MECHANO-ACTIVATED ELECTRONIC AND MOLECULAR STRUCTURES

A Dissertation

by

KE WANG

Submitted to the Office of Graduate Studies of
Texas A&M University
in partial fulfillment of the requirements for the degree of

DOCTOR OF PHILOSOPHY

December 2009

Major Subject: Materials Science and Engineering

MECHANO-ACTIVATED ELECTRONIC AND MOLECULAR STRUCTURES

A Dissertation

by

KE WANG

Submitted to the Office of Graduate Studies of
Texas A&M University
in partial fulfillment of the requirements for the degree of

DOCTOR OF PHILOSOPHY

Approved by:

Co-Chairs of Committee,	Hong Liang
	Winfried Teizer
Committee Members,	Jorge Seminario
	Philip Hemmer
Chair of Intercollegiate Faculty,	Tahir Cagin

December 2009

Major Subject: Materials Science and Engineering

ABSTRACT

Mechano-activated Electronic and Molecular Structures. (December 2009)

Ke Wang, B.S., Lanzhou University;

M.S., Peking University

Co-Chairs of Advisory Committee: Dr. Hong Liang
Dr. Winfried Teizer

For centuries, researchers have been trying to achieve precise control and tailor materials properties. Several approaches, i.e., thermo-activation, electro-activation, and photo-activation, have been widely utilized. As an alternate and fundamentally different approach, mechano-activation is still relatively less-known. In particular, understanding the roles of mechano-activated electronic and molecular structures is yet to be achieved.

This research contributes the fundamental understanding in mechanisms of mechano-activation and its effects on materials properties. Experimental investigation and theoretical analysis were involved in the present research. A methodology was developed to introduce the mechnao-activation and to study its subsequent effects. There are three major areas of investigation involved. First, the means to introduce mechano-activation, such as energetic particle collision or a bending deformation (tensile force); Second, in-situ and ex-situ characterization using AFM, FTIR, UV-Vis, and XPS etc. techniques; Third, theoretical analysis through modified Lennard-Jones potentials in order to explain the behavior of materials under mechano-activation.

In the present research, experiments on a Diamond-Like Carbon (DLC) film, a Polyvinylidene Fluoride (PVDF) film, and the Silver-Crown Ether nanochains (Ag-NCs) were carried out. For DLC, the collision-induced transformation between hybridization states of carbon was confirmed, which also dominated the friction behavior of the film. For PVDF, results show that the applied tensile force induced the transformation of α, β, and γ crystalline phase. In addition, the transformation observed was time and direction dependent. For Ag-NCs, a new approach based on the mechanism of mechano-activation was developed for nanochain structure synthesis. Molecular dynamics simulation and experimental results revealed that the formation of Ag-NCs is a synergetic physical-chemical procedure. Experimental results from DLC and PVDF were further used to validate the proposed potential, which brought new insight into the activation process. The current research achieves a precise control on engineering materials properties. The force-activated materials have wide applications in many areas, such as functional coating, sensing, and catalysis.

In this study selected experiments have demonstrated the effects of mechano-activation in different material systems (ceramic, polymer, metallic nano structure) and at different length scales. For the first time, a modified potential was proposed to explain the observed mechano-activation phenomena from the energy point of view. It was validated by experimental results of DLC and PVDF. The current research brings new understanding in mechano-activation and opens potential for its applications in tailoring materials properties.

DEDICATION

To my family for their unconditional love and support

ACKNOWLEDGEMENTS

Station (TEES), the Department of Mechanical Engineering, and the Materials Science and Engineering Interdisciplinary Program.

Finally, I would like to thank my friends and family, especially my wife, Xun, and my parents for their support and encouragement. They have always been supportive during years of my study. Their unconditional love provides me the strength to go through any difficulties.

NOMENCLATURE

AFM   Atomic Force Microscopy

FTIR   Fourier Transform Infrared Spectroscopy

UV-Vis   Ultraviolet Visible Spectroscopy

XPS   X-ray Photoelectron Spectroscopy

DLC   Diamond-like Carbon

PVDF   Polyvinylidene Fluoride

Ag-NCs   Ag Nanochains

EDS   Energy Dispersive X-ray Spectroscopy

TEM   Transmission Electron Microscopy

XRD   X-ray Diffraction

a-C:H   Hydrogenated Amorphous Carbon

ta-C   Tetrahedral Amphorous Carbon

SEM   Scanning Electron Microscopy

AES   Auger Electron Spectroscopy

LVDT   Linear Variable Differential Transformer

FWHM   Full Width at Half Maximum

UHV   Ultrahigh Vacuum

SPR   Surface Plasmon Resonance

BE   Binding Energy

L-J   Lennard-Jones

TABLE OF CONTENTS

LIST OF FIGURES

LIST OF TABLES

CHAPTER I

INTRODUCTION

In the current research, a systematic study on the effects of mechano-activated electronic and molecular structures on material properties at different length scales was presented. This chapter introduces the necessary background for the area of electrons and electronic structures, mechanochemistry, and mechano-activation.

1.1. Roles of Electrons and Electronic Structures

During the activation processes, the excited electrons play important roles in guiding the reaction path, reaction rate, or the final products. In order to elucidate the roles of activated electrons under mechano-activation, it is necessary to have a thorough understanding on electrons and the roles of electronic structures.

1.1.1. History in the Study of Electrons

The interaction between materials is primarily through the bonds between valence electrons which hold atoms together to form solid, liquid, and molecular states. Most material properties, such as electrical, optical, magnetic, and mechanical, depend on the electrons. The better we understand them, e.g., position and energy, the better we can design and utilize materials.

The word "electron" origins from Greek *"ēlectron"* that means amber.[1] It is a yellow fossilized resin of evergreen trees and was known as a natural plastic material to

_____

This dissertation follows the style of *Journal of Physical Chemistry C*.

ancient Greeks. They found that when amber was rubbed by a dry cloth, it produced attraction that is now called static electricity. In 1600s, William Gilbert invented the word "electric" from studying the same attraction phenomenon. Since then, the words "electricity" and "electron" have been wildly used.[2,3] The milestones in the history of electron-related study are shown in the Figure 1.1.

Although electric phenomena have been known for centuries, the study on electronic structure began in the 1890s with the discovery of an electron as a particle. In 1896, Hendrik A. Lorentz first used the electron theory to interpret the splitting of spectral lines by a magnetic field[4], which was discovered by his student, Pieter Zeeman. They concluded that radiation from atoms was due to negatively charged particles with a very small mass. One year later, J. J. Thomson[5] discovered the electron in an experiment on ionized gases at the Cavendish Laboratory in Cambridge. Thomson's results also confirmed that the electron is negatively charged, with a charge to mass ratio similar to that found by Lorentz and Zeeman. For their contribution, the Nobel Prize was awarded to Lorentz and Zeeman in 1902 and to Thomson in 1906.

The continuous study on electrons brought fundamental improvement on the understanding of material and a series of Nobel Prizes. In 1923, Millikan[6] won the Nobel Prize for his work on the elementary charge of electricity and the photoelectric effect. In 1925, Frank and Hertz won the Nobel Prize for their discovery of the laws governing the impact of an electron upon an atom. Four years later, de Broglie won the Nobel Prize for his genius thought on the wave nature of electrons.
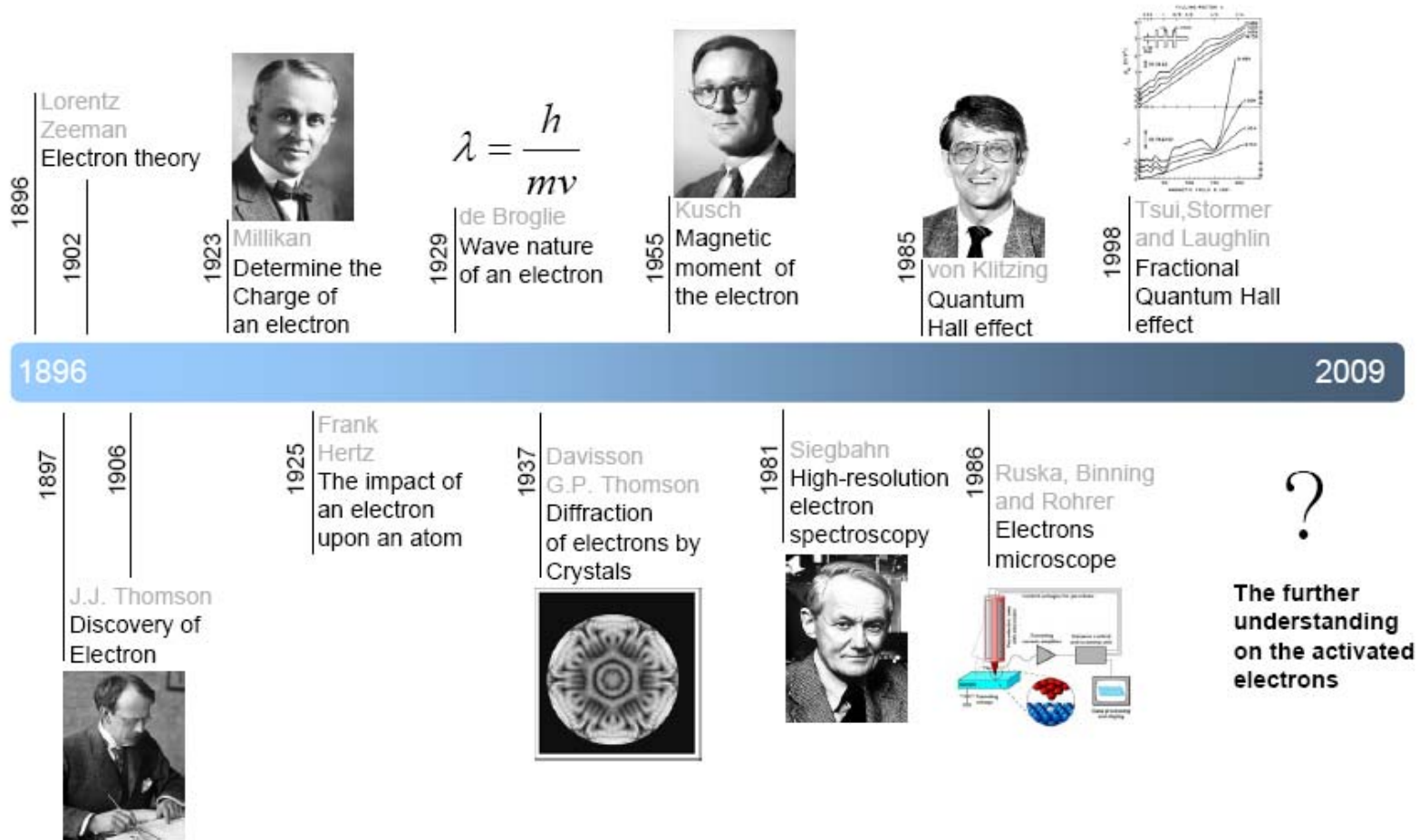
Figure 1.1. Milestones in the history of electron related study

Davisson and G.P. Thomson[7] won the Nobel Prize for their experimental discovery of the diffraction of electrons by crystals in 1937. In 1955, Kusch's work on precise determination of the magnetic moment of the electron won himself the Nobel Prize[8]. In 1981, Siegbahn[9] received half of the Nobel Prize for his contribution to the development of high-resolution electron spectroscopy. Four years later, von Klitzing[10] won the Nobel Prize for the discovering of the Quantum Hall effect. Just after one year, in 1986 Ruska, Binning and Rohrer[11] shared the Nobel Prize for their fundamental work in electron optics and for the design of the first electron microscope. In 1998, Laughlin, Stormer and Tsui[12] shared the Nobel Prize for discovering the fractional Quantum Hall effect. Researchers believed that the further understanding on the activated electronic structures would open new avenue to control material properties.

1.1.2. Roles of Electronic Structures

Since the discovery of electrons in 1896, the theory of electrons and electronic structures has attracted great attention in materials related research. Researchers believe that understanding of materials and phenomena depends on our knowledge in electronic structure. Because electrons and nuclei are the fundamental building blocks that determine the nature of materials: atoms, molecules, bulk matter, and artificial structures. Electrons not only form the "quantum glue" that maintain materials in their respective states, but also electronic structures determine the various properties of material, such as electrical, optical, and magnetic properties.

Here the electronic structure does not limit to the arrangement of electrons in the shells of an atom. It includes the orbital or bond formed through the interactions between the electrons in the valence shell of atoms, such as σ bond and π bond.

Carbon is a good example to elucidate the roles of electronic structures. As one of the most versatile elements in the periodic table, carbon virtually can form an infinite number of compounds. This is due to the various types of bonds or hybridization states it can form with other elements.

For electron hybridization, sp^2 and sp^3 are two common types. For sp^3 hybridization, each of the carbon's four valence electrons is assigned to a tetrahedrally structured hybrid orbital. It forms a strong σ bond with an adjacent atom and results in tetrahedral bonding arrangement, as the basic building block of diamond shown in the Figure 1.2. For sp^2 hybridization, three of four electrons are assigned to the equal lateral triangle hybrid orbital, which forms intra-layer σ bonds. The fourth electron has a p orbital that is normal to the σ bonding plane. The p orbital between adjacent planes can form weak π bond, such as the van der Waals bonding between layers of graphite.
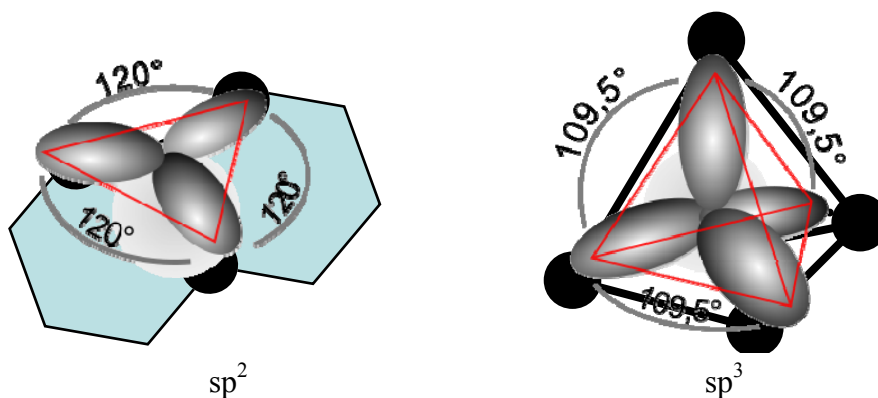
Figure 1.2. sp^2 and sp^3 hybridization of carbon

In fact, graphite and diamond are two extreme examples of carbon. Graphite only contains sp^2 hybridization and weak van der Waals bonding between its layers. It is soft and conductive. In the bulk, graphite is an anisotropic metal. For a single graphite plane (graphene), it is a zero band gap semiconductor. Diamond contains only sp^3 hybridization which results in the strong, directional σ bond. It has a hardness of 100 GPa and is an insulator with wide band gap of 5.5 eV. Using carbon as an example, the roles of electronic structures in determining materials properties are apparent.

1.2. Roles of Electrons and Electronic Structures

1.2.1. Activation Methods

There are four alternate ways to activate the energy states of electrons and molecules at surfaces and interfaces: thermo-activation, electro-activation, photo-activation, and mechano-activation.[13-17] As listed in Table 1.1., the first three are chemical activation methods that have been well studied and accepted. The fourth way is a physical activation method, mechano-activation, which is less known.

Table 1.1. Activation methods

Activation Methods		
Chemical Methods	Thermo-Activation	Electro-Activation	Photo-Activation
Physical Methods	Mechano-Activation		

1.2.1.1. Thermo-activation

Thermo activation origins from the study of thermochemistry, which is generally concerned with energy exchanging in the form of heat. Thermo-activation initiates the interactions between atoms and molecules via heat.

A study on tailoring the electronic structure of a bilayer graphene via potassium doping was reported by T. Ohta et al. [13] In the study, they synthesized the bilayer graphene thin film on insulating carbide and used the angle-resolved photoemission to characterize the electronic band structure. By carefully increasing the carrier concentration in each layer, changes in the Coulomb potential led to the modification of the band gap between valence and conduction bands. The gap was first open at the doping concentration of 0.005 e, then closed at the concentration of 0.0125 e, and finally opened again at the concentration of 0.035 e. The authors demonstrated that the occupation of electronic states near E_F and the magnitude of the gap between the valence and conduction bands could be manipulated by controlling potassium doping.

1.2.1.2. Electro-activation

Electro-activation origins in electrochemistry that generally involves energy exchange with the transfer of electrons. Electro-activation initiated the interactions via means of transferring electrons between atoms or molecules under the application of an external voltage or through the release of chemical energy.

An example on switchable, palindromically constituted bistable [3] rotaxane was given. It was designed and synthesized to mimic the function of a muscle. The columbic

repulsion between specific functional groups were initiated or reduced via electro-chemical oxidation or reduction.

Y. Liu et al. [14] designed and synthesized bistable [3] rotaxanes which has a pair of mechanically mobile rings encircling a single dumbbell. There were two energy favored positions for the two cyclobis(paraquat-p-phenylene) (CBPQT^{4+}) rings. One was at tetrathiafulvalene (TTF) station, the other was at naphthalene (NP) station. By applying an electrical potential, the rings could move from TTF to NP station with an inter-ring distance change from 4.2 to 1.4 nm. Their work opened an avenue to control the nano scale mechanical movement of microbeams via electrochemical activation.

1.2.1.3. Photo-activation

Photo-activation origins in the study of photochemistry that generally involves the energy exchanging through light absorption. Photo-activation initiates the interaction between atoms or molecules via means of photon irradiation and absorption. An example on the photo-induced formation of electrically conductive thin palladium nanowires on DNA scaffolds was given.

In the experiment, a photochemical method had been exploited for a fast synthesis of electrically conductive Pd nanowires.[15] We found that the Pd nanowires growed as the UV irradiation time increases; without irradiation, no formation was detected. The EDS, TEM, and XRD results are given in the Figure 1.3. As shown in the Figure 1.2a and b, the average diameters of the Pd nanowires were 55-75 nm, and the average lengths were ~3-5 µm. The EDS analysis was used to determine the chemical composition of synthesized. The EDS spectrum consisted mainly of Pd, C, Cu, N, and P peaks.
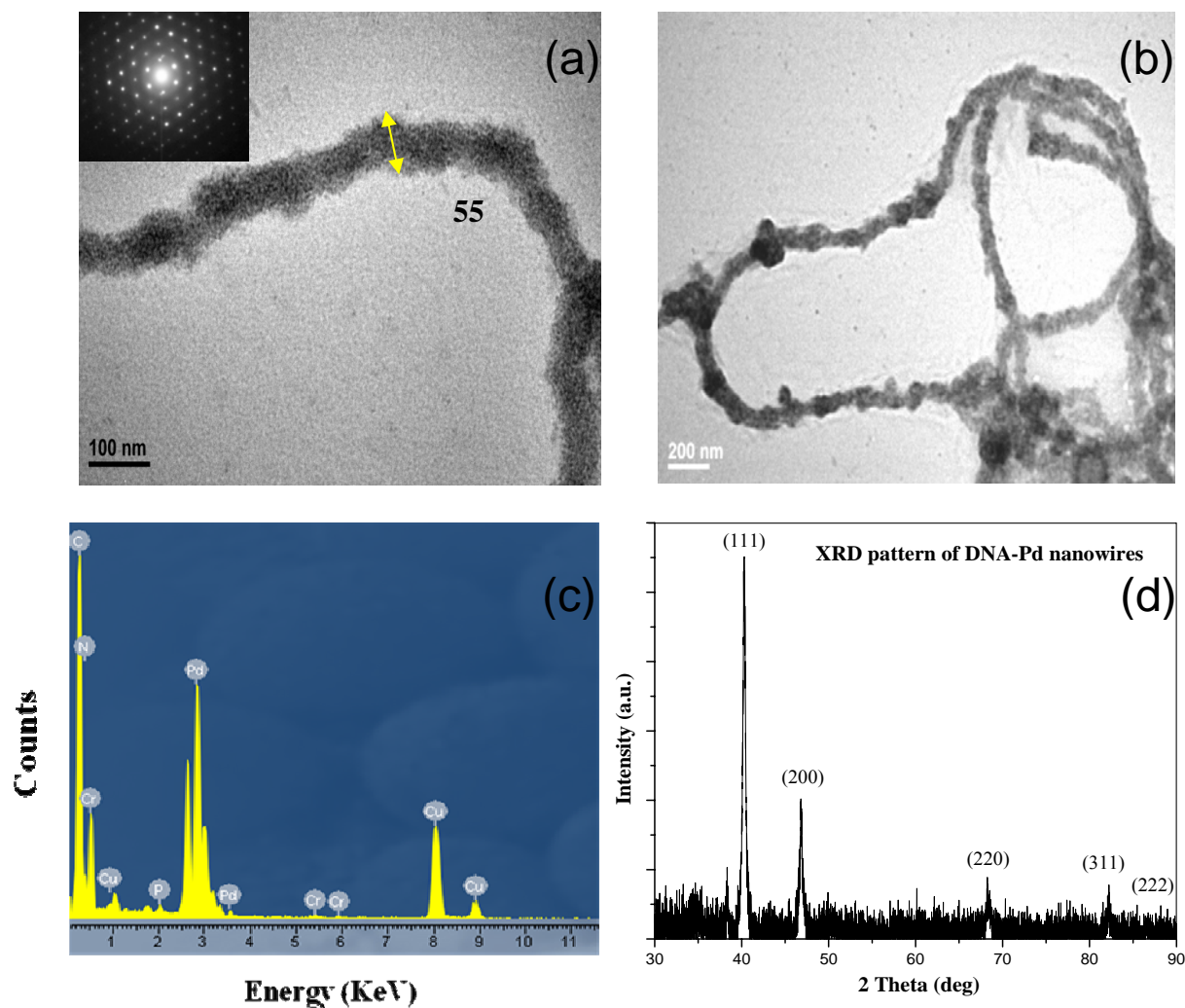
Figure 1.3. (a) and (b) TEM images of Pd nanowires after UV photo-irradiation. (a) A bent single chain DNA-Pd nanowire, inset shows the selected area electron diffraction pattern indicated crystalline nature of the nanowire. (b) Pd nanowires synthesized with S value of 3. (c) Energy dispersive X-ray spectrum (EDS) of the DNA-Pd nanowires. (d) Powder X-ray diffraction pattern of the DNA-Pd nanowire[15]

The C and Cu peaks came from the carbon-coated Cu TEM grid used for the analysis. The Pd peak came from the reduced Pd nanowire and the small P and N peaks came from the DNA. From the XRD result, the diffraction peaks originated from the {111}, {200}, {220}, {311}, and {222} planes were identified. The ratio of the

intensities of {200} and {111} diffraction peaks is higher than the conventional value, indicating that the nanowires were abundant in {110} planes and oriented parallel to the surface of the substrate.

Based on the experimental results, we proposed that the mechanism of photo-induced synthesis of Pd nanowires on DNA proceeds in three steps, as shown in the Figure 1.4. Initially, positively charged Pd (Ⅱ) ions formed a complex with DNA. Then Pd (Ⅱ) ions were reduced to Pd (0) and formed seeds on DNA scaffold under UV photo irradiation (260nm). The hydroxyl group of DNA in the deoxyribose sugar part might initiate the reduction of Pd (Ⅱ) to Pd (0) in the presence of UV photo irradiation. With time, the Pd seeds growed to form bigger Pd nanoparticles, then crosslinked to form Pd nanowires on the DNA template.
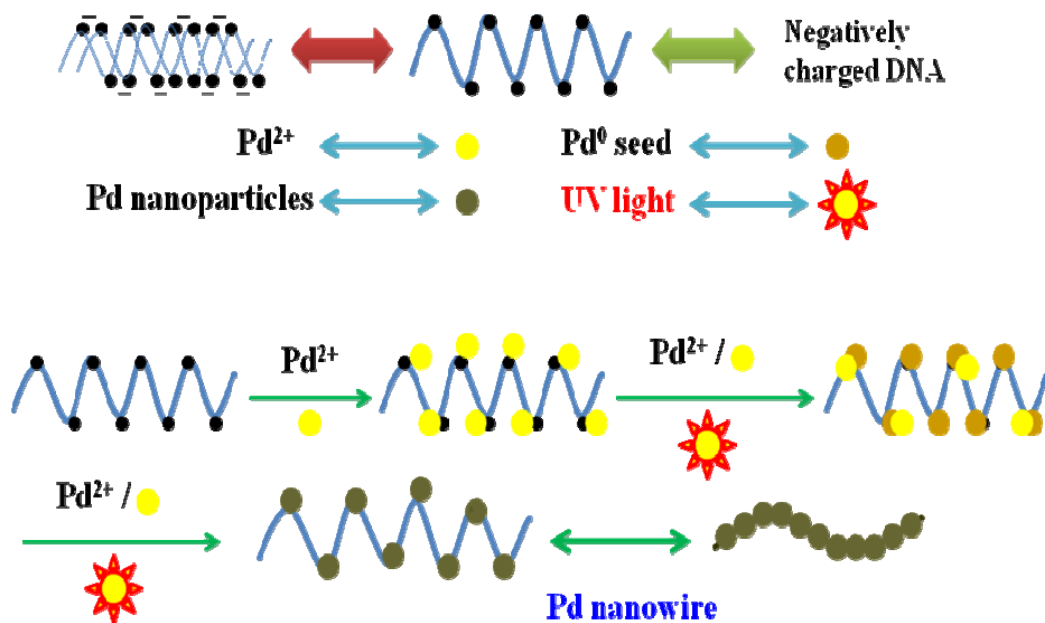
Figure 1.4. Proposed mechanism for the photo-induced formation of electrically conductive thin palladium nanowires on DNA scaffolds[15]

1.2.2. Mechano-activation

Besides thermo-activation, electro-activation, and photo-activation, mechano-activation is a fundamentally different way to excite the electronic or molecular structures. In most cases, a mechanical force will be involved in the excitation process, no matter it is via collision or bending deformation, or compression. It has been reported that a mechanical force can activate covalent bonds in polymers and result in chain scission[18-21], guide reaction pathway,[22] or facilitate the nanostructure fabrication[16].

The term "Mechanical Activation" was firstly introduced by Smékal in 1942.[23] It was assigned to a method for increasing the reaction activity of solids and, consequently, to accelerate solid phase reactions and to reduce the temperature of the subsequent thermal decomposition. "Mechano-Activation" was used later to compare with other activation methods. It has been confirmed that the mechano-activation is usually accompanied with changes in composition or micro structure.

A prudential definition was made by Butyagin[24] in 1984, where the mechano-activation was defined as an increase of reaction ability due to the stable change in solid structure. He explained the effects of mechanical energy on solids from three aspects: structural disordering, structure relaxation and structure mobility.

Juhász categorized the influence of mechano-activation from a different point of view, i.e., the primary and secondary processes.[25,26] The primary process would increase the reactivity of the substance, such as the increase of internal or surface energy. The extra energy introduced via mechano-activation could excite the atoms and molecules to a higher energy state, helped the system go over the energy barrier to initiate a reaction, and then consequently enhanced the reactivity. The secondary process took place

spontaneously with the mechano-activation. It usually accompanied with structure rearrangements, which needed less energy than the primary one to initiate the process.

1.3. Electron and Roles of Electronic Structure

Besides thermochemistry, electrochemistry, and photochemistry, mechanochemistry is an alternative branch of chemistry. It deals with the chemical and physico-chemical changes of substances in all states of aggregation.

The term "Mechanochemistry" was first introduced by Nobel Laureate Fridrich Wilhelm Ostwald (Nobel Prize in Chemistry 1909) in his book "Lehrbuch der Allgemeinen Chemie" (Textbook of General Chemistry). In which, he defined the mechanochemistry along with thermochemistry, electrochemistry, and photochemistry from the energy point of view as part of his effort to systemize chemical disciplines.

From the first attempt by primitive to make fire using friction to the ignition of solid explosives via shock, the effects of mechanical force on the route of chemical reaction are part of the early experience of human being. People have realized that mechano-activation itself can lead to chemical consequences as thermo-activation, electro-activation, and photo-activation do. The milestones in the history of mechanochemistry are summarized in Table 1.2.

Table 1.2. History of mechanochemistry

Time	Events
371-286 B.C.	The first written document on the mechanochemical preparation of mercury by Theophrastus of Eresus in his book "De Lapidibus".
16th century	Several examples of mechanochemistry were observed by Agricola during milling and metallurgical operations.
19th century	A mechanochemical process on the decomposition of silver chloride was reported by Faraday.
Late 19th century	Detailed studies on the decomposition of Ag, Hg, Pt, and Au halides during attrition in a mortar were documented by Carey Lea
Early 20th century	The term "Mechanochemistry" was first introduced by Ostwald.
1920s	Early mechanochemical study of organic macromolecules was carried out by Wanetig, Staudinger, Kauzmann, and Eyring.
1941	Transformation between two dimorph of PbO under hydrostatic pressure was observed by Clark and Rowan.
Since 1970s	Single molecule or single bond studies

The first mechanochemical reaction was reported by Theophrastus of Eresus (371-286 B.C.), a student of Aristotle, in his book "De Lapidibus" or "On Stones". In this book, the following sentence was mentioned "Native cinnabar was rubbed with vinegar in a copper mortar using a copper pestle, then yielded a liquid metal of mercury." It was the first written document of a mechanochemcial reaction. The mechanochemically induced reduction of mercury may follow the reaction:[27-29]

$$HgS + Cu \rightarrow Hg + CuS \tag{1.1}$$

When the native cinnabar is rubbed in a brass mortar with a brass pestle in the presence of vinegar, metallic mercury is obtained.

In the medieval literature, only a few documents were found on the topic of mechanochemistry. Several examples of the mechanical action initiated chemical reactions during the milling and metallurgical operations were reported by Agricola.

As a pioneer in electromagnetic theory and nano-material synthesis, Faraday also made his contribution to mechanochemistry. In 1820 he reported a mechanochemical process on the decomposition of silver chloride, as shown in equation 1.2. Later on, he also found that certain hydrated salts dehydrated spontaneously under mechanical treatments, such as using mortar or comminution.

$$2AgCl + Zn \rightarrow 2Ag + ZnCl_2 \tag{1.2}$$
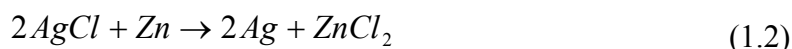
In the discipline of mechanochemistry, researchers usually regard Carey Lea as the first mechanochemist. He carried out detailed study on the decomposition of Ag, Hg, Pt, and Au halides during attrition in a mortar. When heated, he observed that AgCl melted and Hg_2Cl_2 sublimated without decomposition, but under the effect of stress both of them decompose with the formation of elementary metals and chlorine. The reactions probably proceed through the following courses:

$$2AgCl \rightarrow 2Ag + Cl_2 \tag{1.3}$$
$$Hg_2Cl_2 \rightarrow 2Hg + Cl_2 \tag{1.4}$$

For the first time, Lea experimentally proved the parallelism between the thermo-activation, electro-activation, photo-activation, and mechano-activation on the silver halides. Early experimental mechanochemistry was focused on the decomposition of inorganic salts under the influence of mechanical force. Later on, the transformation of solids under mechano-activation attracted more interest. Clark and Rowan[30] found that the transformation between two dimorph of PbO (massicot↔litharge) occurs during

milling, where litharge and masscicot are the natural forms of lead oxide. Litharge has the internal tetragonal crystal structure and massicot has the orthorhombic form. They attributed the applied hydrostatic pressure to the litharge-massicot transformation.

Substantial contribution on the mechano-activation phenomena in organic macromolecules has been made since the 1920s. Inspired by the needs of the paper industry, Wanetig[31] studied the beneficial effect of grinding on cellulose's solubility. He confirmed that the mechanical destruction of the macromolecule and creation of new hydrophilic groups via breaking valence bonds would make the paper pulp more solvable. Later on, Staudinger et al.[19,32] proved that the reduction of the molecular weight of polymers was caused by the mechanically induced disruption of the valence bonds in the carbon chain under mastication. Their explanation was further refined by Kauzmann and Eyring.[18] They suggested that the hemolytic cleavage of the C-C bonds in the backbone under a mechanical force is the real reason for the shortening of polymers.

From the end of 20th century, considerable attentions have been attracted on bimolecular reaction under mechano-activation, mechanochemical synthesis, mechanochemistry in a single molecule or single bond such as mechanical rupture forces of covalent bonds,[33,34] metallic bonds,[35,36] or coordinative bonds.[37,38]

Meanwhile, researchers spent a lot of efforts on developing theories and models to explain the observed results. They are summarized in Table 1.3.

Table 1.3. Theories and models in mechanochemistry

Time	Theory or Model	Authors
1952, 1958	Hot-Spot Theory	Bowden, Tabor, and Yoffe[39-41]
1967	Magma-Plasma Model	Thiessen, Meyer, and Heinicke[42]
1969, 1974	Dislocation and Phonon Theory	Gutman, Bertenev, and Razumovskaya[43,44]
1973	Theory of Short-Live Active Centers	Butyagin[45]
1984, 1986	Impulse Model	Lyachov[46]

The first trial was Hot-Spot Theory developed by Bowden, Tabor, and Yoffe.[39-41] In the experiment, a temperature raise of 1000K in an area of $1\mu m^2$ was found on the surface under a 10^{-4}-10^{-3} s friction process. They attributed this temperature increase as the cause of mechanically initiated reactions.

In 1967, Thiessen et al.[42] proposed the Magma-Plasma Model. In this model, a special plasmatic state formed by the emission of excited fragments of solid sample at the contact spot of collision. The temperature in those regions could reach more than 10000K, which would enhance the local reactivity. But the plasmatic state had very short life time, usually less than 10^{-7} s.

Gutman, Bertenev, and Razumovskaya[43,44] brought up the Dislocation and Phonon Theory. According to this theory, the dislocations caused by the mechano-activation could diffuse to the surface and consequently increase the chemical activities. At the same time, the motion of dislocations and the interaction between them was accompanied by the formation of phonons.

Butyagin[45] used the theory of Short-Live Active Center to explain the rearrangement of chemical bonds under mechanical treatments. New structures at the

surface caused by the mechano-activation were not able to stabilize in the 10^{-9}-10^{-11} s of thermal excitation. For the stabilization and rearrangement of chemical bonds, a longer time of 10^{-4}-10^{-7} s was required. The decay of short-live centers depended on the relaxation processes.

With the developing of mechano-activated synthesis, the Impulse Model was proposed by Lyakhov[46] in order to interpret the kinetics of reactions observed in the ball milling process. The model was based on the time intervals of a stress field formation and its relaxation due to the impulse effect of milling balls on materials.

To date, mechanochemistry has been an established field in material science and solid-state chemistry. But the research on mechano-activation has not been complete yet. As for the mechano-activation of polymers, the emergence and relaxation of stress fields in these systems have not been thoroughly studied. Little is known about the response of different phases in polymer under the influence of a mechanical force. In addition from the application point of view, effects of mechano-activated electrons on material properties at different length scales, e.g., crystal structure, phase transformation, and surface conductivity, have not been systematically discussed. Furthermore, an energy based theory on mechano-activation has not been developed yet.

1.4. Summary

In this chapter, basic understanding in mechanochemistry, mechano-activation, and the roles of electronic structures are introduced. It presents the contributions in experiment and theory that have been made in this area. However, effects of mechano-

activation on material properties have not been carefully studied at different length scales. More importantly, in order to obtain the fundamental understanding on the roles of mechano-activated electronic or molecular structures in determining material properties, an explanation from the energy point of view is yet to be developed.

In this study, we focused on the excitation of electronic or molecular structures under mechano-activation and the consequent effects on material properties. Both primary and secondary processes were carefully studied. For the primary process, the studies are focused on the collision-induced hybridization states transformation of carbon atoms in DLC. For the secondary process, the research is concentrated on the time-dependent and anisotropic phase transformation induced by tensile force in PVDF. Detailed discussion will be provided in Chapter Ⅳ and Ⅴ.

Following the introduction, the second chapter delivers the motivations and objectives of the present research as well as the methodology developed to achieve these objectives. The detailed study on the selected material systems is covered in chapters Ⅳ, Ⅴ, and Ⅵ. Theoretical analysis based on an energy diagram is provided in chapter Ⅶ. Finally, conclusions and recommendations for future works are given in chapter Ⅷ.

CHAPTER II

MOTIVATION AND OBJECTIVES

In Chapter I, we discussed the state-of-the-art of the mechano-activation and the basics of electronic structures. It is clear that there are needs to understand the mechanisms of mechano-activation process and its effects. In the present research, we propose to investigate the relationships between mechano-activated electronic/molecular structures and materials properties. Specifically, we will study the mechano-activation phenomena in the selected material systems. We propose a combined experimental and theoretical approach that is based on the energy diagram.

There are two major objectives in this research. The first objective is to study the behavior of mechano-activated surface electrons through experimental examination. The second objective is to obtain fundamental understanding in the relationships between those activated electrons and materials properties. We will focus on the phase transformation at the atomic and molecular scales of thin films that are under mechano-activation. The outcome of the research is expected to lead to discover new behaviors or phenomena and to open perhaps new areas of materials science. Below are details addressing each of the objective:

1)   Experimental examination of mechno-activated electroninc and molecular structures

Apart from thermo-activation, electro-activation, and photo-activation, mechano-activation is a fundamentally different way to alter electronic and molecular structures,

trigger chemical reactions, and consequently modify materials properties. In this study, experiments will be conducted on three selected materials systems. These results will further our understanding in roles of mechano-activation in modifying materials properties.

In order to achieve this objective, the materials will be carefully selected. The chosen materials are from different categories: Diamond-like Carbon (DLC), a ceramic; Polyvinylidene Fluoride (PVDF), a polymer; and Silver-Crown Ether nanochains (Ag-NCs), metallic nanomaterial. The phenomena are at different length scales: the friction behavior of DLC at macro scale; transformation between phases of PVDF at micro scale; and the formation of Ag-NCs at nano scale.

A methodology will be developed to induce mechano-activation and to study their effects. The approach includes three critical parts. First, the means to introduce mechano activation, such as ion collision or bending deformation introduced by special sample stand; Second, in situ and ex situ characterization, such as using AFM, FTIR, UV-Vis, XPS etc. An in situ characterization method for one sample could be an ex situ method for another sample. Third, theoretical analysis, such as spectrum deconvolution or multi-body Lennard-Jones Potential calculation. The developed methodology has the adaptability to different material system and can serve as guidance for future study.

2)   Theoretical analysis of mechano-activation

As discussed in Chapter Ⅰ, section 1.3, from the early Hot-Spot Theory to the Impulse Model, researchers have paid tremendous efforts in understanding mechano-

activation. The theories on activated electronic and molecular structures have been hardly reported.

In this research, a modified interatomic/ intermolecular potential that includes the contribution of mechano-activation will be proposed. Using this modified potential, we will be able to describe the energy states under the influence of a mechanical force and examine the experimental results.

More importantly, the validated potential would not only be able to explain the observed phenomena, but also bring new understanding in mechano-activation and opens potential for its applications in tailoring materials properties.

For the first time, we investigate the effects of mechno-activation on electronic and molecular structures. The research will bring insight from the fundamentals in relations of electronic structure and materials properties. The findings will broaden the scopes for future research as well as provide the guidelines for selection and design of materials for a broad spectrum of engineering applications.

The next six chapters are organized in the following way: after a detailed description of experimental approaches, results are introduced. Discussions are divided into two major areas, DLC and PVDF, followed by a detailed theoretical analysis. The main dissertation ends with the summary and future recommendations.

CHAPTER III

MATERIALS AND METHODS

In this chapter, materials, characterization and analysis methods used in the dissertation research are discussed. Materials from different categories are chosen to study the mechano-activation process and its effects. Selected characterization and data analysis methods are presented.

3.1. Materials

3.1.1. Diamond-like Carbon

Diamond-like carbon (DLC) is a metastable form of amorphous carbon which has similar properties like natural diamond, such as high mechanical hardness, wear resistant and chemical inertness. [47,48,49,50] These unique properties origin from a significant amount of sp^3 hybridization of carbon contained in DLC.

After hydrogen, helium, and oxygen, carbon is the fourth most abundant chemical element in the universe by mass. Its atomic number is 6 and has 4 valence electrons (2s, 1p,1p, 1p). Carbon is able to exist in three hybridization states, sp^3 (like carbon in C_2H_6), sp^2 (like carbon in C_2H_4), and sp^1 (like carbon in C_2H_2). Configurations of each hybridization states are shown in Figure 3.1. For sp^3 hybridization, each of the carbon's four valence electrons is assigned to a tetrahedrally structured hybrid orbital, which forms a strong σ bond with an adjacent atom and results in tetrahedral bonding arrangement.

For sp^2 hybridization, three of four electrons are assigned to the equal lateral triangle hybrid orbital, which forms intra-layer σ bonds. The fourth electron has a p orbital that is normal to the σ bonding plane. The p orbital between adjacent planes can form weak π bond, such as the van der Waals bonding between layers of graphene. For sp^1 hybridization, two of four electrons form hybrid orbital along ± x-axis, and the other two electrons enter the formation of π bonds in y and z directions.[51] The physical properties of carbon hybridization states are given in the Table 3.1.[52]

Table 3.1. Carbon-carbon hybridization states and bond lengths

Bond	Hybrid Type	Energy of Bond (kJ/mole)	Bond Length (nm)
C-C	sp^3	370	0.154
C=C	sp^2	680	0.13
C≡C	sp^1	890	0.12

sp^3 sp^2 sp^1
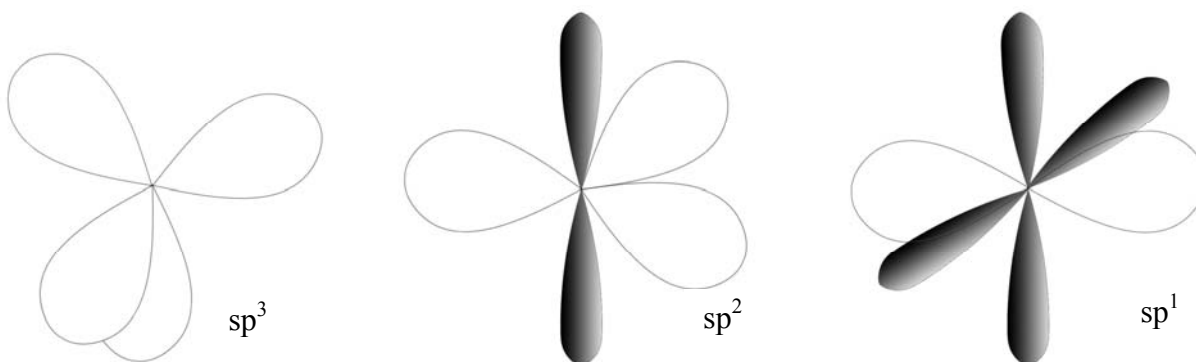
Figure 3.1. Carbon-carbon hybridization states and bond

DLC is a metastable form of amorphous carbon containing both sp^3 and sp^2 hybridization. The sp^3 bonding of DLC contributes to some extreme properties similar to natural diamond, such as the hardness, elastic modulus and chemical inertness. [53-56]

The first fabrication of DLC thin film was reported in early 70s by Asienberg and Chaot using ion beam deposition. There are two types of DLC films being reported, hydrogenated amorphous carbon (a-C:H)[56] and tetrahedral amphorous carbon (ta-C) [57]. The major properties of amorphous carbon and other reference materials are given in Table 3.2.[58-61]

Table 3.2. Comparison of major properties of amorphous carbons with natural diamond and graphite

	sp3 (%)	sp2 (%)	H (%)	Density (g/cm^3)	Hardness (GPa)
Diamond[58]	100	0	0	3.515	100
Graphite[59]	0	100	0	2.267	
ta-C[60]	80-88	12-20	0	3.1	80
a-C:H[61]	40	60	30-40	1.6-2.2	10-20

Due to its unique properties, DLC has been wildly used as protective coatings, as for drills, bits, magnetic storage disk[62-64], and biocompatible coatings on parts such as replacement hip and knee joints, heart valves, and stents. [65-67]

In our experiment, a tetrahedral amorphous (ta-C) DLC film was deposited on 52100 bearing steel disks using a PVD method. The coating had a surface roughness of about 30 nm in root mean square and contained less than 0.5 %at of hydrogen.

3.1.2. Polyvinylidene Fluoride (PVDF)

Due to its unique piezo-, pyro-, and ferroelectric properties, polyvinylidene fluoride (PVDF) has been insensitively studied for its physical properties and applications.[68-70]

As a member of thermoplastic fluoropolymer family, PVDF is a semicrystalline polymer that contains the mer unit of $C_2H_2F_2$. It has the molecular weight about 10^5, which contains 2000 repeat units and has an extended length of 50 μm. The physical properties of PVDF and other piezoelectric polymers and ceramics are given in Table 3.3.[71-72]

As a semi crystalline polymer, PVDF has five crystallographic forms, α, β, γ, δ and ε. The crystalline structures of α, β, γ, and δ, when projected onto a plane normal to the molecular axis, are shown in Figure 3.2. In all of them, the chains are packed in the unit cell in such a way that the dipoles associated with individual molecules are parallel one to the other, leading to the non-zero dipole moment of the crystal.

Table 3.3. Physical properties of PVDF and other piezoelectric materials

	Structure	Density (g/cm^3)	Piezoelectric Coefficient, d (pC/N)	Pyroelectric Coefficient, p (µC/K m^2)	Max Use Temp (°c)
PVDF[71]		1.78	d_{31}=20-30	30-40	80
PTrFE[71]		1.90	d_{31}=15-30	30-40	90-100
LZT[72]		7.5	d_{31}=100-300	50-300	
Quartz[72]		2.7	d_{11}=2		

PTrFE: Poly Vinylidene Fluoride-trifluoroethylene and Tetrafluoroethylene Copolymers
LZT: Lead Zirconate Titanate

(a) β-phase (orthorhombic)   (b) α-phase (orthorhombic)

(c) δ-phase (orthorhombic)   (d) γ-phase (monoclinic)

⬤ : Fluorine   ⚬ : Carbon
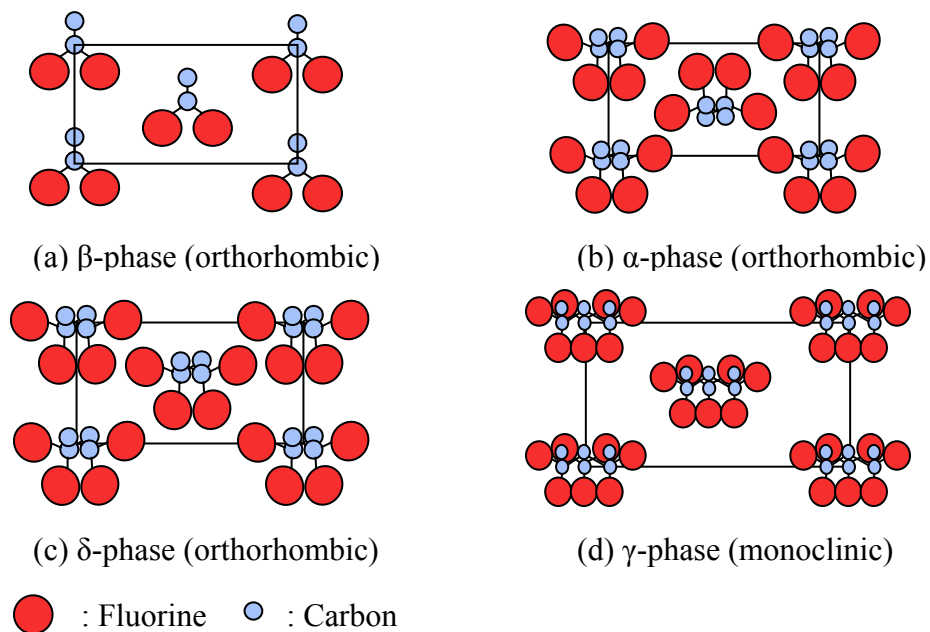
Figure 3.2. Crystal structures of (a) β, (b) α, (c) δ, and (d) γ phases of PVDF

In β phase, all chains are oriented parallel to the y-axis of the unit cell with the dipoles pointing in the same directions, resulting in a noncentrosymmetric crystal. The net dipole moment along y-axis is 2.1 D.

The arrangement of the molecules in α phase is such a way that it results in a centrosymmetric unit cell, which is antipolar. The molecular dipoles are antiparallel and there is no net dipole. δ phase has the similar crystal structure as α phase, except that the center chain has the same orientation as the others. The unit cell is noncentrosymetric and it has net dipole moment of 1.3 D.

For γ phase, the molecular chains are packed in parallel in the noncentrosymetric unit cell. Such an arrangement results in a net dipole moment that is smaller than β and δ phases.

The transformation between polar and non-polar phases can be obtained under different experimental conditions such as applying tensile stress (α phase → β phase),[73,74] poling under external electric fields (α phase → β and δ phase),[75-77] or annealing at high temperatures (α phase → γ and ε phase).[78,79] Recently, we reported the time-resolved and anisotropic transformation between crystalline and amorphous phases in PVDF under the applied tensile force.[80]

It has been accepted that the electromechanical properties of PVDF, such as ferroelectricity, piezoelectricity, and pyroelectricity are originated from the alignment of the polarization domain. However, the fundamental understanding on the stress-induced phase transformation in micro-, nano-, and molecular length scale has yet to be achieved. An in situ characterization and analysis of small scale phase transformation is necessary

to identify the role of mechanical force and help to understand origin of the piezoproperties.

Taking advantage of its electromechanical properties, light weight and the flexibility, PVDF has been used in various applications such as impact sensor, pressure switch, and medical probe.[72] As a critical part in keyboard, a 16 μm thin metalized polar PVDF film is able to sustain 15 million pushes without failure.[81]

PVDF films (Measurement Specialties, USA) were used for this research. They were casted from solution to the thickness of 9 μm and 52 μm. During electrical poling, uni-axial stretching was applied at temperatures right below the melting point. This process disentangles chain packing of the molecules along the tensile direction.

In order to apply a controlled force while doing the AFM and FTIR analysis, special sample stands were designed resembling a half-cylinder. The stand for the AFM has a radius of 6 mm and width of 6 mm. Another stand for the FTIR has a radius of 15 mm and width of 15 mm, at the top a hole with diameter of 5 mm was purposely made to let the infrared light pass through. PVDF samples of 6 mm × 10 mm and 30 mm × 20 mm were assembled on to the round surface of the stands and placed under AFM and FTIR for characterization, respectively. Both samples were carefully mounted onto the stands to avoid extra tensile force, the ends of samples were fixed by using adhesive. Bending deformation was induced in longitudinal and transversal directions with respect to the initial chain orientation (stretching direction), as shown in Figure 3.3a and b. Under longitudinal deformation, the bending direction is along the original chain orientation. Under transversal deformation, the bending direction is perpendicular to the original chain orientation.
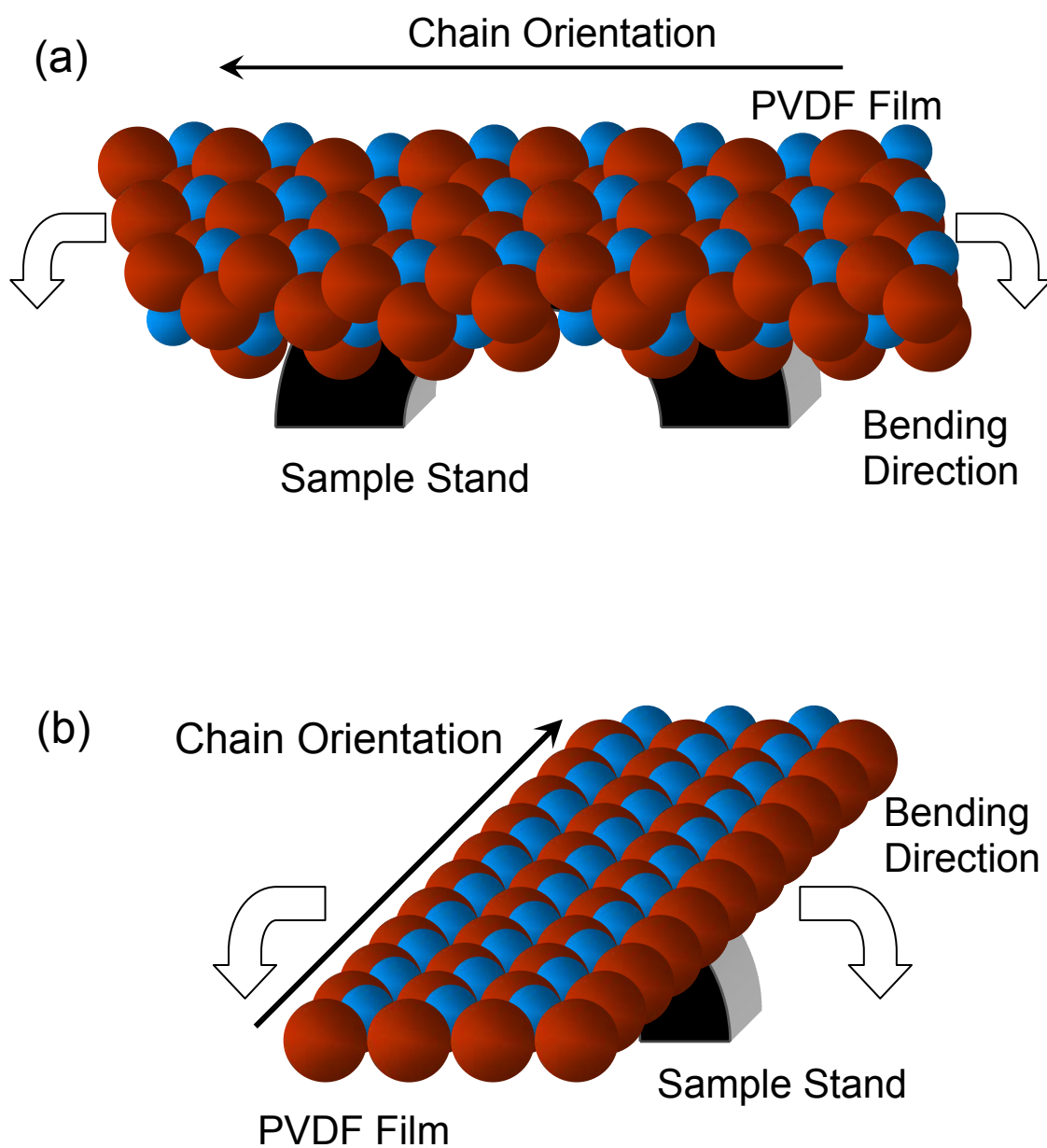
Figure 3.3. Bending deformation introduced on PVDF film (a) longitudinal direction, (b) transversal direction

3.1.3. 18-Crown Ether-6

"Crown Ethers" is the common name for a group of macrocyclic polyethers that consist of a ring containing several ether groups. Crown Ethers have 9 to 60 atoms including 3-20 oxygen atoms in the ring.[82,83] The oxygen atoms are separated from each other by two carbon atoms. The repeating unit of Crown Ether is usually CH_2CH_2O. A schematic drawing of 18-Crown Ether-6 is given in Figure 3.4, where "18" stands for the total atoms in the ring and "6" represents the number of oxygen atoms in the ring. The physical properties of 18-Crown Ether-6 are listed in Table 3.4.
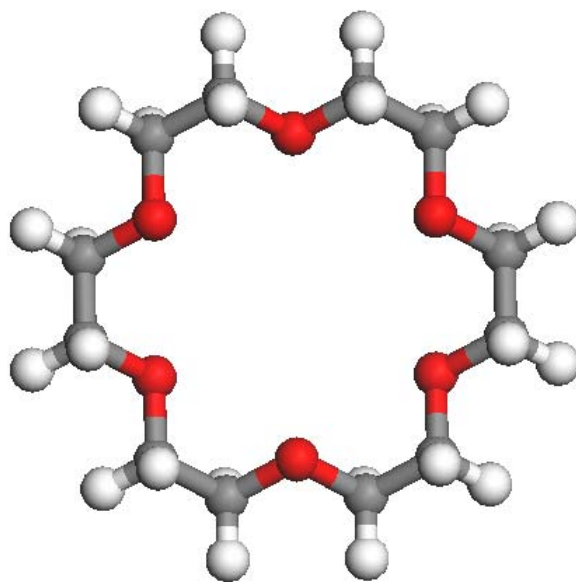
Figure 3.4. 18-Crown Ether-6 (red: oxygen; white: hydrogen; gray: carbon)

Table 3.4. Physical properties of 18-Crown Ether-6

	Molecular Formula	Molar Mass (g/mol)	Density (g/cm^3)	Melting Point (°c)
18-Crown Ether-6	$C_{12}H_{24}O_6$	264.32	1.237	39-40

One of the remarkable properties of Crown Ethers is their ability to capture alkali, alkaline-earth and transition-metal cations on the basis of metal ion size. It was first discovered by Pedersen.[82] He published the paper "Cyclic Polyethers and Their Complexes with Metal Salts" on the Journal of the American Chemical Society in 1967, which later on won him the Nobel Prize in chemistry in 1987. In the paper, he presented 33 cyclic polyethers and proved that many of them have the unusual property to form relatively stable complexes with metal ions. The selectivity of Crown Ethers as complexing agents results from the definite size of the Crown Ether ring, which only accepts cations of comparable ionic radii. Table 3.5. provides the information about the ring size of several Crown Ethers and the ionic radii of complexable cations.[84,85] 18-Crown Ether-6 has an estimated cavity diameter of 2.6-3.2 Å and is most suitable for complexing with K^+, NH_4^+, and Rb^+ (ionic diameters 2.66, 2.86, and 2.94Å, respectively).

Table 3.5. Crown Ether ring size and complexable cation size

Crown Ethers and Their Ring Size		Complexable Cations and Their Size			
	Diameter (Å)		Diameter (Å)		Diameter (Å)
14-Crown-4	1.2-1.5	Li	1.36	Ag	2.52
15-Crown-5	1.7-2.2	Na	1.94	Cs	3.34
18-Crown-6	2.6-3.2	K	2.66	NH_4^+	2.86
21-Crown-7	3.4-4.3	Rb	2.94	Ca	1.98

It has been wildly accepted that the size match selectivity of Crown Ether is based on the ion-dipole interaction between the cation and the negative dipoles of the oxygen atoms in the ring.[86]

3.2. Experimental Methods

3.2.1. High Vacuum Analytical Tribometer

Usually tribology tests are carried out in ambient conditions, several factors, especially the humidity will affect the tribo-behavior of the samples. In order to avoid the effect of water vapor, the high vacuum tribometer has been used. The high vacuum tribometer has been designed to provide controlled vacuum conditions or special gaseous environments. The system contains a vacuum chamber, tribometer, and other accessories, such as heating stage.
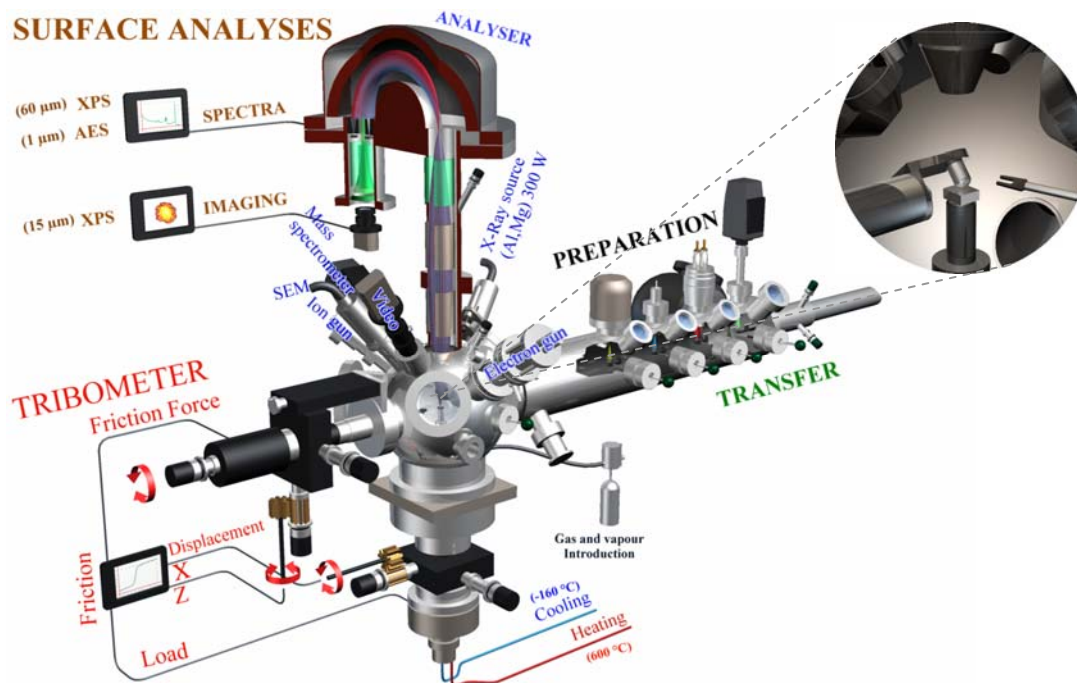
Figure 3.5. High vacuum tribometer

In the experiment, we used the high vacuum analytical tribometer[87] at Ecole Central de Lyon, as shown in Figure 3.5. The pin-on-disk tribometer is located at the center of the vacuum chamber and surface analytical tools are at the top. The vacuum chamber can achieve a pressure as low as 10^{-7} mPa. The system was well designed to not only include the heating (up to 600°C) and cooling (down to 160°C) functions, but also equip with various characterization techniques, such as Scanning Electron Microscopy (SEM), X-ray Photoelectron Spectroscopy (XPS), Auger Electron Spectroscopy (AES), and Mass Spectroscopy.

The tribometer used is a reciprocating pin-on-disk friction tester. The disk is fixed on a vertical shaft attached to an XYZ manipulator. The XYZ manipulator is used to locate the disk position. A Linear Variable Differential Transformer (LVDT) has been developed to measure the force between 0.01 N and 5 N in the vertical direction (calibrated with standard weights). Another quartz force transducer is used to measure the force between 0.005N and 5 N horizontally. The pin moves in a linear reciprocating motion. The pin speed was fixed at a slow speed of 0.1 mm/sec. The friction data was collected in such a way that the friction at low speed towards the two ends of the friction track was not recorded.

The integrated XPS consists of a VG 220i spectrometer using monochromatic Mg-Kα line for measurement. The emitted photoelectrons are detected using a hemispherical analyzer at a passing energy of 20 eV for the *C 1s* XPS peaks. The energy resolution of the instrument at 20 eV is 0.05 eV as estimated from the full width at half maximum of the XPS *Ag 3d$_{5/2}$* of a pure silver target.

In the experiment[17], energetic Ar ions of 5 keV were generated using the ion gun integrated. The DLC samples were treated with energetic ions with different amount of time, 1 min and 10 min. After the treatment, the samples were characterized using XPS to analyze the carbon hybridization states change on the surface of DLC. Then the in situ friction tests were conducted by using the reciprocating pin-on-flat tribometer inside the same vacuum chamber.

3.2.2. X-ray Photoelectron Spectroscopy (XPS)

X-ray photoelectron spectroscopy (XPS) is a quantitative spectroscopic technique that measures the elemental composition, empirical formula, chemical state and electronic states of the elements.[88] As shown in Figure 3.6, the instrument consists of: a vacuum chamber, an X-ray source, an electron energy analyzer, and an electron detection system. A typical XPS spectrum is a plot of electron intensity versus (y-axis) the binding energy (x-axis).

The measurement process involves the irradiation of a material with soft X-rays while simultaneously analyzing the photo-emitted electrons which escape from the top 10s atomic layers of the sample surface. Figure 3.7. explains the principle of XPS. Without the incidence of X-ray, the electrons of carbon atom stay at ground state. With the incidence, the core electron (C 1s) will absorb the energy of the incident X-ray, then becomes much more energetic and emit from the subshell. By comparing the incident energy and the measured kinetic energy, we can get the binding energy of this core electron using Eq. (3.1).
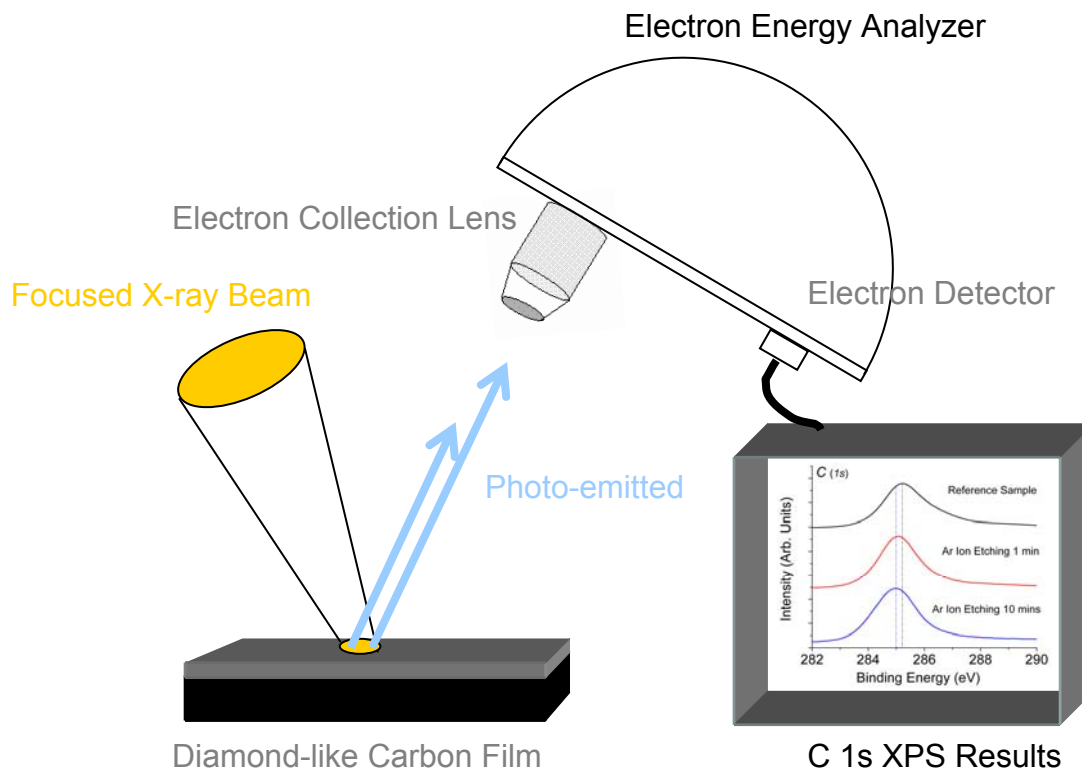
Figure 3.6. Basic components of a monochromatic XPS system

$$E_B = h\upsilon - E_K \qquad\qquad (3.1)$$

Because each element has its own characteristic binding energy in the XPS spectrum, XPS is very accurate on identifying the element on the surface of the material being analyzed. More important, the same element in different chemical environment will have slightly different binding energy (shift of BE). For example, when carbon coordinates with metal to form carbide, C 1s has the binding energy between 280.8 eV and 283 eV; when carbon bonds with sulfur, C 1s has higher value between 285.5 eV and 287.4 eV. With this feature, the shape of measured spectra can be used to provide the

information of the chemical bonds and help to distinguish electronic states on the sample surface.

Photo-emitted Electron (KE=1201.5 eV)

X-ray Beam (KE=1486 eV)

C 2p (BE=5 eV)

C 1s (BE=284.5 eV)

C 2s (BE=9 eV)

(+) Hole
(+) 284.5 eV

Ground State   Excited State   Photo-emitted
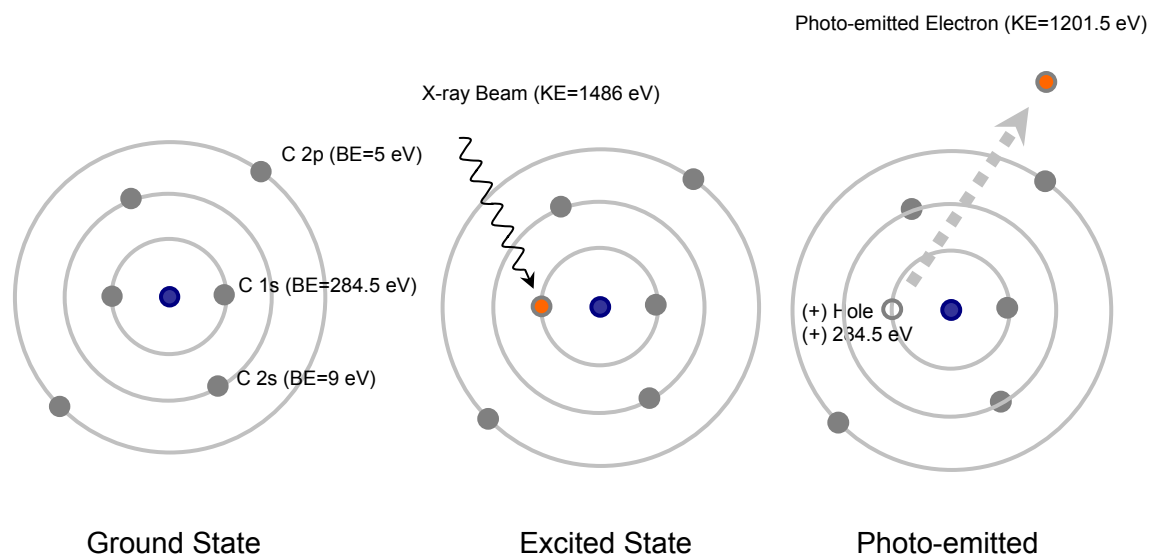
Figure 3.7. Principle of XPS

In the experiments[15,16,89-92], the X-ray photoelectron spectroscopy (XPS) analysis was carried out using a Kratos Axis Ultra Imaging X-ray Photoelectron Spectrometer with monochromatic Al-K_α line (1486.7 eV). The instrument integrates a Magnetic Immersion Lens and Charge Neutralization System with a Spherical Mirror Analyzer, which provides real-time chemical state and elemental imaging using a full range of pass energies. The emitted photoelectrons were detected by the analyzer at a passing energy of 20 eV with energy resolution of 0.05 eV. The incident X-ray beam is normal to the sample surface and the detector is 45° away from the incident direction. The analysis spot on the sample is 0.4mm by 0.7mm, which can be adjusted. The collected data were referenced to C 1s with binding energy at 284.5 ± 0.1 eV.

3.3. Data Analysis Method

3.3.1. XPS Spectrum Deconvolution

XPS is a sensitive analytical tool to study the chemical states on the surface. It provides qualitative and quantitative information about the composition of the sample. By comparing the deconvoluted spectra, small differences in the binding energy of elements due to different chemical environments (chemical shifts) can be identified, which will help us quantify the surface composition, monitor the reaction progress, and further understand the mechanism.

The devonvolution of a measured XPS spectrum usually contains the following steps:

1) Select a spectrum to process.

2) Define the deconvolution regions.

3) Determine and apply the background.

4) Identify possible components.

5) Add and adjust deconvoluted components.

6) Optimize the constrains and parameters of components.

7) Output the results.

For deconvolution process, a critical step is to choose and apply the background. It will help to subtract the contribution of the background noise to the spectrum. There are three approaches to determine the background from the literature: the linear method, the Shirley method, and the Tougaard method. In which Shirley background is the most

common one. For quantitative analysis of polymer spectra, the use of linear background is recommended. The Tougaard algorithm appears to be more successful for treating spectra from metallic systems, it helps to reveal the real peak area usually ignore by the other methods.

After introducing the appropriate background function, we can use the maxima in the spectrum as the clue to the find the position of possible components. A more strict way to do that is via taking the second derivative of the original spectrum. During the deconvolution process, a series of components are generated and placed under the measured spectrum at proper binding energy. The initial line width, line shape, and intensity of each component are determined on the basis of different criteria.

The natural line width is a direct refection of uncertainty for the life time of the core-hole system produced by the emission of photoelectrons. From the uncertainty Principle, the line width of each component can be expressed as:

$$linewidth = \frac{h}{\tau} = \frac{4.1 \times 10^{-15}}{\tau}(eV) \tag{3.2}$$

where h is Planck's constant and τ is the core-hole lifetime. The core-hole lifetime is determined by the decay processes that follow the photoemission, like X-ray fluorescence, Auger process, and Coster-Kronig process.

There are several contributions to the line width, but the associated line shapes are not the same. For our study, two basic line shape function are Gaussian and Lorentzian, where Gaussian distribution corresponds to repeated, independent measurements with random uncertainties, and Lorentzian distribution corresponds to resonant behavior, such as mechanical or electronic oscillation. In the real measurement, the $K\alpha_{1,2}$ photon source

line shape is essentially Lorentzian, while the overall distribution from the spectrometer is Gaussian. The overall line shape is a complex with Gauss-Lorentzian character. The Gauss-Lorentzian ratio depends on the relative contribution of the instrument. This ratio should be the same for all of the components in the same spectrum.

The relative intensity of each component is strongly depends on the shell where electrons stay and the quantum numbers that label the energy states of electrons. First, the non-s-levels are doublets as a result of the spin-orbit coupling. Using the quantum numbers n, l, s, and j, we can distinguish electrons from one and another. Where n is the principle quantum number, l is the orbital angular momentum quantum number, s is the spin angular momentum quantum number ($\pm 1/2$), and j is the total angular momentum quantum number ($j=l+s$). Thus for the non-s-level electrons, there is $l>0$. There are two possible states, "parallel" and "anti-parallel" of the spin and orbital angular momentum vectors. The relative intensities of these doublets are given by the ratio of their respective degeneracies ($2j+1$), as shown in Table 3.6.

Table 3.6. Spin-orbit coupling and relative intensities of the doublets

Subshell	j values	Area ratio
s	1/2	-
p	1/2, 3/2	1:2
d	3/2, 5/2	2:3
f	5/2, 7/2	3:4

Comparing the sum of the deconvoluted components with the experimental results, we can get a measure of the goodness of deconvolution, and usually it is

expressed as the chi-squared by the least squares method. Now, most of the deconvolution software can do it automatically. By allowing the variation of parameters describing the binding energy position, line width, line shape, and intensity, the deconvolution process can be optimized with further iterations.

Table 3.7. Comparison of the carbon element ratio

	C 1s (C-C)	C 1s (C-O)	C 1s (Carbonate)
Crown Ether Ring Open	63.4%	32.5%	4.1%
Crown Ether Ring Close	48.2%	48%	3.8%
Difference	+15.2%	-15.5%	+0.3%

In our research, the spectrum deconvolution was done using XPSpeak 4.1 software, with Newton's iteration method and 300 iterations. It was performed by using two main components (each being a mixture of Gaussian and Lorentzian) and by approximating the contribution of the background by the Shirley method. An example of 18-Crown Ether-6 is given in the Figure 3.8. Figure 3.8a and b show the C 1s peak deconvolution results of 18-Crown Ether-6 with the ring open and close. For both samples, the first component corresponds to the carbonate, which may be resulted from absorbed CO_2 during sliding; the second component corresponds to the C-O group of the ethylene oxide in the 18-Crown Ether-6; the third component corresponds to the hydrocarbon in the repeating ethylene oxide unit of the Crown Ether. With the deconvolution, we can clearly identify that the 18-Crown Ether-6 with open ring contains less C-O bonds than that of the one with close ring (15.5% less). The quantified result is provided in Table 3.7.
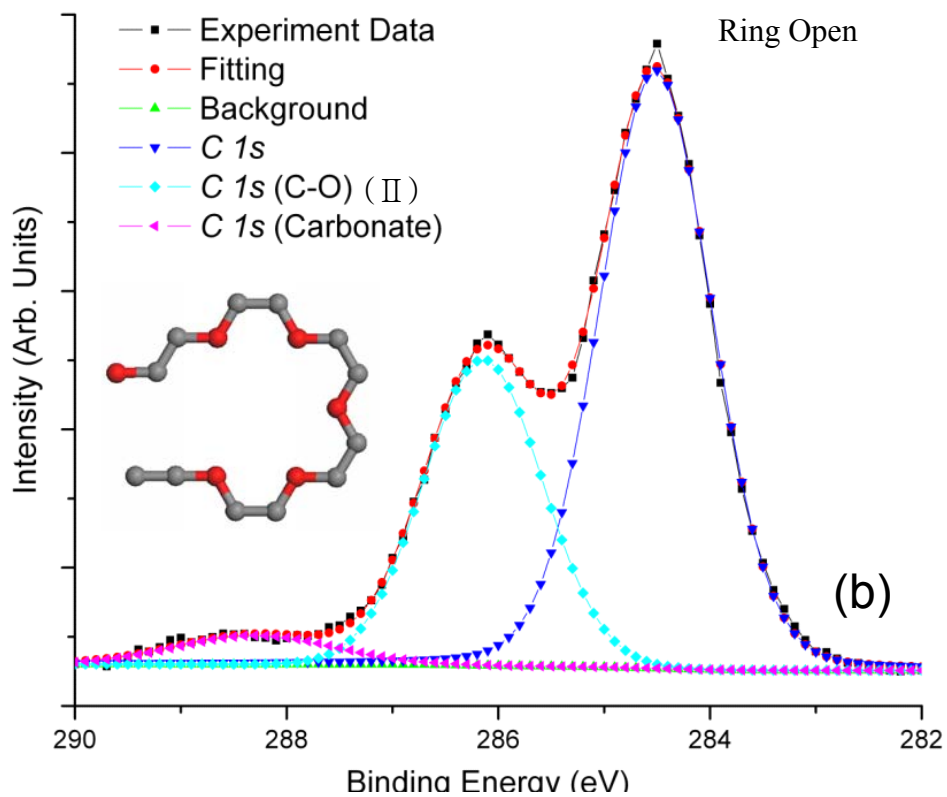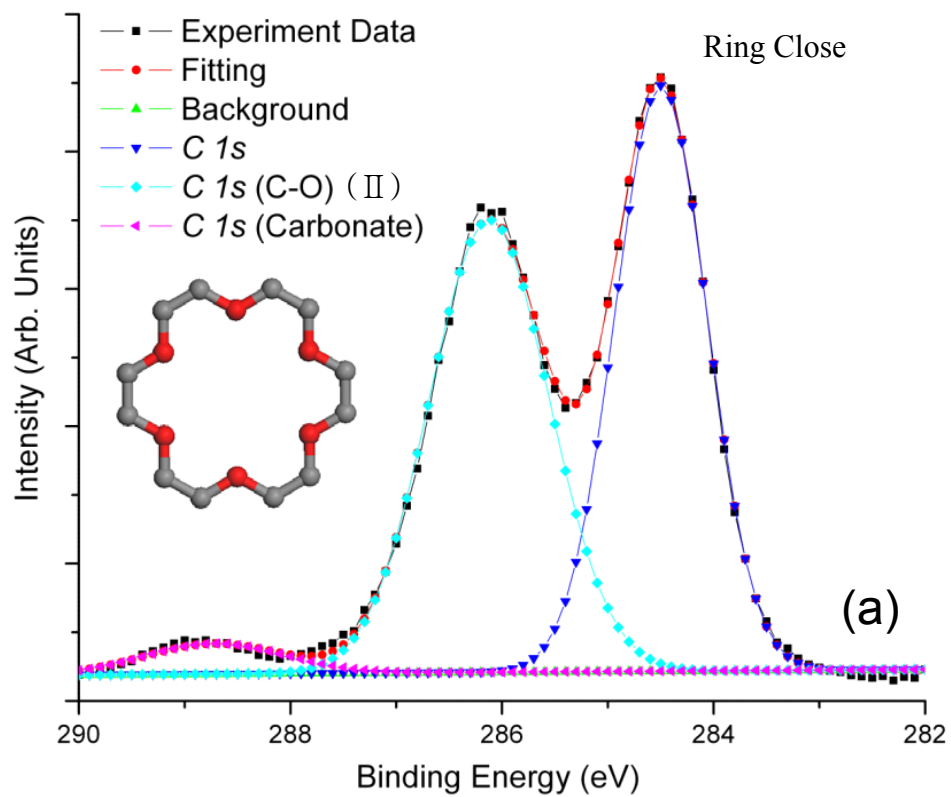
Figure 3.8. Deconvolution results of 18-Crown Ether-6. (a) with ring close, (b) with ring open

CHAPTER IV

COLLISION-INDUCED HYBRIDIZATION STATES TRANSFORMATION OF CARBON IN DIAMOND-LIKE CARBON (DLC)*

In this chapter, the collision-induced hybridization states transformation of a diamond-like carbon (DLC) film and its effect on the friction behavior have been demonstrated. The carbon atom displacements were induced through their collisions with energetic argon ions. The changing ratio of sp^2 and sp^3 hybridization states of carbon dominates the film's friction against the untreated DLC film.

4.1. Diamond-like Carbon (DLC)

For centuries, researchers have been trying to make a "forever" lasting material similar to diamond. The diamond-like carbon (DLC) has become promising to protect microelectromechanical systems (MEMS) with its ultra-smooth surface as a coating.[93-95] The DLC is a mixture of *C* atoms with sp^2 and sp^3 hybridizations.[96] The sp^3 bonding of DLC confers on it many of the beneficial properties of diamond itself, such as high mechanical hardness, chemical and electrochemical inertness. While the sp^2 bonding control the electronic and optical properties.[97] The ratio of sp^2/sp^3 carbon atoms is one of the most significant factors governing the properties of the DLC films. Hydrogen-free DLC with significant fraction of sp^3 content is called tetrahedral amorphous carbons (ta-C).[57]

Energetic ions, like Ar, have long been used to introduce damages in solids to study their radiation resistance in nuclear technology.[98-102] Later on, they were wildly used in the deposition methods for solid thin films, like DLC.[103] In the present study, we introduce energetic Ar ions to modify the electronic structures of carbon atoms on the DLC film surface.[17]

4.2. Collisions between Ar Ions and DLC Hybridization States Transformation

An experiment was conducted to study the effects of collision. Energetic Ar ions of 5KeV were generated using the integrated X-ray Photoelectron Spectroscopy (XPS) inside the vacuum chamber. The DLC samples were bombarded by the accelerated Ar ions with different amount of time (1 min and 10 mins). The XPS and friction tests were conducted *in situ*. The *ex situ* surface morphological analysis was carried out using an atomic force microscope. Further data analysis via multiple-peaks deconvolution of the *C 1s* XPS peak was conducted to reveal the hybridization states of carbon atoms at the sample surface.

The XPS analysis was carried out *in situ* for DLC films with different etching times before the friction test. Figure 4.1. shows the XPS C 1*s* peaks of DLC samples after 1 min and 10 mins ion etching respectively, as well as the reference sample without ion etching. It was found that the binding energy of the measured spectra shifted towards small binding energy direction. From high to low, the values are 285.2eV (reference sample), 285.1eV (sample with 1 min etching), and 285eV (sample with 10 min etching)

respectively. The shift is potentially attributed to a change of carbon hybridization at the top surface and subsequently the binding energy of *C* 1s photo-emitted electrons.
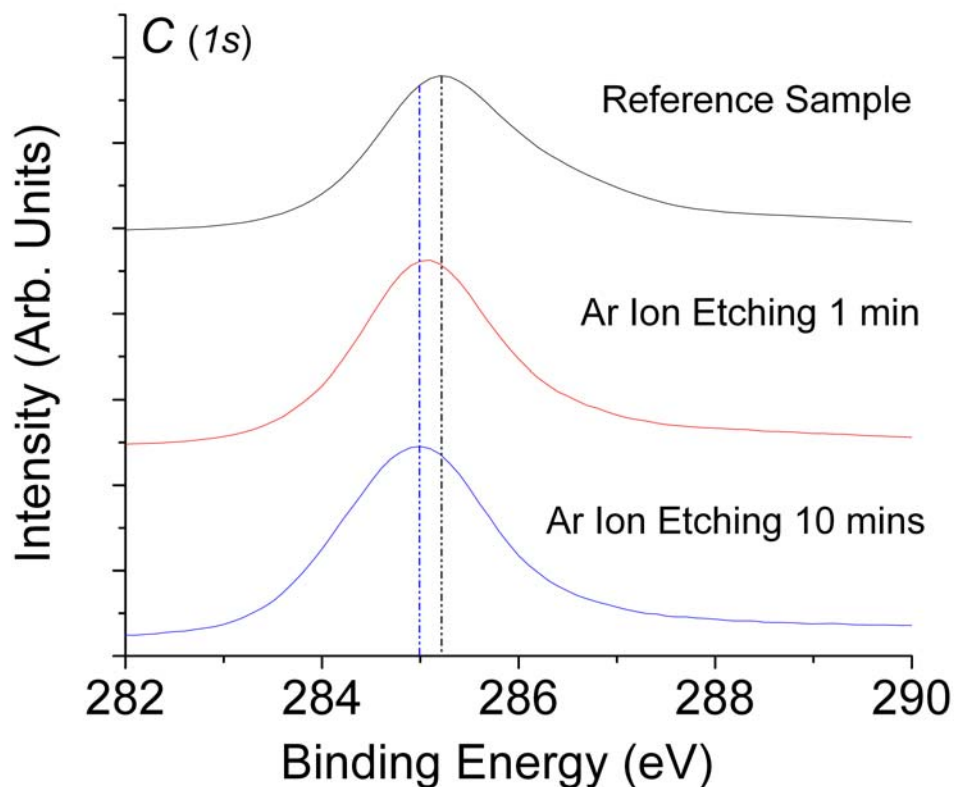
Figure 4.1. XPS *C* 1*s* peaks of the DLC reference sample, samples after 1 min and 10 mins ion etching

The XPS can be used to acquire chemical information within tens of nanometers depth on a solid surface. The XPS' sensitivity in chemical analysis stems mostly from its ability in resolving the chemical identity of the atoms from the measured binding energies.[104] The line-shapes of *C* 1s peak gives information of the chemical bonds. Fitting the peak to suitable functions allows extraction of bonding information.

The spectrum deconvolution was done using XPSpeak 4.1 software, with Newton's iteration method and 300 iterations. It was performed by using two main components (each being a mixture of Gaussian and Lorentzian) and by approximating the contribution of the background by the Shirley method, as shown in Figure 4.2. For our data, all spectra were defined as 20% Lorentzian and 80% Gaussian. The sp^3 peak was fitted allowing both the full width at half maximum (FWHM) and the binding energy to vary, while the sp^2 peak had a variable FWHM but a position fixed at (E_{sp3} - 0.5) eV.[105] The *C-O* peak was also fitted with a variable FWHM, but its binding energy was fixed at (E_{sp3} + 1.3) eV.

In Figure 4.2, the first component is found at 284.7 ±0.1eV corresponding to sp^2 hybrid carbon atoms. The second is at 285.2 ±0.1eV corresponding to sp^3 hybrid carbon atoms. The third peak of much smaller intensity at 286.5 eV is attributed to C-O contamination (C-OH or C-O-C species) due to air exposure. These results are in good agreement with those obtained by Diaz et al..[106] The published results were acquired during deposition process while ours were obtained during etching. The full width at a half maximum (FWHM) of the *C 1s* spectra of the DLC films is about 1.4 eV, which is much larger than that of graphite (FWHM = 0.6eV), and that of diamond (FWHM = 1.0eV).[107] This is attributed to the bonding between environments and DLC film surface of mixed sp^2 and sp^3. It should be reminded that the XPS analysis is for the top few surface layers. The ratios of sp^3:sp^2 from the XPS data fitting will represent the surface.

The sp^3 and sp^2 hybridization carbon atom content was determined as the ratio of the corresponding peak area over the total *C 1s* peak. Consequently, the sp^3:sp^2 ratios can be calculated for each sample. Figure 4.2. shows the sp^3:sp^2 ratio as a function of Ar ion

etching time. The sp^3:sp^2 ratio for sample after Ar ion etching for 10 mins is 1.61; The

sp^3:sp^2 ratio for reference sample is 2.08; The sp^3:sp^2 ratio for sample after Ar ion etching

for 1 min is 2.27, as shown in Table 4.1. The high sp^3:sp^2 ratio on the reference sample

surface is due to hydrocarbon contaminants and adventitious carbon. It is known that this

substance has a low friction less than 0.1. The contaminants were removed as seen in the

reducing CO peak with etching time. The top surface of the ta-C is eventually exposed

giving the highest sp^3:sp^2 ratio (2.274). After etching for 10 minutes, the ta-C surface

transformed to graphitic carbon. Under friction, it is seen that the smaller sp^3:sp^2 ratio,

the lower friction coefficient.

Table 4.1. sp^3/sp^2 ratio of reference sample, samples after 1 min and 10 mins Ar ion etching

Sample	Etching 10 mins	Reference Sample	Etching 1 min
sp^3/sp^2	1.61	2.08	2.27
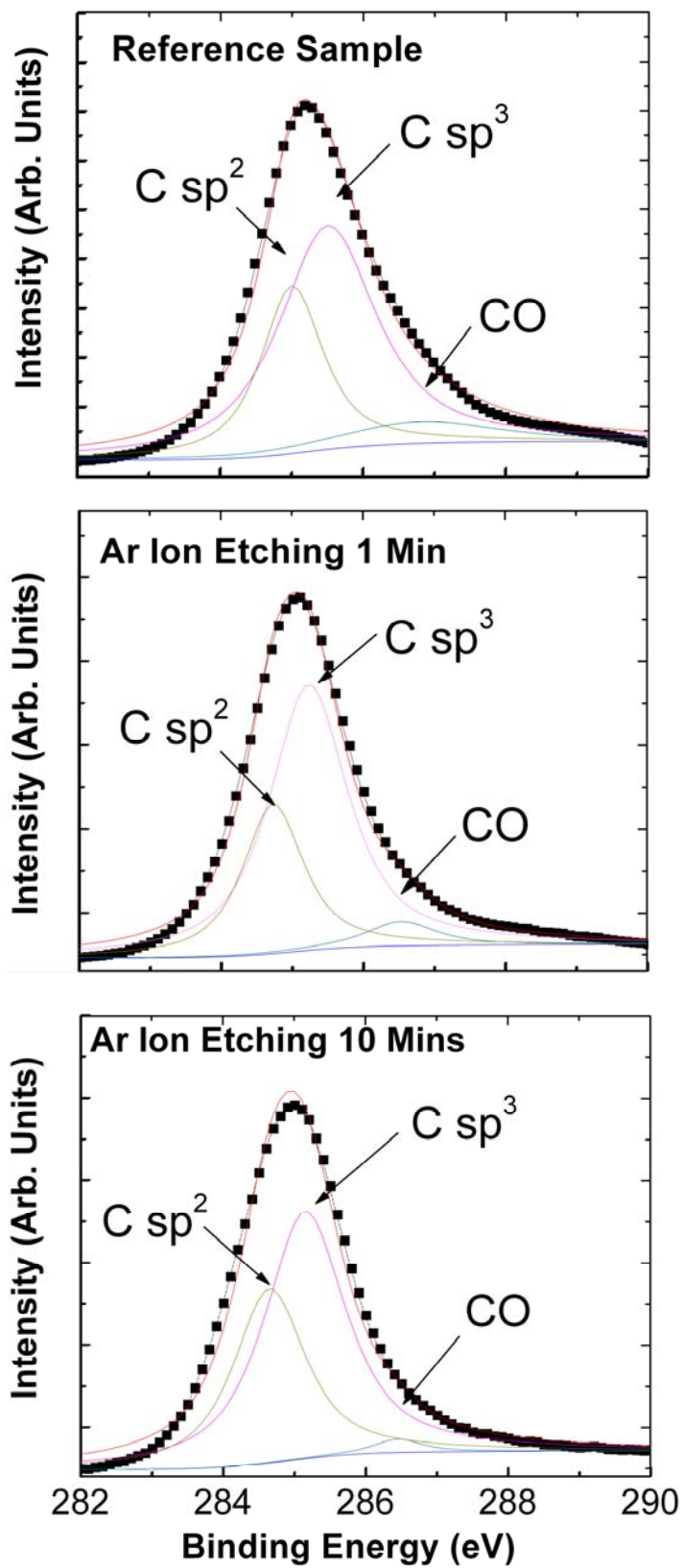
Figure 4.2. Deconvolution of the XPS *C 1s* peaks of reference sample, samples after 1 min and 10 mins ion etching

4.3.   Surface Morphology Characterization

Topographic images of each sample were observed by using an Atomic Force Microscope (Nano-R, Pacific Nanotechnology Inc., USA) in a close contact mode. Surface roughness data was acquired and analyzed using the NanoRule+ (Pacific Nanotechnology Inc., USA). Figure 4.3. shows the AFM images obtained after the Ar ion etching treatments. Surface roughness data are achieved by using NanoRule+, which are shown in Table 4.2.

Table 4.2. Surface roughness of reference sample, samples after 1 min and 10 mins Ar ion etching

	Reference Sample		Ar Ion Etching 1 Min		Ar Ion Etching 10 Mins	
	A	B	A	B	A	B
Ra (nm)	17.1 ± 0.6	9.9 ± 0.2	21.9 ± 0.4	12.5 ± 0.2	25.1 ± 1.2	12.0 ± 0.8

A: Surface roughness measurement of the reference sample and samples of 1 min and 10 mins Ar ion etching; B: Surface roughness of the reference sample and samples with 1 min and 10 mins Ar ion etching after friction test.

The topography and roughness measurements show that as the etching time increases, the surface roughness increases accordingly. This increase, however, does not correlate with friction behavior. It means that the surface roughness shows no visible effects on sliding friction. The surface topography and profile image are shown in Figure 4.3. The topography and roughness measurements were also conducted after friction tests. The AFM analysis was performed in the contact area of pin and disk and images are shown in Figure 4.4. Table 4.2. lists the surface roughness data. Results show that the

surface morphology is changed in the contact area due to sliding. The reference keeps the

lowest roughness among all.
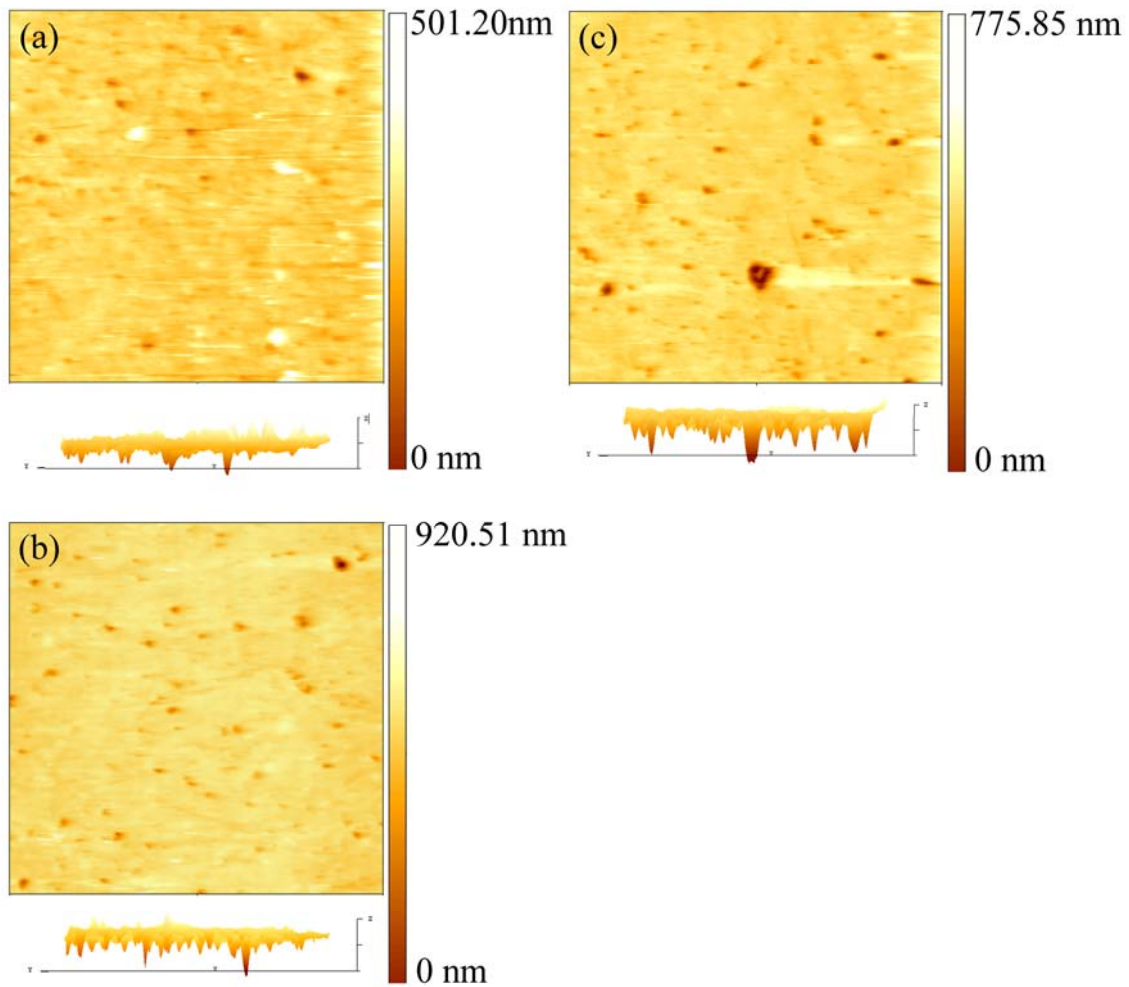
Figure 4.3. AFM images (80um x 80um) and side views were obtained after Ar ion etching treatments, (a) Reference sample without etching. (b) Etching 1 min. (c) Etching 10 mins
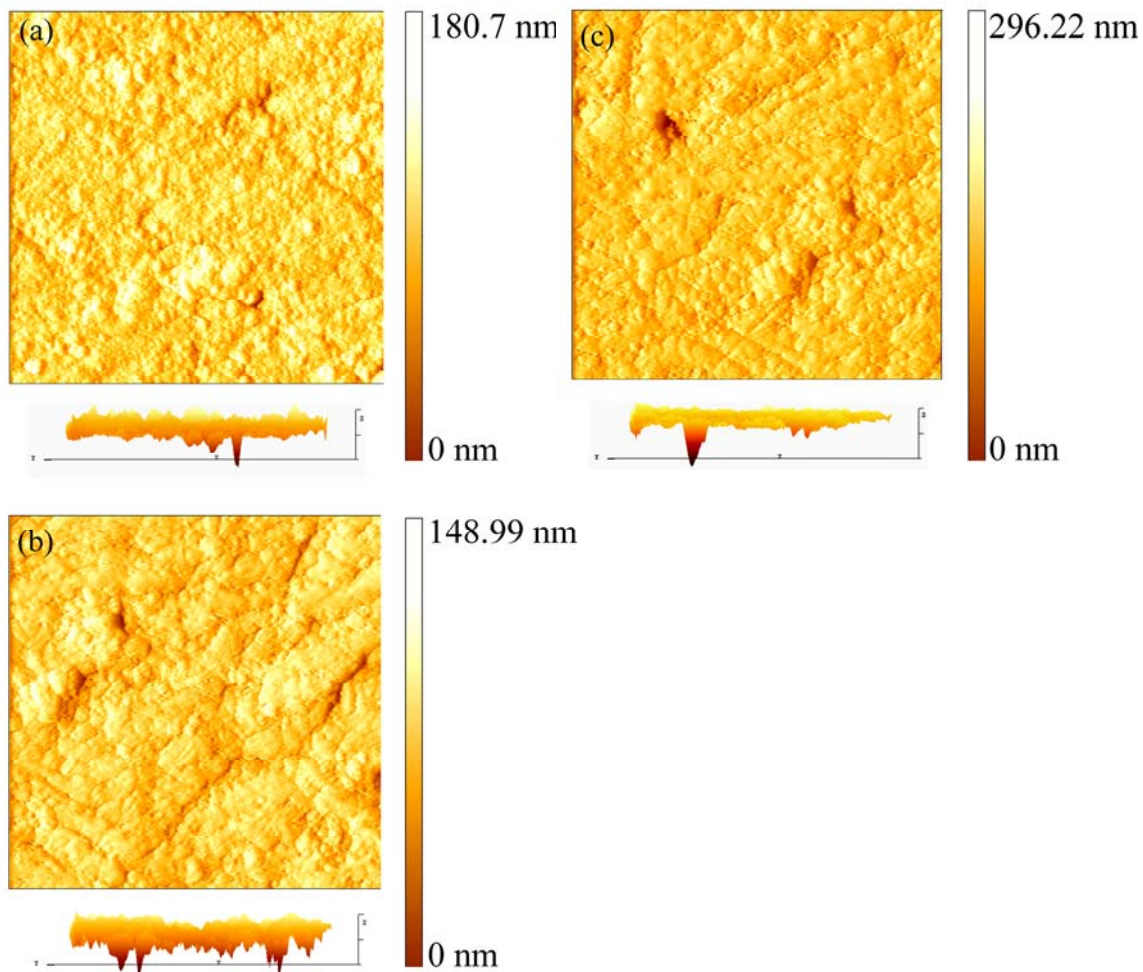
Figure 4.4. AFM images (80um x 80um) and side views were obtained after friction tests, (a) Reference sample without etching. (b) Etching 1 min. (c) Etching 10 mins

4.4. Friction Behavior of DLC Film with Ar Ion Collision

The *in situ* friction tests were conducted by using the reciprocating pin-on-disk tribometer inside the same vacuum chamber. Figure 4.5. shows the *in situ* friction test results in ultrahigh vacuum (UHV). The initial friction coefficient of reference sample is at around 0.15. This is consistent with the observed friction coefficient value of ta-C

film.[108] The friction coefficient of the sample after Ar ion etching for 1 min starts from 0.3 and increases with the number of cycles. The friction coefficient of the sample of Ar ion etching for 10 mins has the lowest initial value 0.03 and it maintains the value till an abrupt change after the 16th cycle. Eventually the friction coefficient reaches the same level as the sample after 1 min ion etching. In both cases, the increase of the friction coefficient after certain cycles clearly indicated changes in the friction contact.
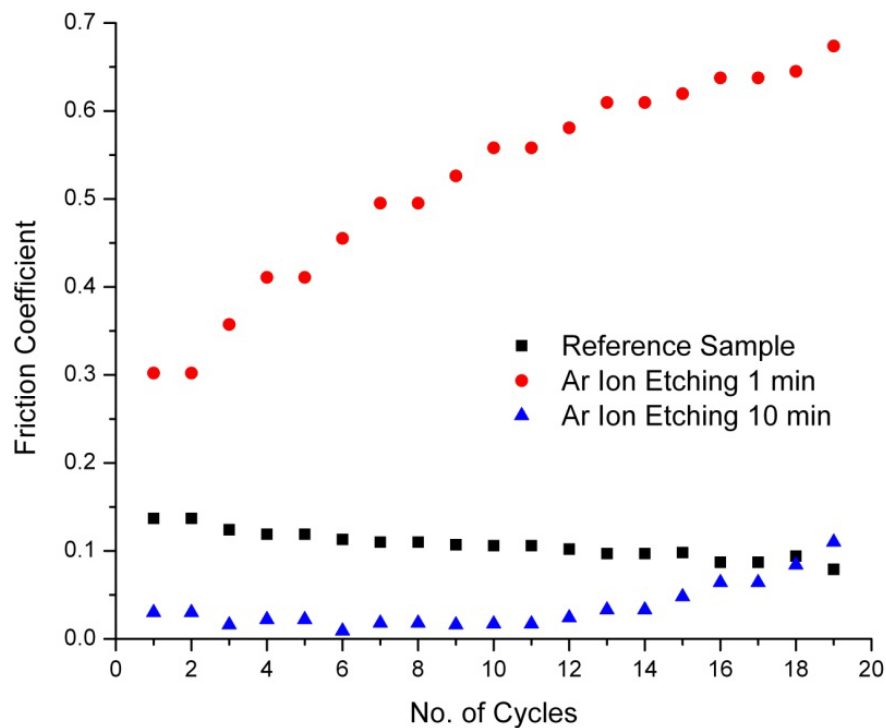
Figure 4.5. *In situ* friction test results of reference sample, samples after 1min and 10 mins ion etching

Could friction and frictional heating induce graphitization? The effects of load and sliding speed on friction and graphitization of DLC have been reported by Liu *et al*. [109,110] It was shown that there was no friction-induced graphitization of DLC when the sliding speed was lower than 60 mm/s at the load of 1 N. They reported that under the

condition of a low sliding speed and load, the graphitization was not observed after a 10 km sliding distance. In the present work, we select the sliding speed at 0.1mm/s and the load at 1 N with a short sliding test (about 0.6 m). Hence with our test condition, friction-induced graphitization is not expected. Thermally induced sp^3 to sp^2 phase transition has been reported to occur at ~500 K for DLC films during deposition.[111-113] Recent theoretical study shows the transformation from ta-C to highly ordered sp^2 material takes place at T_{act}=1,750 K.[114] In the present work, this temperature is not likely to be reached under a low load and speed (1 N and 0.1 mm•s^{-1}). In our experiments, the only variable is the etching time. The stable friction observed on the reference sample indicates that there is no phase transformation observed through either friction or frictional heating.

In collision with the DLC film, the energetic Ar ions exchange momentum with carbon atoms and transfer their energy. If the introduced the energy is larger than the bonding energy between carbon atoms, the knock-on collision will cause the displacement of atoms and trigger the reconstruction on the sample surface. A comparison between the energy introduced by the collision and the bond strength of carbon will be given in Chapter VII.

Overall, with 5 keV impact energies, the C network is sufficiently damaged on the surface that subsequent long-range reconstruction results in predominantly large graphitic sp^2 structures. This leads to the formation of an amorphous sp^2 rich layer on the surface of the film. Graphite-like sp^2 structures have low shear strengths promoting low friction.

4.5. Summary

Using an *in situ* technique, we conducted analysis on a DLC film. The effects of collision on C 1s XPS spectra and the ratio between sp^3 and sp^2 hybrid carbon atoms of the DLC (ta-C) were evaluated. The C 1s spectra were deconvoluted into two well-resolved contributions: one was sp^2 bonded carbon (at 284.7 eV) and the other sp^3 (at 285.2 eV). The results were compared with frictional behavior. It was found that Ar ions roughened the DLC film. However, the roughness increase was not responsible for friction. In stead, we found that the friction of the DLC film against itself depends on the bonding configurations of C atoms. As the ratio of sp^3 and sp^2 hybridization decreases, increased number of C atoms at the interface undergoes phase transformation to form graphitic carbon. Consequently, the friction is reduced. The collision-induced hybridization states transformation of carbon in DLC was confirmed and its effect on the tribo-behavior of the film was further demonstrated.

CHAPTER V

STRESS-INDUCED ANISOTROPIC PHASE TRANSFORMATION OF

POLYVINYLIDENE FLUORIDE (PVDF)*

The application of a mechanical stress can not only vary the hybridization states of atoms, but also can induce rearrangement of molecular structure and phase transformation. A mechanical force, such in a shear form, can alter the symmetry of a molecule or the arrangement of molecules[115] and result in the structure transformation. Researchers have studied the decrease of the molecular weight of polymers under mastication or under condition of transient elongation flow. Comparing the molecular weight distribution of polymers, e.g., polystyrene, before and after mastication, the result clearly shows that the shortening of polymer chain was caused by the cleavage of C-C bonds in the backbone under an external force.[116,117]

In this chapter, we investigate the time-dependent and anisotropic phase transformation of poly (vinylidene fluoride) (PVDF) under bending. Using combined techniques of an Atomic Force Microscope (AFM) and a Fourier Transform Infrared Spectroscope (FTIR), observation of surface morphology and phase transformation in time was made. Results showed that bending stress induces the transformation of amorphous, α, β, and γ crystalline phases. Specifically, the amorphous and α were transformed into the β phase when the bending force was applied.

5.1. PVDF and its Phase Transformation

As a semicrystalline polymer, PVDF has five crystallographic forms, α, β, γ, δ and ε, only the latter four crystalline structures possess permanent dipole moment.[118,119] The dipoles associated with individual molecules are parallel to each other in the unit cell. In which, the β phase contains the largest dipole moment. It also exhibits the strongest piezo-, pyro, and ferroelectric properties.[120,121]

Due to its unique piezo-, pyro- and ferroelectric properties, poly (vinylidene difluoride) (PVDF) has been intensively studied in its physical properties and applications.[122-124] The polar phases can be obtained from non-polar α phase by different processes such as applying tensile stress (α phase → β phase),[73,74] poling under external electric fields (α phase → β and δ phase),[75-77] or annealing at high temperatures (α phase → γ and ε phase).[78,79] And the transformation between crystalline and amorphous phases also exists.[125]

5.2. Effects of Applied Stress on Surface Morphology

In the present work, we used an *in situ* approach to apply a mechanical force on a PVDF thin film. With applied bending force, we characterized the film with techniques, such as Atomic Force Microscopy (AFM) and Fourier Transform Infrared Spectroscopy (FTIR). The effects of stress on microstructure and its subsequent relaxation with time were investigated. Further analysis was conducted in order to correlate the phase transformation and the anisotropy behavior. In the experiments, a special sample holder

was designed to apply the longitudinal and transversal bending deformation while doing the *in situ* AFM and FTIR measurements.

Surface morphology and phase images of each deformed PVDF film were observed by using an Atomic Force Microscope (Nano-R, Pacific Nanotechnology Inc., USA) in close contact mode with Si_3N_4 tips. The scan rate was set at 0.5s/line and each scan took 5 mins.

The *in situ* AFM measurements of PVDF film (100um) under longitudinal bending deformation are shown in Figure 5.1. In the figures, the left are surface morphology images, and phase images , which were collected simultaneously with the topographical images, are given on the right. Phase image can map the local changes in material physical and mechanical properties. The initial AFM scan was performed on the samples as soon as bending was applied, i.e. T = 0 min. Maintaining the same bending deformation, dynamic AFM measurements was continued at a series of time, i.e., 6th min, 13th min, 25th min, 35th min, 43rd min, 61st min, and 68th min. Results are shown in Figure 5.1.

Figure 5.1a is the reference sample prior to bending. The surface morphology (left) and phase (right) images are shown with a scanning area of 20 um x 20 um. The highest peak in the scanned region is 123.3nm. Immediately after the same sample was bent, the AFM scan was performed on a smaller area of 10 um x 10 um at the center region of 5.1a. Results are shown in Figure 5.1b displaying a peak with a height of 750.51 nm. The phase image shows island-like structures. Comparing with Figure 5.1a, both the topographic and phase images confirm there is a drastic surface microstructure change due to bending deformation. This result indicates the surface structure

rearrangement of PVDF with the applied tensile force. In order to track the change, a series of scans were conducted at time (T) of 6th min, 13th min, 25th min, 35th min, 43rd min, 61st min, and 68th min.

Figure 5.1c (10 um x 10 um) shows that after 6 mins, the upper island-like structures were dwindling, but the lower ones were enlarging. The fringes between those island-like structures are less distinctive than that in Figure 5.1b. In the phase image, two piles of "islands" came apart and the upper one eventually disappeared (Figures 5.1d-h).

At the 13th min, shown in Figure 5.1d (10 um x 10 um), the upper island-like structures continued to shrink and the lower counterparts showed a decreasing trend. The fringes became clearer. The transformation in phase is clearly revealed by comparing the phase images of Figure 5.1c and Figure 5.1d. The rest of the AFM scans, given in Figure 5.1e through Figure 5.1i, showed continued dwindling with time. As time went on, the surface morphology change was gradually relaxed. These results confirm the further structural relaxation after the tensile force applied. In order to eliminate the thermal drift in the piezoelectric scanner, six continuous AFM measurements on the reference sample (without bending deformation) were taken under the same experiment condition. Results show that the standard deviation of drift in Z direction is 5.63nm, which is much smaller than the height change observed in relative peak. Our results indicated that under deformation, PVDF sample underwent surface morphology and phase change. The change was time-dependent and possibly related to a phase transformation. We thus continued to verify this using the FTIR.
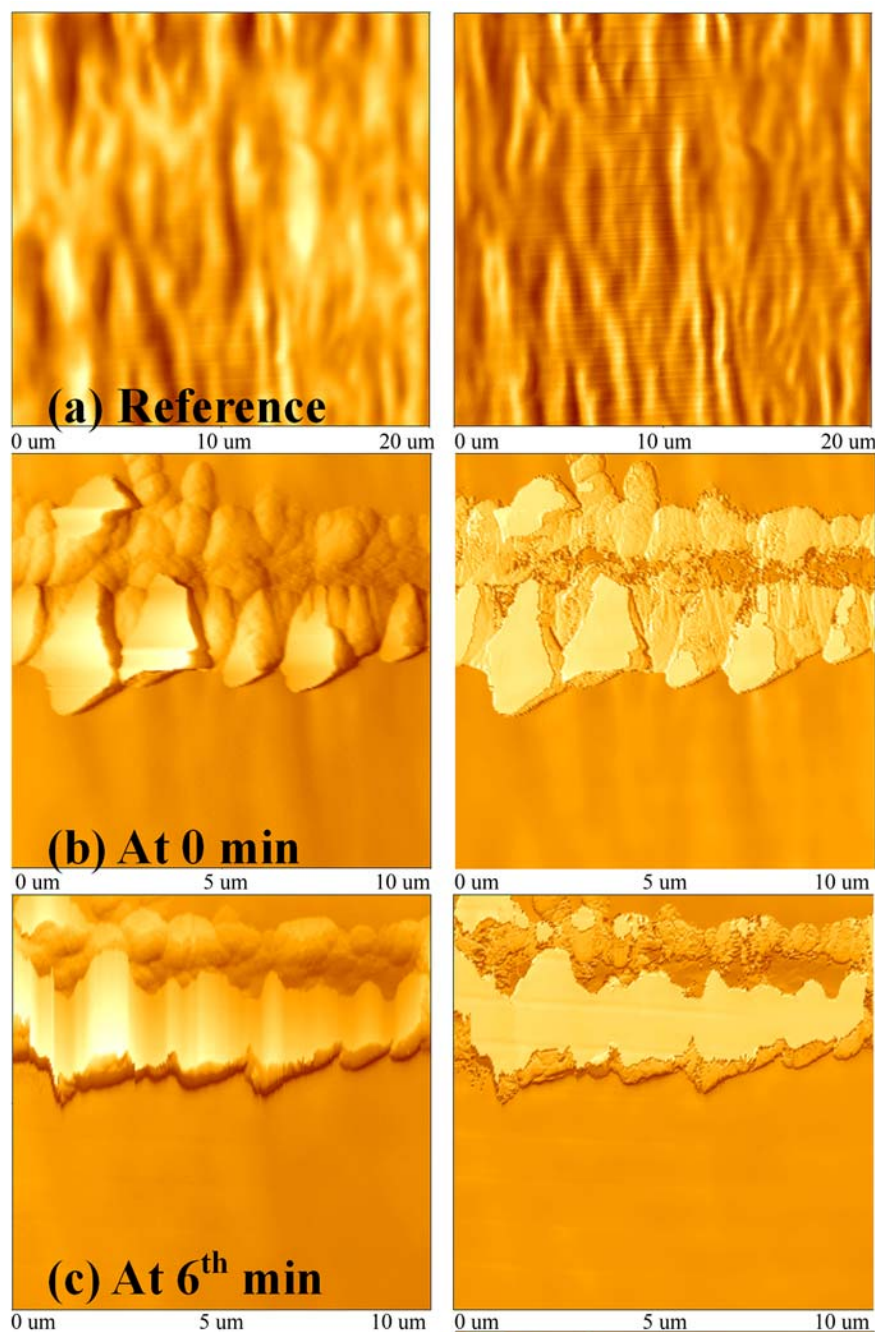
Figure 5.1. AFM scans of PVDF film under deformation at (a) reference sample without deformation; (b) at 0 min (Right after bending force applied); (c) at 6th min; (d) at 13th min; (e) at 25th min; (f) at 35th min; (g) at 43rd min; (h) at 61st min; and (i) at 68th min. *Left*: Surface morphology images; *Right*: Phase images

(d) At 13th min

0 um   5 um   10 um   0 um   5 um   10 um

(e) At 25th min

0 um   5 um   10 um   0 um   5 um   10 um

(f) At 35th min

0 um   5 um   10 um   0 um   5 um   10 um

(g) At 43rd min

0 um   5 um   10 um   0 um   5 um   10 um
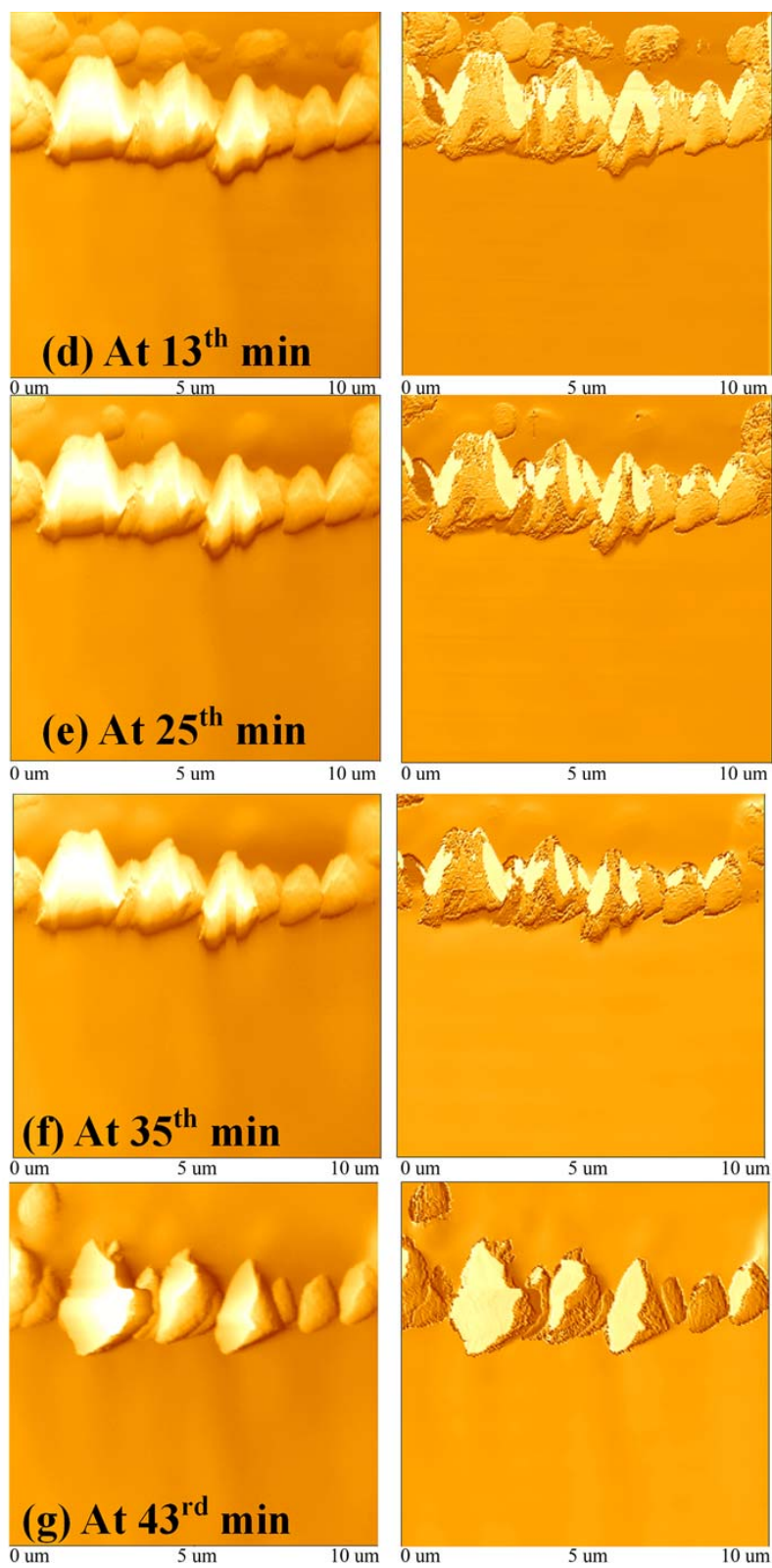
Figure 5.1. Continued
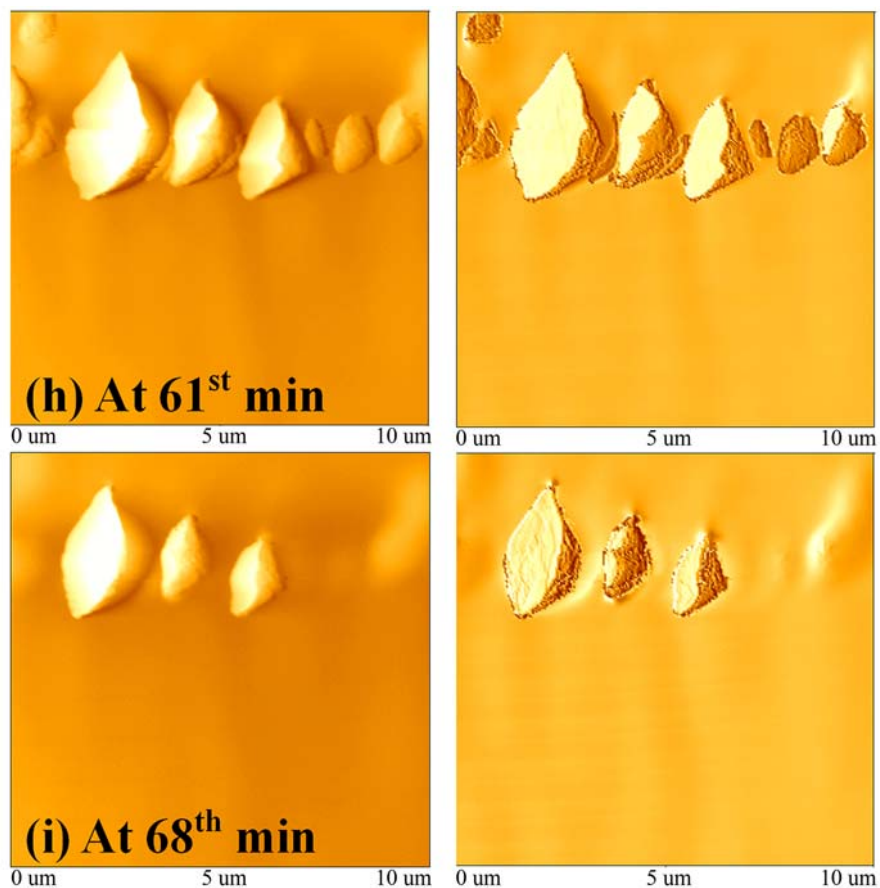
Figure 5.1. Continued

5.3. Time-dependent and Anisotropic Phase Transformation Induced by Stress

FTIR experiments were conducted on PVDF films with longitudinal and transversal deformation induced at room temperature. In order to monitor the time-evolution of microstructures, the measurements were conducted on the sample under longitudinal deformation at T (time) of 0 min, 19 min, and 37 min, as shown in Figure 5.2.

To examine the effect of the anisotropy of PVDF film on its response to bending deformation, another set of experiments were carried out on the same sample under

transversal deformation at T (time) of 0 min and 20 min. Results are shown in Figure 5.3.

FTIR absorbance spectra are given in the range of $400 - 1500$ cm^{-1}.
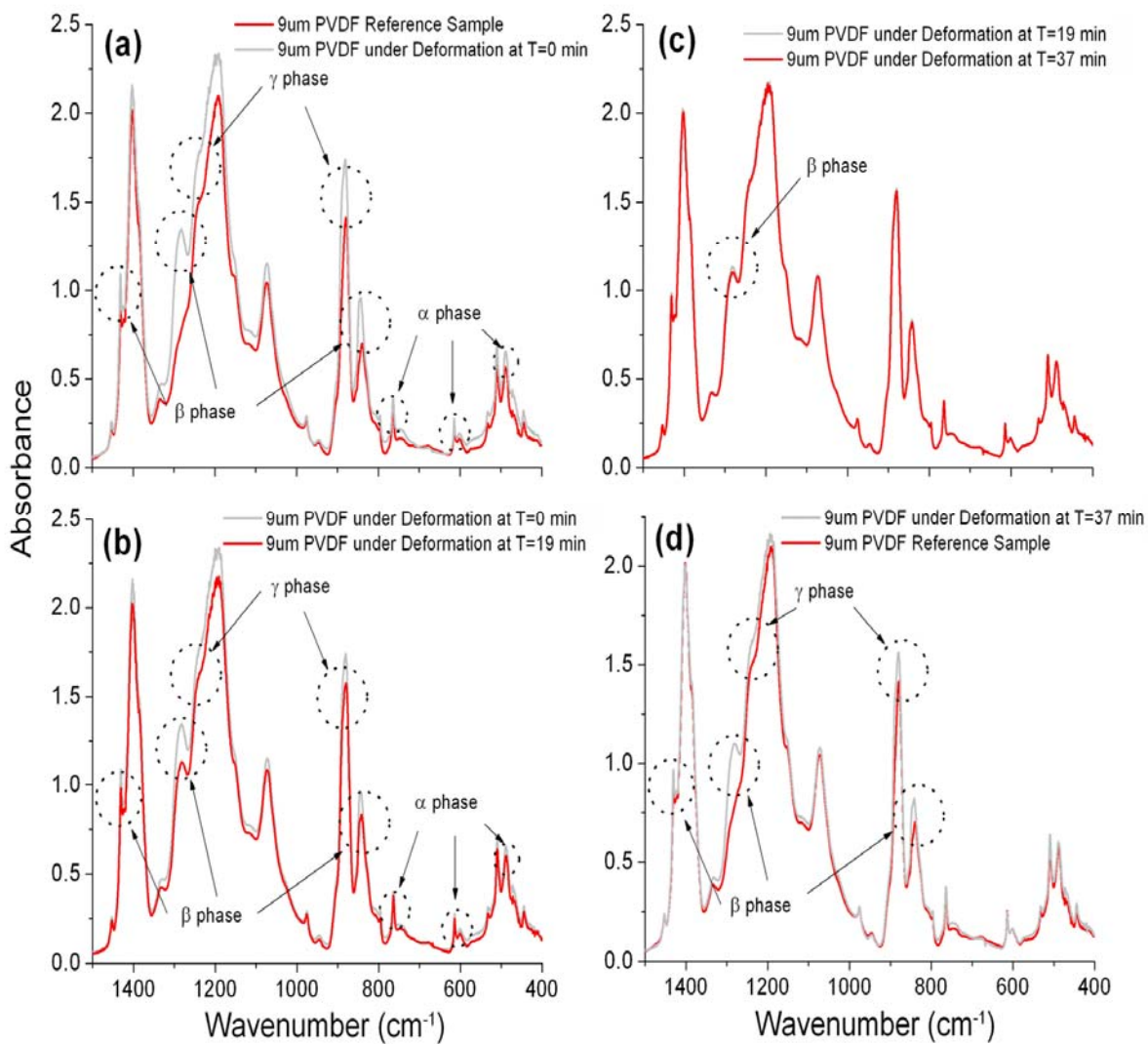
Figure 5.2. Comparison of FTIR results between (a) the 9um PVDF reference sample and sample with bending at T=0 min; (b) the 9um PVDF sample with bending at T=0 min and T=19 min; (c) the 9um PVDF sample with bending at T=19 min and T=37 min; (d) the 9um PVDF sample with bending at T=37 min and the reference sample

The FTIR wave bands in the region from 400 to 1500 cm^{-1} provides the information on the conformational isomerism in the PVDF film, as α, β, γ phase. The characteristic bands of α phase were observed at 763, 615, and 490 cm^{-1}. The absorption band at 763 cm^{-1} is related to a rocking vibration. [126] The band at 615 cm^{-1} is regarded as a mixed mode of CF_2 bending and CCC skeletal vibration. [121,127] The 490 cm^{-1} band is related to bending and wagging vibrations of the CF_2 group ascribed to the α phase. [128,129] The β phase has three representative IR bands at 1431, 1286, and 840 cm^{-1}, in which the band at 840 cm^{-1} is regarded as a mixed mode of CH_2 rocking and CF_2 asymmetric stretching vibration. [130,131]

While the γ phase can be distinguished with its characteristic 1234 and 890 cm^{-1} bands. [77] Figure 5.2a shows the FTIR results of a sample prior to and after deformation. In the figure, the characteristic wave bands of α, β, and γ phases are identified and listed in Table 5.1. The phase transformation is highlighted in the circles and labeled with the corresponding phase, as shown in Figure 5.2a. It is observed that under bending deformation the absorbance intensity of α, β, γ phase increases. The increasing of β phase content is considered most obvious than others.

Table 5.1. Characteristic wave bands of α, β, γ phase of 9um PVDF film observed in FTIR experiments

	α Phase			β Phase			γ Phase	
Wave Number (cm^{-1})	490	615	763	840	1286	1431	890	1234
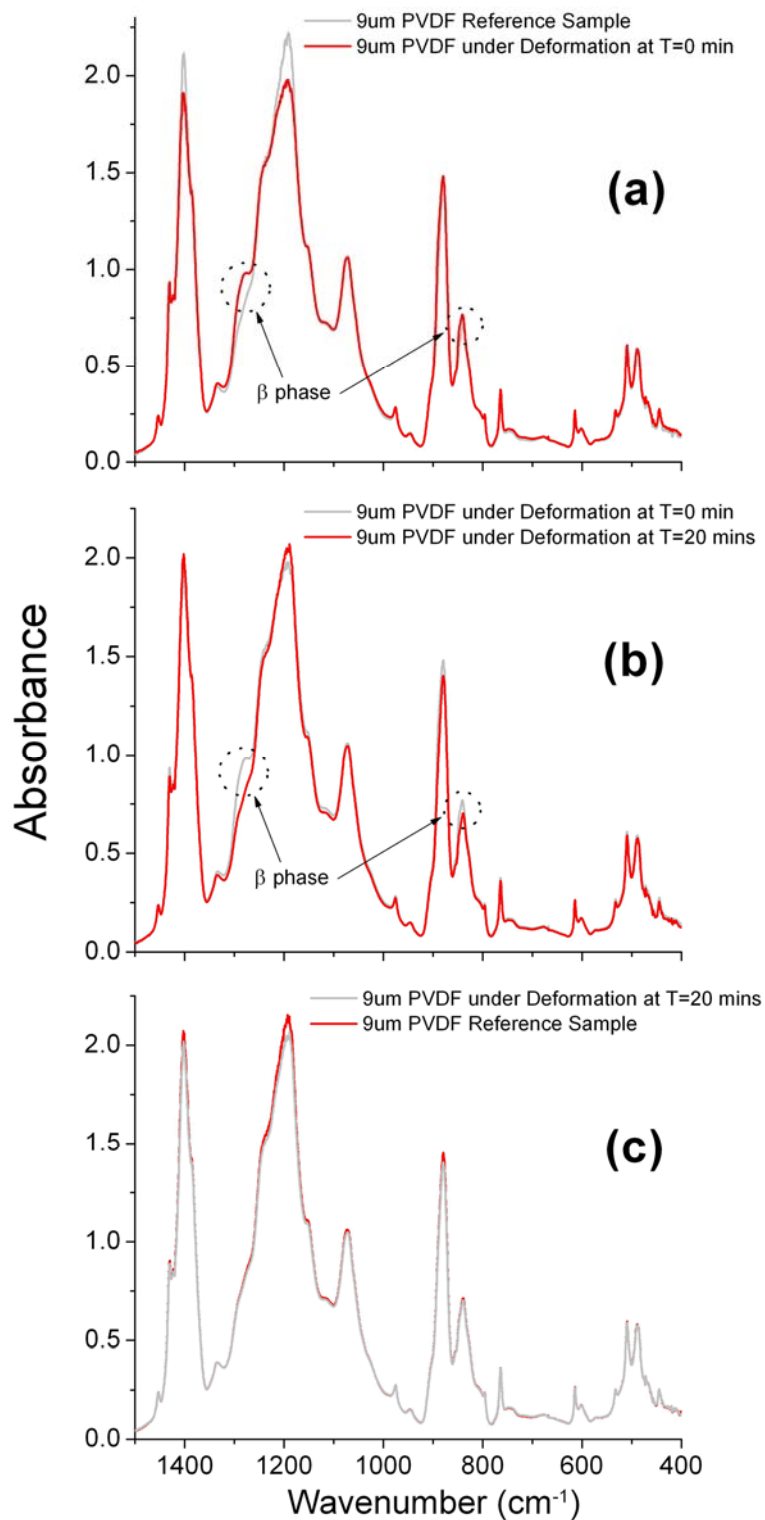
Figure 5.3. FTIR results comparison between (a) the 9um PVDF reference sample and sample with transversal deformation at T=0 min; (b) the sample with transversal bending at T=0 min and T=20 mins; (c) the sample with transversal bending at T=20 mins and the reference sample

According to the FTIR results shown in Figure 5.2 and 5.3, there are two significant peaks at 1396 cm^{-1} and 1194 cm^{-1}. Those peaks had been confirmed to be the amorphous and α phase. [132] Figure 5.3a shows that as β phase intensity increases at 1286 cm^{-1} and 840 cm^{-1}, the intensity of amorphous and α phase decreases at 1396 cm^{-1} and 1194 cm^{-1}. This indicates that there were phase transformation between amorphous and β, also α and β phase.

FTIR result at the 20th min is shown in Figure 5.3b. Comparing with the result at T=0 min, the intensity decrease of β phase is the dominant change. The comparison between FTIR result at the 20th min and that of reference sample is given in Figure 5.3c. Differently from the result shown in Figure 5.2d, the spectra in Figure 5.3c at the 20th min are almost identical to the reference sample. It means the relaxation behavior of PVDF film is also anisotropic.

The anisotropic behavior of PVDF film can be further confirmed by β phase fraction calculation. Based on Beer-Lambert law and the characteristic absorption coefficients of α (at 763 cm^{-1}) and β (at 840 cm^{-1}) phase, the β phase fraction $F(\beta)$ is given as: [133,134]

$$F(\beta) = \frac{X_\beta}{X_\alpha + X_\beta} = \frac{A_\beta}{1.26 A_\alpha + A_\beta} \tag{5.1}$$

Where X_α and X_β are the mass fractions of α and β phases (mass percentage), A_α is the absorption at 763 cm^{-1}, A_β is the absorption at 840 cm^{-1}. The results are shown in Table 5.2 and Figure 5.4.

Table 5.2. Variations of $F(\beta)$ in PVDF film under longitudinal and transversal deformations

	Longitudinal Deformation				Transversal Deformation		
	Reference	T=0 min	T=19 min	T=37 min	Reference	T=0 min	T=20 min
$F(\beta)$	61.18%	65.33%	63.50%	63.28%	60.96%	61.87%	60.72%

Figure 5.4 shows the variations of $F(\beta)$ under different deformation. In both cases, $F(\beta)$ increases as soon as the bending deformation applied. The upper curve is that under the longitudinal deformation and the lower is the transversal one. the only variable in this figure is the bending direction. As seen, under this bending condition, $F(\beta)$ decreases with time. In both cases, the PVDF undergoes a relaxation process with slightly different behavior. For longitudinal deformation, the decrease was observed in the first 19 mins and continued for another 18 mins, then $F(\beta)$ was consent at the 37th min. The increase of $F(\beta)$ is more pronounced in longitudinally deformed directions. It is needed to point out that $F(\beta)$ at the 37th min is larger than that of the reference sample, which infers to the permanent phase transformation under longitudinal deformation. For transversal deformation, the decrease mostly took place at the first 20 mins and $F(\beta)$ reduced to similar value of the reference sample.
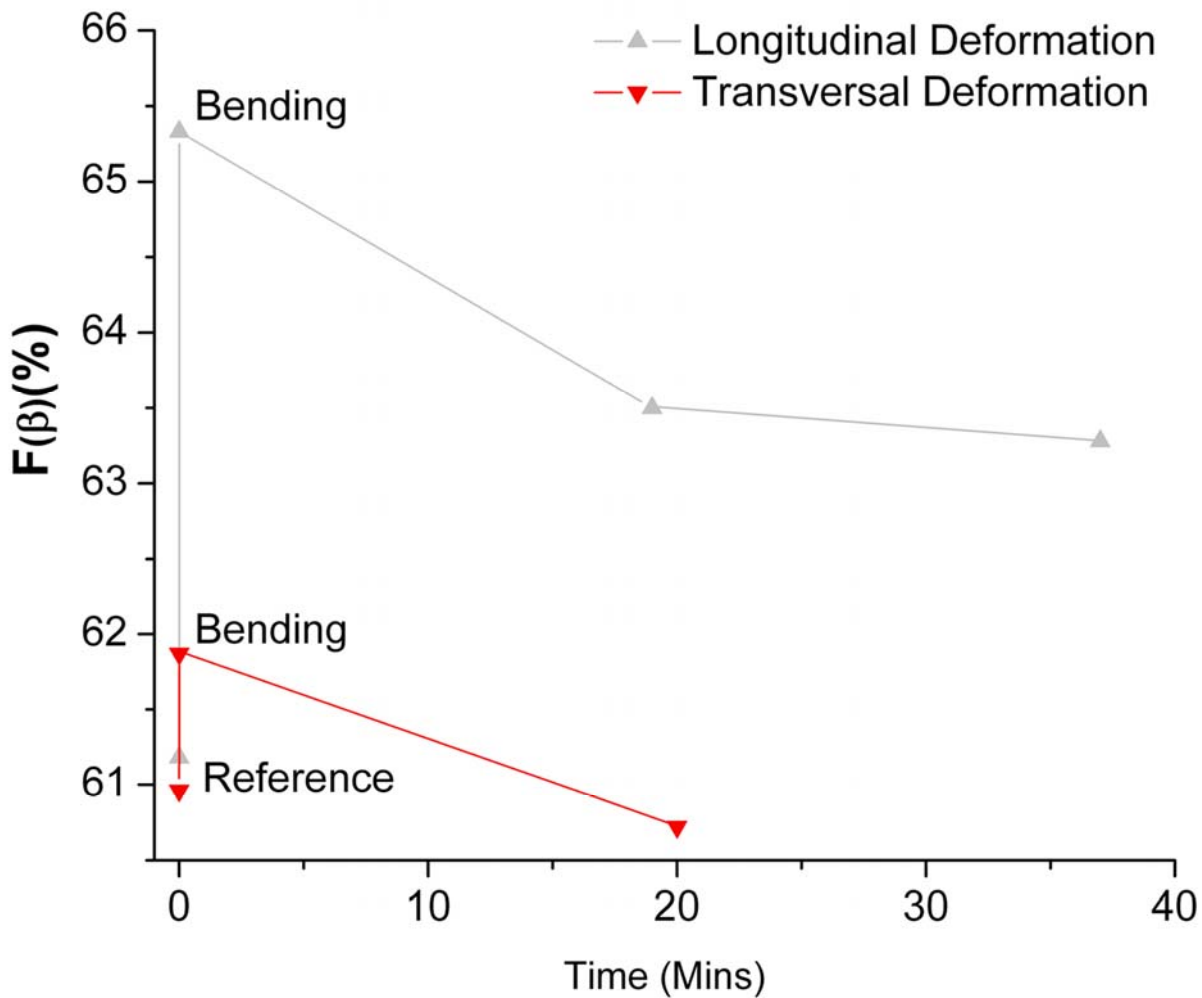
Figure 5.4. Variations of F(β) in PVDF film under longitudinal and transversal deformations

As mentioned in the Introduction, Butyagin explained the effects of mechanical energy on solids using three aspects: structural rearrangement, structure relaxation and structure mobility.[135] These three aspects were all observed in this study. The apparent difference between the surface microstructure of samples with and without stress indicates the structural rearrangement. The time-dependent variation of the surface

morphology and FTIR spectrum further confirms the structure relaxation. The time-evolved transformation between different phases of PVDF and the plotted-out variation of β phase demonstrates that the molecules of PVDF have higher mobility along the chain alignment than normal to it.

Overall, the FTIR results have proven that the PVDF behaves anisotropically under stress. It was found in phase transformation from amorphous to β, α to β phase and subsequent relaxation. The trend of the height change in AFM is coincident with that of phase transformation found in FTIR. Differently from the ceramic piezoelectric compounds, where small ionic groups change their dipole orientation by rotation and/or displacement, the dipoles in polymer system are coupled together by strong covalent bonds. The orientation change in the dipole moments requires cooperative motion of neighboring groups through large-scale conformational changes, which can be induced by external mechanical force. Consequently, it will change the surface morphology of the sample and affect the shape of FTIR spectrum.

5.4. Summary

In the present work, we use an *in situ* approach to apply a mechanical force on a PVDF thin film. With applied bending force, we characterized the film with techniques, such as Atomic Force Microscopy (AFM) and Fourier Transform Infrared (FTIR). The effects of stress on microstructure and time evolution of crystal structure, their (reverse) transformation were studied. We found evidence of bending-induced phase transformation. This transformation was anisotropic and affected surface morphology.

The surface roughness increased due to stress and subsequently reduced with time. Our study contributes to the understanding of the stress-induced phase transformation related piezoelectricity.

CHAPTER VI

FRICTION-INDUCED FORMATION OF SILVER NANOCHAINS*

Besides thermochemistry,[136] electrochemistry,[137] and photochemistry,[138] the mechanochemistry is a fundamentally different branch of chemistry dealing with reactions. It has been reported that a mechanical force can activate covalent bonds in polymers and result in chain scission[19,21,139,140] or guide reaction pathways.[141] The effects of mechanical forces acting on a surface have been studied extensively for decades. In late 1960s, the polishing, i.e., mechanical sliding, was found to smoothen a surface through repacking its atoms.[142] A friction force, due to sliding, has been found to trigger chemical reactions that differ from equilibrium ones.[115,143] Mechanical forces result in the physical motion of an atom.[144] The advantages of using mechanical forces are their superb controllability in either the direction or the amplitude.

In this chapter, a mechanism of mechano-activation using a new approach to synthesize nanochain structures is presented. Silver nanochains (Ag-NCs) were fabricated through sliding Ag against itself in a Crown Ether (18-crwon ether-6) solution. Characterization results showed that the average size of the Ag nodules was 50 nm and the separation distance between nodules was around 10 nm.

Molecular dynamics simulation and experimental results revealed that the formation of Ag-NCs was a synergetic physical-chemical process that involved three competing mechanisms: nucleation of nanoparticle Ag through wear; activation and breaking of covalent bonds through the sliding force; and oxidation and chain formation.

6.1. Silver Nanostructures

In recent years, low-dimensional materials (nano-wires, tubes, and chains, etc.) have attracted great attention due to their superior properties.[145,146] Among those, silver (Ag) nanowires and nanochains are of great interests for their high electrical and thermal conductivity, biological inertness, and distinct surface plasmon resonance (SPR). Ag nanostructures show promise for use in electronic, photonic, and opto-electronic devices. To date, synthesis of Ag nanowires and nanochains has been limited in the method of wet chemistry that involves surfactant and/or amphiphile for growth and anti-agglomeration.[147-150] Understanding of bonding mechanisms and of paths of selective growth in alternative crystallographic planes is yet to be achieved. New approaches, such as mechano-activation, are needed to understand the reaction mechanisms and to achieve precise control in fabrication of nanostructures.

In the present work, we developed a mechano-activation approach to synthesize Ag nanochains (Ag-NCs). This approach not only allows the "control" of chemical reactions via mechanical forces, but also opens new avenues for fabricating chain-like nano-structures.

6.2. Synthesis of Ag-NCs through a Controlled Mechano-activation

In the experiment, we used mechanical force to active chemical reactions of a template consisting of a well defined molecular structure, 18-Crown Ether-6, with Ag. The mechanical motion is found to promote the formation of Ag-NCs. The experiments were designed in such a way that an Ag pin slided on another fixed Ag pin in a reciprocal motion. The sliding length was 0.6 cm and applied static loads were 2N and 5N. The sliding speed was at 1 and 3 cm/sec respectively. The friction force between two pins generates Ag debris with different sizes. The sliding tangential force as friction is monitored through a piezo transducer. The energy induced through friction was controllable through applied force and sliding speed. The 18-Crown Ether-6 was dissolved into DI water to make a solution with a concentration of 37.5%wt. A drop of 18-Crown Ether-6 solution was added between the sliding surfaces every 10 mins during the experiment. At room temperature, the sliding experiment lasted for 30 mins. The remained solution was carefully collected at the interface after the experiment.

The samples for TEM and EDS were prepared by placing a drop of the collected solution onto a carbon-coated Cu grid followed by slow evaporation of the solvent at an ambient condition.

The Transmission Electron Microscopy (TEM) results before and after sliding tests are shown in Figure 6.1. Four images are given here. Figure 6.1a is the Crown Ether before sliding. Figure 6.1b is the TEM image of the sample made at a speed of 3 cm/sec and under 5 N load. Under these conditions the length between nodules is 5 nm and the diameter of the nodules (dark spheres) is around 80 nm.
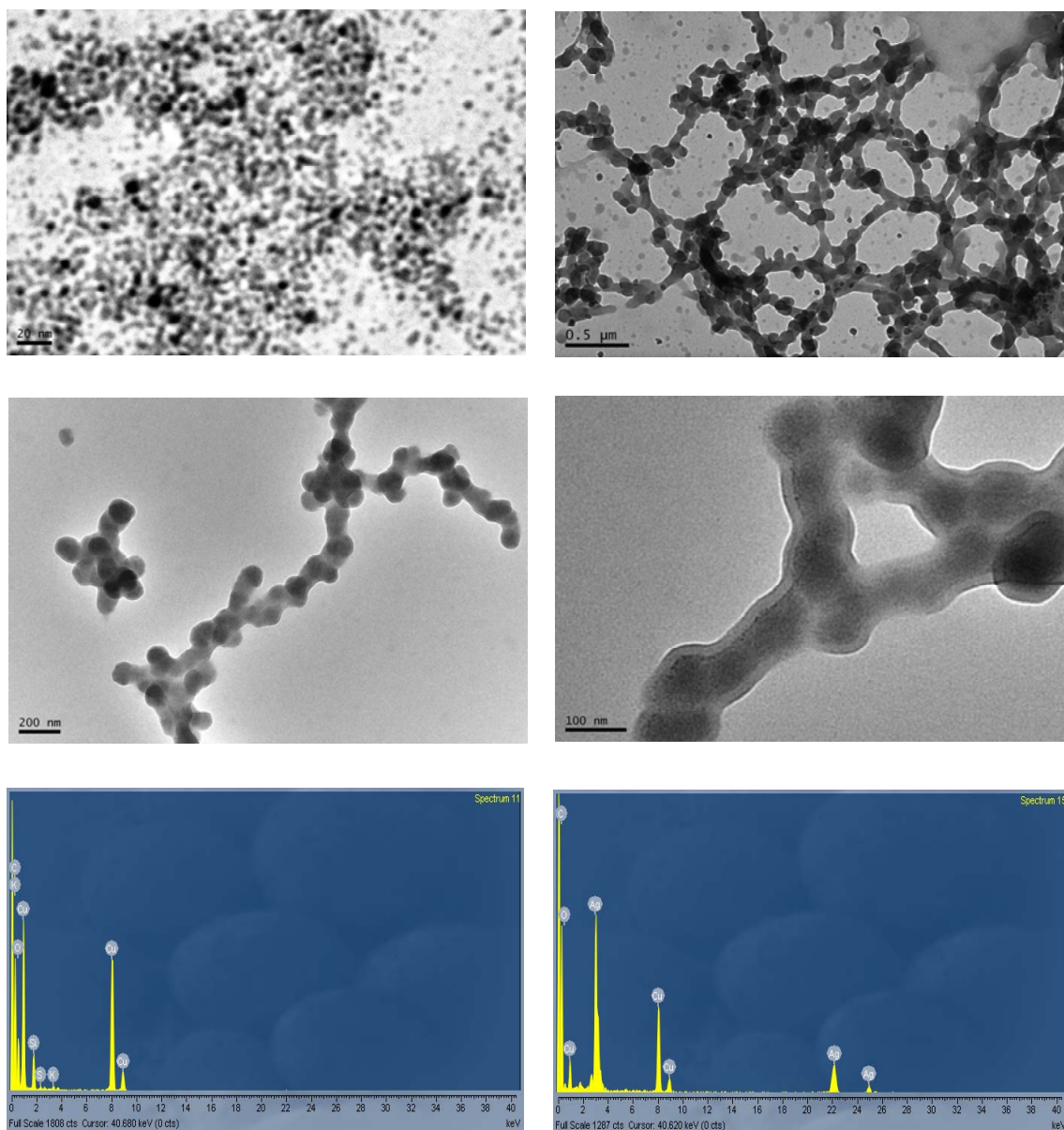
Figure 6.1. TEM images of samples, (a) before (pure 18-Crown Ether-6) and (b-d) after sliding. The EDS spectra are shown in Figures (e) and (f), (e) before and (f) after

In order to determine the chemical compositions of Ag-NCs, we analyzed the nanochains using the Energy Dispersive X-ray Spectroscope (EDS) attached to the TEM at the location of the nodules and chains. Figures 6.1e and 6.1f show the results before (6.1e) and after (6.1f) sliding experiments. Before sliding, the 18-Crown Ether-6

composites copper, oxygen, and carbon. The Cu peak is from the TEM sample grid. The carbon and oxygen are from the Crown Ether. Figure 1f displays new peaks of Ag after sliding. These peaks are from nodules. Other studies on the nanochain structures of Si,[151] SiO$_2$,[152] Au,[153] Ni,[154] and Co[155] had been reported. In those results, nanochains have much longer separation distances between nodules (>10 nm) than ours. The synthesis processes making them are more complicated than that presented in this research.

TEM images of samples obtained under different test conditions are presented in Figure 6.2. Figures 6.2a and b are the TEM images of the sample obtained under the 2N load at the speed of 1cm/s. According to the figure, under this particular condition, the Ag-NCs have an average chain width 35-50 nm and nodules about 50 nm in diameter. In Figures 6.2c and d, the sample was obtained under the load of 2N and at the speed of 3 cm/s. Here, the nanochains exhibit a network structure. The average width of the chains was about 30-40 nm in width with the nodule about 45 nm in diameter. It implies that a high speed decreases the chain length with more network connections than at a low speed. In Figures 6.2e and f, the sample was obtained under the load of 5N and a speed of 1cm/s. Under high magnification, the Ag-NCs are found to be aggregated together. Such aggregation was less at high speeds (Figure 6.1.). Single nanochains were observed under the load of 5N and at the speed of 3 cm/s. Overall, the higher the applied load, the wider the chains. Furthermore, the higher the speed, the more the network connection. The size and shape of Ag-NCs were controllable through processing parameters.
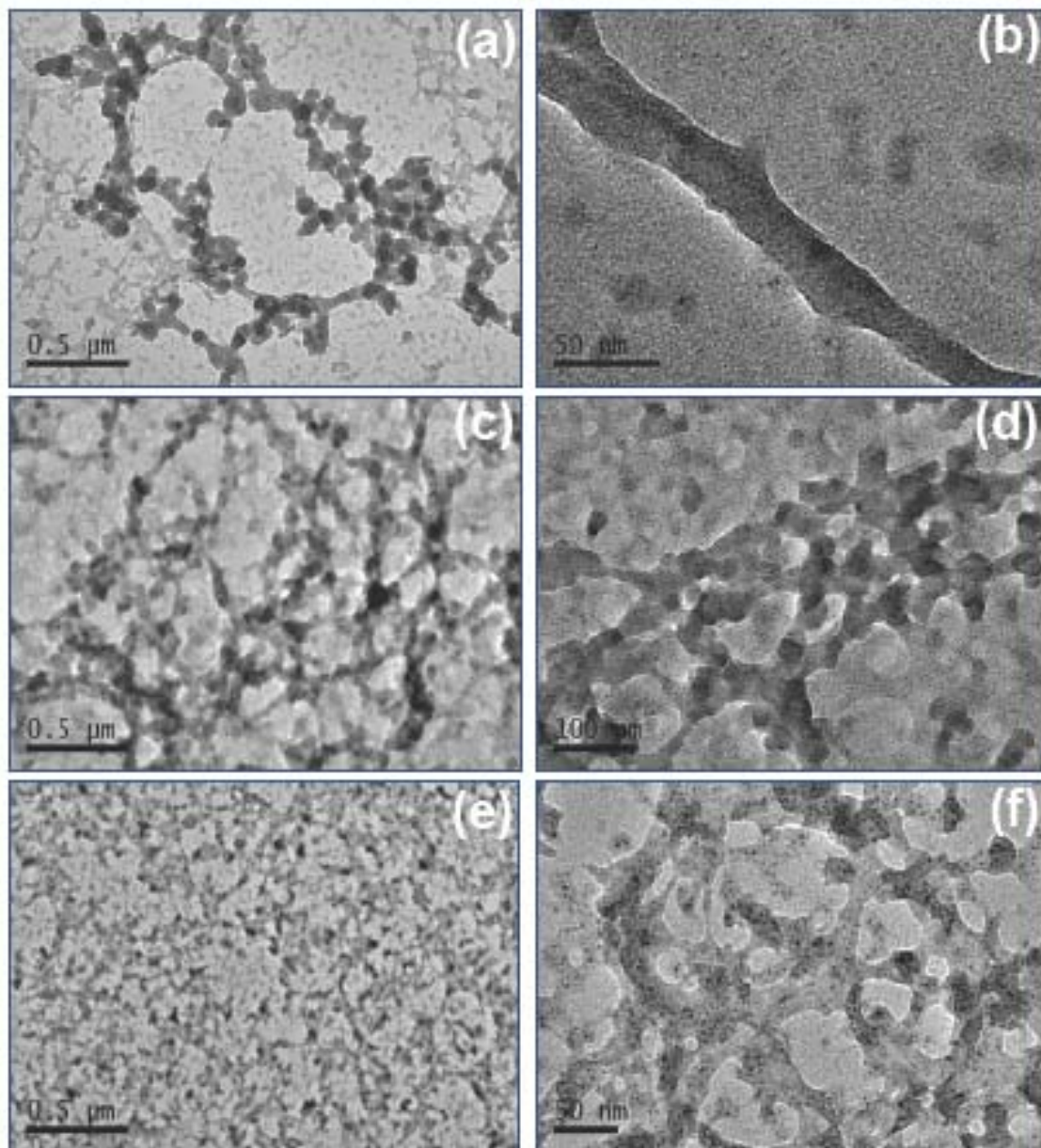
Figure 6.2. TEM images of Ag-NCs obtained under different conditions. (a) and (b) 1cm/s, 2N load; (c) and (d) 3cm/s, 2N load; (e) and (f) 1cm/s, 5N load

To understand the Ag-NCs formation mechanisms, X-ray Photoelectron Spectroscopy (XPS) analysis was carried out focusing on *O 1s, Ag 3d* and *C 1s* peaks. The collected data were referenced to C 1s with binding energy at 284.5 ± 0.1 eV.

Figure 6.3a gives the survey spectrum. Figure 6.3b shows the *O 1s* XPS peak of the pure 18-Crown Ether-6 and of the Ag-NCs. Arbitrary units (Y-axis) are used here in order to compare the binding energies (X-axis). It is found that the binding energy (BE), which corresponds to the maximum peak of O 1s, shifts toward the low energy side; the values are 532 and 531.8 eV. The shift can be attributed to the existence of Ag-O bonds, which is confirmed by the deconvolution of the *O 1s* peak (details given in Figure 6.4.). The variance of BE is consistent with the charge transfer model that the BE of an element with high electronegativity shifts toward the low energy direction in its oxidation state.[156] The results indicate that Ag nanoparticles are linked to each other through Ag-O bonds and then form the chain structure.

Figure 6.3c shows the *Ag 3d* XPS peak of the silver pin and of Ag-NCs. The peak at 374.6 eV corresponds to *Ag 3d$_{3/2}$*; the peak at 368.6 eV corresponds to *Ag 3d$_{5/2}$*. A close examination of the peak shape and position reveals two major differences. The *Ag 3d* peaks for the Ag-Crown Ether sample are broadened and they are not symmetrical. Using spectral deconvolution (details given in Figure 6.4.), we found that there are two sets of overlapping components under the peak envelope. One set with a higher BE is attributed to the metallic Ag; the other set with lower BE is indicative of Ag-O bonds.

Figure 6.3d shows the *C 1s* XPS peaks for the pure 18-Crown Ether-6 and of the Ag-NCs. From left to right, the first maximum peak corresponds to the C-C bond; the second to C-O. For Ag-NCs, we observe that the peak height of C-O bond is smaller and

that of C-C bonds is larger than the reference sample. The results from *C 1s* peak deconvolution (details given in Figure 6.4.) show that the amount of carbon in C-O bonds decreased by 15.5% and that in -C-C- increased by 15.2%, similar in values.
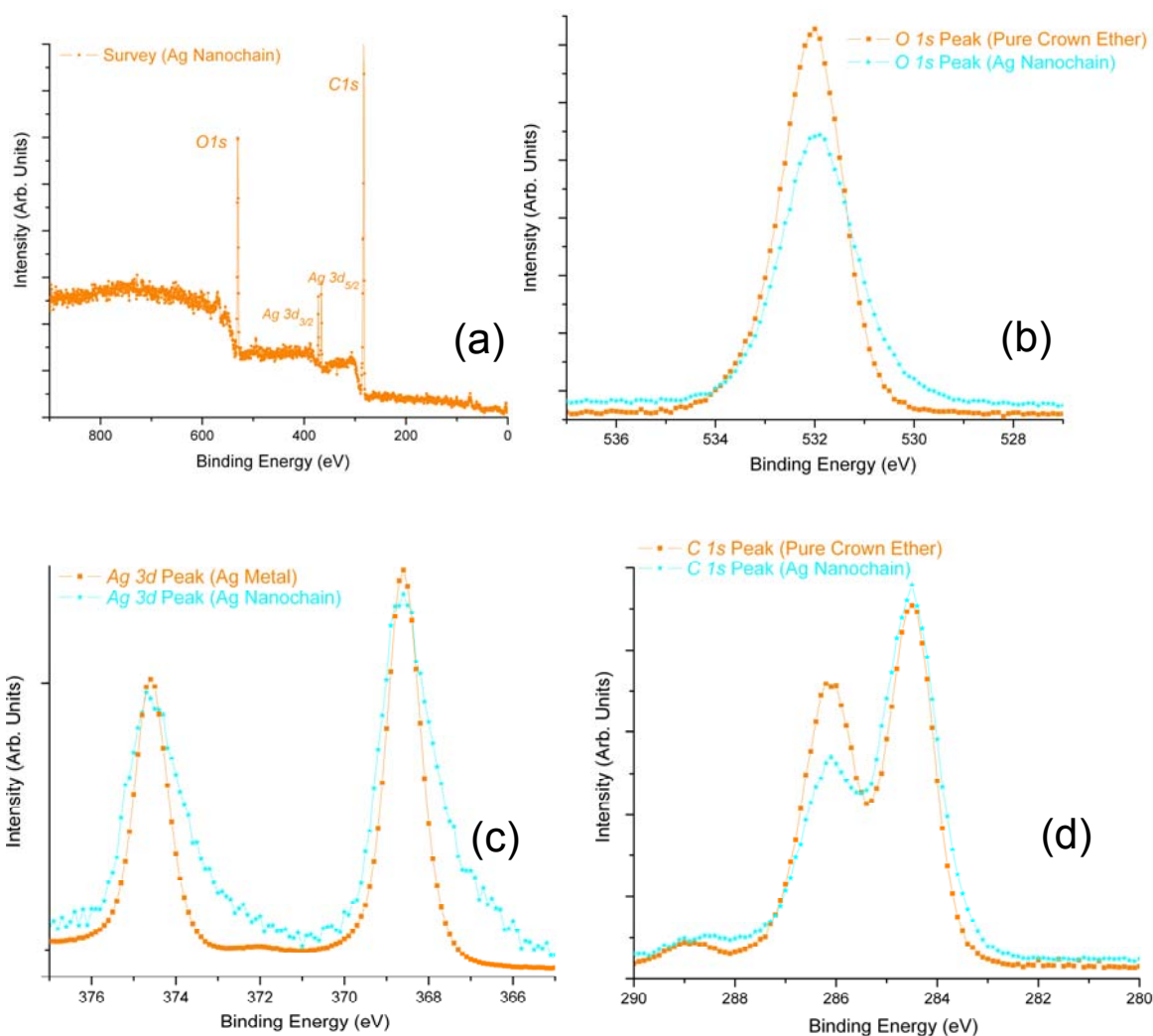
Figure 6.3. XPS analysis of debris samples before and after sliding, (a) the O1s peak, (b) the C1s peak, (c) the Ag 3d peak and (d) the C1s peak

Through further peak deconvolutions, the relative composition of individual element was determined based on the corresponding peak area and its sensitivity factor.

The line-shapes of O 1s, C 1s and Ag 3d peak provided information of the chemical bonds. Fitting the peak to suitable functions allows extraction of bonding information. The curve fitting was done using the XPS peak 4.1 software, with Newton's iteration method and 300 iterations. It was performed by using two main components (each being a mixture of Gaussian and Lorentzian) and by approximating the contribution of the background by using the Shirley method.

Figures 6.4a and b show *O 1s* peak deconvolution results of pure 18-Crown Ether-6 and of the Ag-NCs respectively. For the pure 18-Crown Ether-6, the first component corresponds to SiO_2, which comes from the Si substrate used in the XPS measurement; the second corresponds to the C-O group, which origins from the Crown Ether. The full width at a half maximum (FWHM) for the C-O peak is 1.4eV (peak centered at 532eV) and for SiO_2 1.5eV (peak centered at 533.1eV). Considering the resolution of the XPS of 0.1eV, the FWHM of two bonds were quite similar.

For the Ag-NCs, the first two components are the same as the reference sample, but a new component is observed at the low binding energy side which corresponds to the Ag oxidation. The FWHM for C-O peak is 1.5eV (peak centered at 531.8eV), and for SiO_2 peak is 1.5eV (peak centered at 533.1eV); the FWHM for Ag oxide peak is 1.3eV (peak centered at 530.5eV), which is consistent with the published data.[157,158]

Figures 6.4c and d show *Ag 3d* peak deconvolution results of Ag pin and Ag-Crown Ether sample. For both samples, the first peak corresponds to *Ag 3d$_{3/2}$*; the second corresponds to *Ag 3d$_{5/2}$*. For the Ag pin, the FWHM of *Ag 3d$_{3/2}$* peak is 1 eV (peak centered at 374.6 eV), for *Ag 3d$_{5/2}$* 1 eV (peak centered at 368.6 eV).
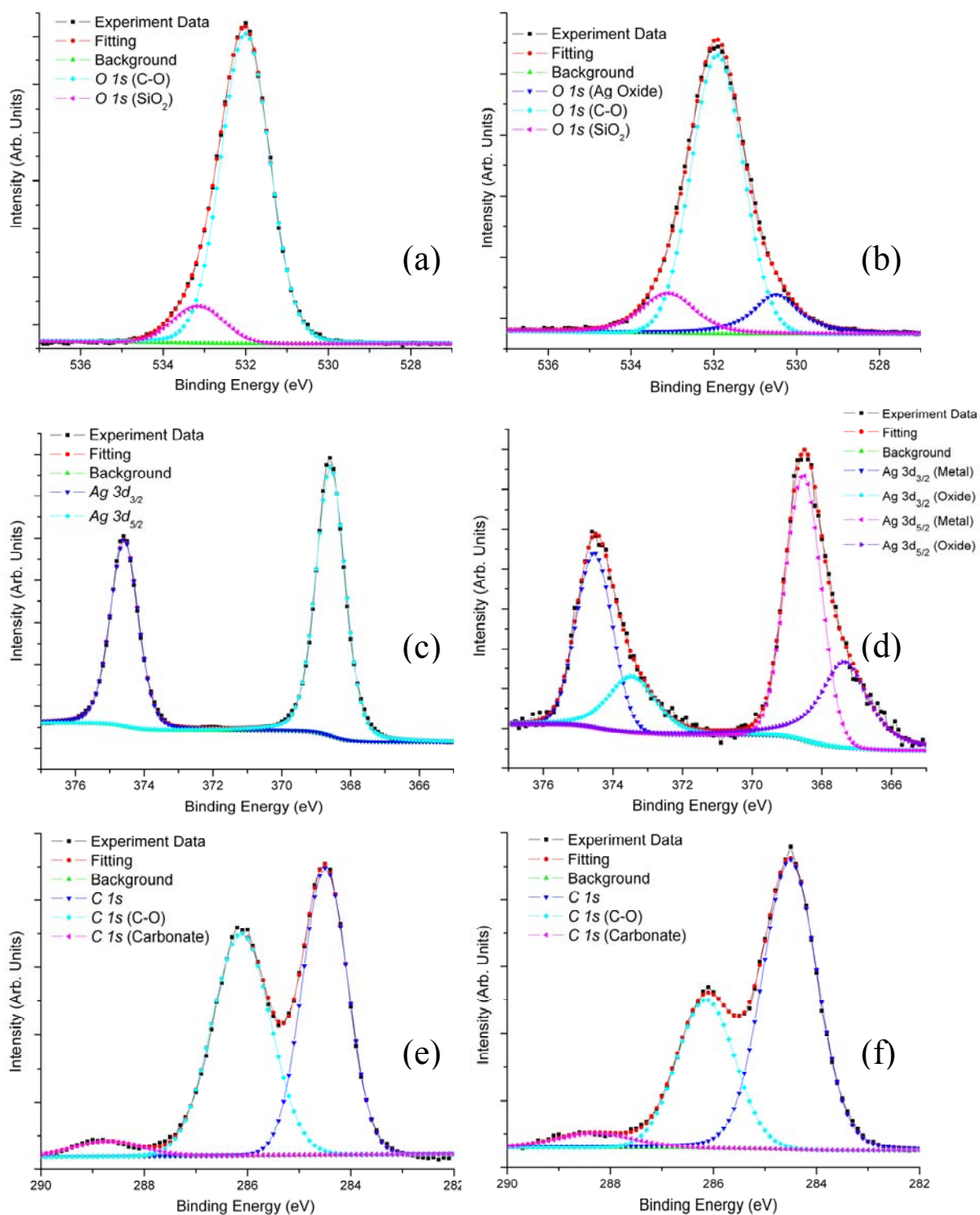
Figure 6.4. Deconvolution of O 1s peak, (a) before (pure 18-Crown Ether-6) and (b) after (Ag-NCs) sliding. Deconvolution of Ag 3d peak, (c) before (pure silver) and (d) after (Ag-NCs) sliding. Deconvolution of C 1s peak, (a) before (pure 18-Crown Ether-6)

For the Ag-NCs, we have identified two sets of *Ag 3d* peaks. One set with a higher binding energy (BE) is attributed to metallic Ag, where the FWHM for *Ag $3d_{3/2}$* peak is 1.2 eV (peak centered at 374.6 eV), for *Ag $3d_{5/2}$* 1.2 eV (peak centered at 368.6 eV). We attribute the broadening of peaks to the existence of Crown Ether. Another set with a lower BE is the indication of the presence of Ag-O bonds, where the FWHM for *Ag $3d_{3/2}$* peak is 1.6 eV (peak centered at 373.6 eV), for *Ag $3d_{5/2}$* 1.6 eV (peak centered at 367.5 eV).

Figures 6.4e and f show the *C 1s* peak deconvolution results of same samples. For both samples, the first component corresponds to the carbonate which may be resulted of absorbed CO_2 during sliding; the second component corresponds to the C-O group of the ethylene oxide in the 18-Crown Ether-6; the third component corresponds to the hydrocarbon in the repeating ethylene oxide unit of the Crown Ether.

For the pure 18-Crown Ether-6, the FWHM of carbonate peak is 1.6eV (peak centered at 288.7eV), for C-O 1.3eV (peak centered at 286.1eV) and for hydrocarbon 1eV (peak centered at 284.5eV).

For Ag-NCs, the FWHM for carbonate peak is 1.8eV (peak centered at 288.3eV), for C-O 1.3eV (peak centered at 286.1eV) and for hydrocarbon 1.3eV (peak centered at 284.5eV). The FWHM and center position of peaks are almost identical to those of the reference sample.

The carbon atom content in different chemical environments can be determined as the ratio of the corresponding peak area after the deconvolution. Consequently, the change of hydrocarbon and C-O content can be calculated for each sample, as shown in Table 6.1. The results show that, due to the friction force, Ag-NCs contains less C-O

bonds than the reference sample (15.5% less). Furthermore, the same complex holds more hydrocarbon than the pure 18-Crown Ether-6 (15.2% more). It implies that with a friction force, a reaction breaking the C-O bonds in 18-Crown-6 ether was initiated. Due to the existence of Ag, the dangling oxygen bonds prefer to interact with Ag atoms through Ag-O bonds, which was confirmed by the Ag-O component in both *O 1s* and *Ag 3d* XPS spectra of Ag-NCs.

Table 6.1. Comparison of the carbon element ratio in different functional groups groups between Ag-NCs (Crown Ether-Ag) and 18-Crown Ether-6 (Crown Ether)

	C 1s (C-C)	C 1s (C-O)	C 1s (Carbonate)
Crown Ether-Ag	63.4%	32.5%	4.1%
Crown Ether	48.2%	48%	3.8%

6.3. Theoretical Analysis on the Formation Mechanism of Ag-NCs

Nanochain structures were observed under different conditions, as shown in Figures 6.1 and 6.2. The size of silver nodules, the separation distance between the nodules, and the shape of the networks indicate the controllability of the formation of AgNCs that has not been reported before.

The chain-shape was related to the contact sliding. The formation of debris rolls, with small aspect ratio, during sliding has been reported in the wear of ceramics and coatings.[138,159] Those rolls were mainly due to mechanical sliding. The oxidation of sliding materials by the surrounding oxidizing gases was found on the debris rolls.[138] The

size of rolls was dependent on the contact stress and sliding speed similar to what we have observed. The sliding motion promotes the formation of rolls. In the present research, continuous and long chains were formed rather than short ones as previous reported. The different between our work and reported results is apparently due to the reactivity of the dangling oxygen bonds in the broken -C-O-C- unit in 18-Crown Ethers-6. In other words, there are mechanochemical interactions in our case. Indeed, TEM observation and XPS deconvoluion have proved that the 18-Crown Ethers-6 segments were reattached together, forming chains. The connecting joints were proven to be Ag nodules. Our experiments produced long rolls with organized structures that are different from previous reported of short ones without any identical structure.

We estimate the amount of mechanical energy introduced through sliding. Using the most conservative condition, at 1cm/sec under the load of 2N, with the test time of 30 minutes (1800 s), the average friction coefficient measured was 0.78. The total work done by friction was calculated as 28.2J.

It has been accepted that in all friction, the vast majority of the energy goes into the production of heat. For instance, the energy needed for mechanical wear is less than 10% of the frictional energy. Now we consider the energy needed to break Crown Ether. For every 150 μl 18-Crown Ether-6 solution (the amount used during tests), in order to break all the C-C and C-O bonds of all the molecules involved, the total energy needed is 0.62 J. Here the bonding strength for C-O is 358 kJ/mol and for C-C is 346 kJ/mol. Comparing this with the input, it is seen that only 22% of the mechanical energy is used to break C-O and C-C bonds. The breaking of 18-Crown Ether-6's ring structure is

illustrated in Figure 6.5. With sliding, segments of Crown Ether chains with different lengths are possible.

Further analysis using molecular dynamics were conducted using the Materials Studio. The simulated possible molecular structures are shown in Figure 6.5. Here, the friction force introduces mechanical energy on the 18-Crown Ether-6 by rupturing the covalent bonds. The formation of Ag-O bonds takes place as soon as the ionized Ag appear. Note that the friction-induced-ionization of metal has been accepted.[160] The effects of external forces on activation energy have been reported in polymers and metal oxides.[161-163] In the present work, the continuous sliding (in reciprocal motion) generates Ag-NCs. The mechanical (sliding) force stimulates the reaction such that the chains are formed. Specifically, the mechanical force activates the covalent bonds and eventually breaks the 18-Crown Ether-6's ring structure. The dangling oxygen bonds subsequently bind with Ag ions. The final size and shape of the Ag-NCs are dominated by the sliding process parameters, such as sliding speed and applied force.
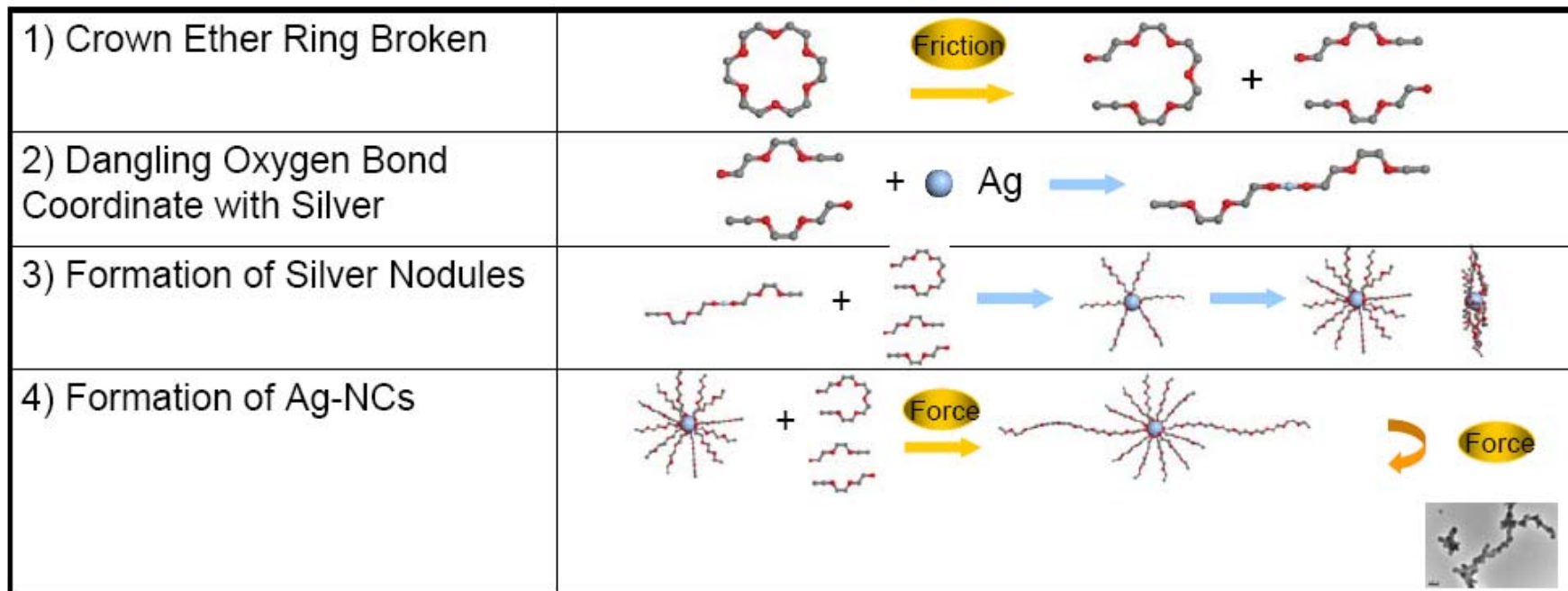
Figure 6.5. Formation of Silver Nanochains

6.4. Summary

In present work, a mechanochemical reaction was found in a sliding system of silver surfaces in 18-Crown Ether-6 leading to production of well-defined Ag-NCs. Molecular dynamic analysis indicated that the formation of such nanochains is energetically possible. The mechanical force not only activated the reaction, but also guided the reaction paths for the formation of Ag-NCs. The approach used here is a simple and cost-effective method to synthesize well controlled nanostructures. The friction force is found to provide silver ions through wear and to promote the formation of nanochains. The metallic nanochains have significant benefits for making nanoelectronic and optical devices.
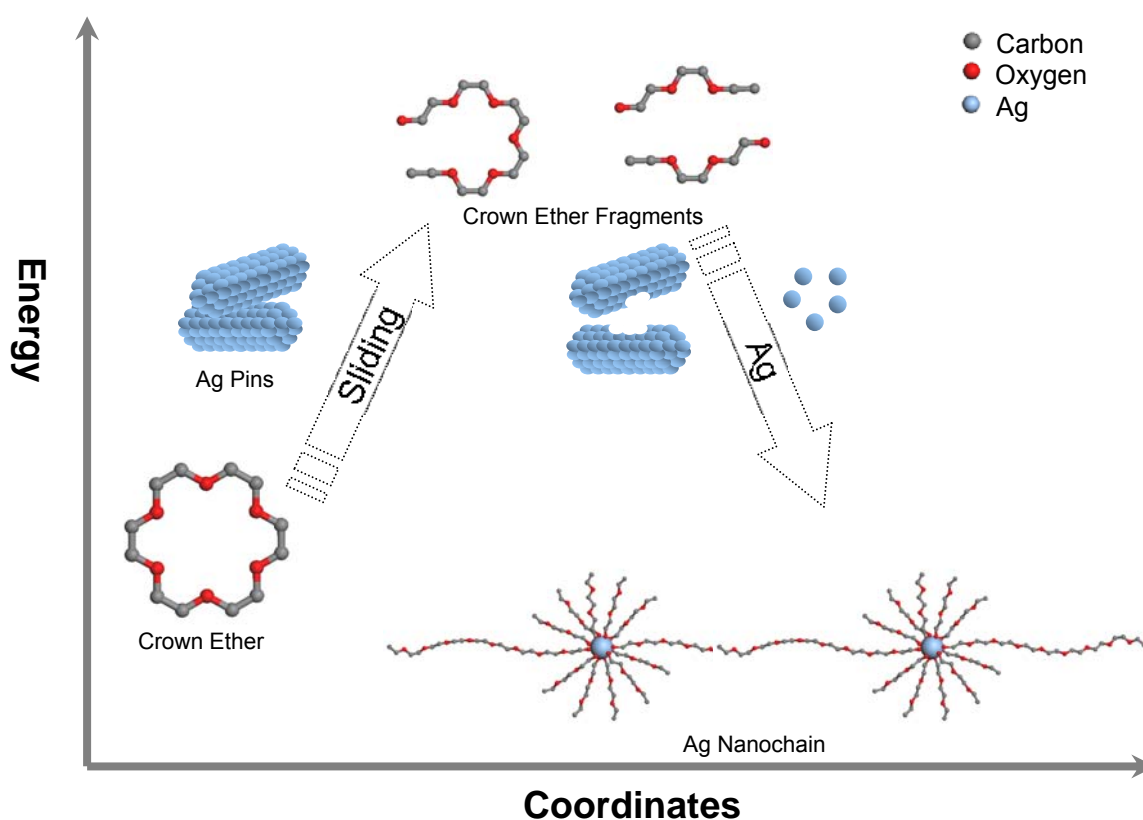
Figure 6.6. Energy diagram for the formation of silver nanochains

CHAPTER VII

MECHANISMS OF MECHANO-ACTIVATIONS

As discussed in the introduction, extensive efforts have been spent to develop understanding in mechanochemistry. From the early Hot-Spot Theory to the Impulse Model, these developed theories and models have improved the understanding on the mechano-activation phenomena. However, fundamental explanation in basics of materials properties related to mechno-activation is still missing. In this chapter, we modified the Lennard-Jones potential in order to discuss effects of an external stress on the energy states of a pair of atoms or molecules. The L-J potential has been wildly used to describe the interaction between atoms or molecules. Comparing with the experimental results, it has been proved to have a good approximation. A simple physical model will be developed here. Experimental results from DLC and PVDF will be used to validate the proposed model.

7.1. Lennard-Jones Potential

For the potential function taken initially as the basis, it is desirable to satisfy the following conditions: 1) proximity to real atoms (accuracy), 2) applicability to different types of atoms or molecules (generality), and relative ease in carrying out the necessary numerical calculation (solvability). One empirical interatomic/intermolecular potential that can satisfy all these three conditions is the Lennard-Jones potential, especially for the multi-body interactions, it is the core potential.

The Lennard-Jones (L-J) Potential is used to describe the interactions between atoms or molecules. For a two-body system, the potential is wildly used in the following form[164,165]:

$$U(r) = \lambda r^{-n} - \mu r^{-6}$$

(7.1)

where r is the distance between the centers of two objects, λ and μ are the coefficients associated with the exchange repulsion force and the dispersion force, respectively. There are $\lambda > 0$, $\mu > 0$, and $n > 6$. The L-J potential will converge to zero at the limit $r \rightarrow \infty$.

The L-J potential contains two types of force acting in opposite directions. One is repulsive and is called the exchange repulsion force, while the other one is attractive and is called dispersion force.[166] Compared the long range force, i.e., Coulomb force between charged particles, these two types of force are defined as short range forces, because they fall off at a much shorter distance than the Coulomb force does. Both of them diminish as the increase of r. Because $n > 6$, the decreasing rate of the dispersion force is always lower than that of the exchange repulsion force. Consequently, the net force between a pair of atoms or molecules is always weakly attractive at a large distance (longer than the equilibrium distance, r_0). As the distance decreases, the net force turns out to be strongly repulsive. This effect plays a critical role in determining the molecular conformation, since it prevents abnormal shortening of the distance.

The first term in Eq. (7.1) describes the exchange repulsion force. As two atoms approaching each other, the electrons which enter the newly formed antibonding orbitals cause a strong repulsive force between the two atoms due to the exchange repulsion (the overlapping of electron orbitals).

The second term in the equation represents the attractive dispersion force. It origins from the interaction of induced dipole moments in the atoms. An atom is composed of a nucleus and electrons that move around the nucleus. Considering a long time average of trajectory, the mass center of electrons may coincide with that of the nucleus, but the nucleus and the electrons never occupy the same position as each other at a given moment. Hence the mass center of electrons does not necessarily coincide with that of nucleus at a given moment, and various patterns of momentary charge distributions may be formed within two interacting atoms in contact. In the absence of any restriction on the movement of electrons, the mass center of electrons of one atom is liable to occupy a position that is close to the nucleus of the other atom. As shown in the Figure 7.1., this oriented charge distribution (Figure 7.1a and b) is more favorable in energy than the oppositely oriented charge distribution (Figure 7.1c and d). Hence, the attractive distribution occurs with a higher probability than the repulsive distribution. Eventually, an attractive force acts between two atoms at a large distance (larger than the equilibrium distance).

In the case where two atoms undergo collisions, the process is slightly different. As two atoms approach to each other, their electron clouds would experience deformation and cause the further deviation between the mass center of electrons and nucleus. The interaction between the induced dipole moments remains as attractive.
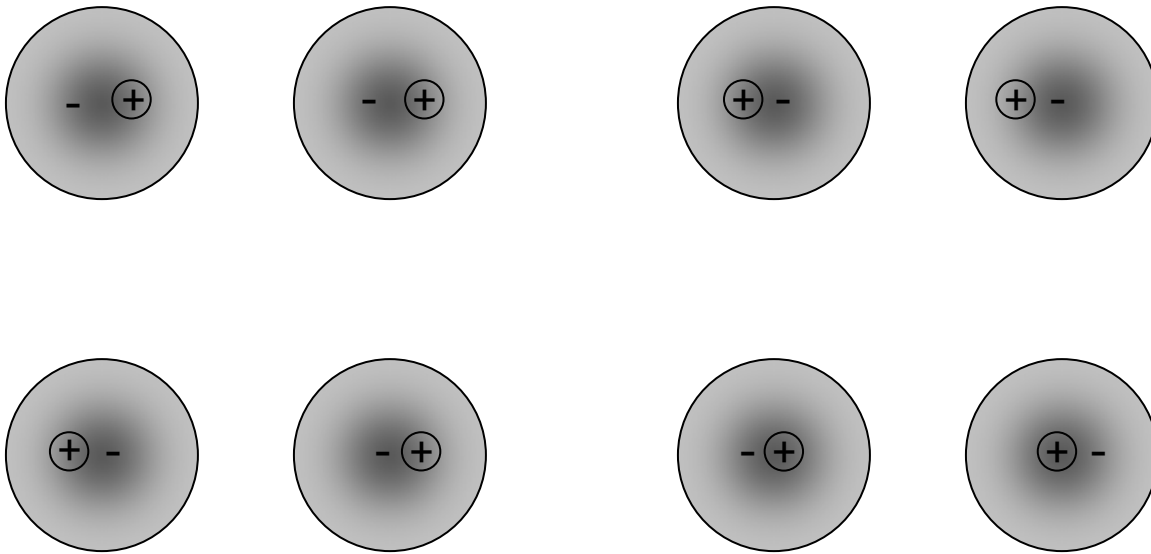
Figure 7.1. Dipoles orientation of two interacting atoms

In addition, the quantum mechanical treatment based on the second-order perturbation theory shows that the energy gained by this dispersion force is inversely proportional to the sixth power of the distance between two atoms.[167]

The net energy of interaction between two atoms is the sum of their energies leading to the attractive dispersion force and the repulsive exchange force. The energy is expected to depend on the distance by following the n-6 relation given by Eq. (7.1).

In order to simplify the calculation, the distance dependent factor of the repulsive term in Eq. (7.1) with n=12 can be obtained by a single multiplication from that of the attractive term. With the simple ratio between the two indices (12 and 6), it is more efficient for the computation. In addition, after the potential had been applied in various

material systems, it was proved that 9 is too small and 15 is too large for the index. Choosing $n=12$, the L-J potential can be written as:

$$U(r) = \lambda r^{-n} - \mu r^{-6} = U_0[(\frac{r_0}{r})^{12} - 2(\frac{r_0}{r})^6]$$

(7.2)

Where r_0 is the equilibrium distance, that is defined as the distance at where the potential has its minimum value U_0. U_0 is also the dissociation energy, which is defined as the energy required to move one of the atoms from the equilibrium position to infinite distance.

An example of the 12-6 L-J potential between two interacting carbon atoms is given in the Figure 7.2. When the distance is within the equilibrium distance, the net force is repulsive; while the distance is larger than the equilibrium distance, the net force is attractive. At the equilibrium distance, there is no net force between two carbon atoms.
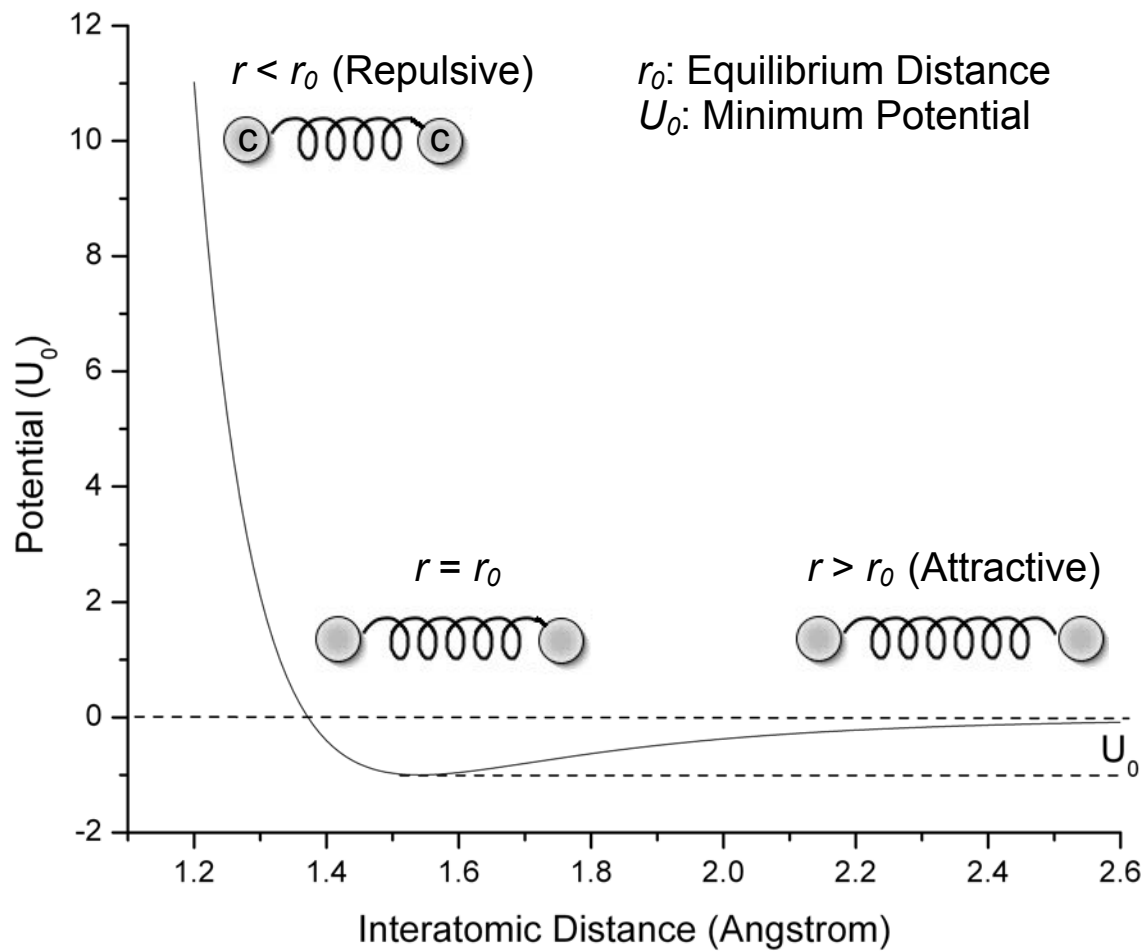
Figure 7.2. The 12-6 Lennard-Jones potential

7.2. The Modified Lennard-Jones Potential

During the mechano-activation process (collision for DLC and bending deformation for PVDF), the applied external force would introduce extra energy and change the shape of the L-J potential curve. It is necessary to modify the L-J potential accordingly. In the modified the L-J potential, extra term W is added to represent the energy introduced by the mechano-activation, as expressed in Eq. (7.3):

$$U(r) = U_0[(\frac{r_0}{r})^{12} - 2(\frac{r_0}{r})^6] + W \tag{7.3}$$

where the work introduced through activation can be expressed as

$$W = \int \vec{F} \cdot d\vec{r} \tag{7.4}$$

With the extra work, the potential curve will deviate from its original plotting. The extra work is not only able to vary the equilibrium distance, change the minimum potential, but also can alter the shape of the potential curve. As shown in Eq. (7.4), the effect of this extra term would be a function of the external force. In our case, Eq. (7.4) can be further simplified upon considering the experimental conditions.

In the experiments of PVDF, samples with 9 um thickness (T) were used. Both longitudinal and transversal bending deformation was applied using a special sample holder, a half-cylinder with a diameter (D) of 12 mm. Based on the geometry of the experimental set-up, as shown in the Figure 7.3, the strain caused by the tensile force can be calculated using Eq. (7.5).

$$\varepsilon \cong (D/T + 1)^{-1} \tag{7.5}$$

The resulting strain in PVDF film at the top of the sample stand is 0.15%. Comparing with the published data[168], the film is still in elastic regime under bending deformation. So the applied tensile can be regarded as a constant. Consequently Eq. (7.4) would be simplified as the product of the tensile force and the resulting displacement.

Tensile Force
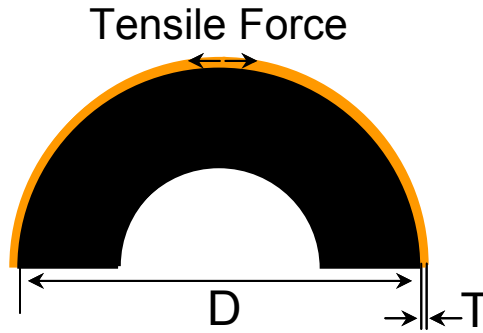
Figure 7.3. Experimental set-up for PVDF

In the experiments of DLC, Ar ions and carbon atoms interact strongly for a short time during collision. The total momentum of the system remains conservative. The average force during collision can be used to describe the interaction. The work introduced through collision will be further simplified as the product of the average force and the resulting displacement.

In the expression of the modified L-J potential, the displacement is defined as the difference between the equilibrium distance and the distance under external force. Thus the displacement caused by compressive force and tensile force would have different sign, which is positive for compressive force and negative for tensile force. Following the rule, the work done by a tensile force on the PVDF can be expressed as:

$$W = -F_0 \cdot \Delta r \tag{7.6}$$

where F_0 is the applied tensile force.

For DLC, when the impact force is tensile, the work has the form:

$$W = -F_{c0} \cdot \Delta r \tag{7.7}$$

When the impact force is compressive, the work has the expression:

$$W = F_{c0} \cdot \Delta r \qquad (7.8)$$

where F_{c0} is the force caused by collision.

Using the simplified form, as shown in Eq. (7.6), (7.7), and (7.8), the modified L-J potential for PVDF and DLC will be in the following format:

For PVDF,

$$U(r) = U_0 [(\frac{r_0}{r})^{12} - 2(\frac{r_0}{r})^6] - F_0 \cdot \Delta r \qquad (7.9)$$

For DLC (Tensile Force)

$$U(r) = U_{c0} [(\frac{r_{c0}}{r})^{12} - 2(\frac{r_{c0}}{r})^6] - F_{c0} \cdot \Delta r \qquad (7.10)$$

For DLC (Compressive Force)

$$U(r) = U_{c0} [(\frac{r_{c0}}{r})^{12} - 2(\frac{r_{c0}}{r})^6] + F_{c0} \cdot \Delta r \qquad (7.11)$$

7.2.1. Mechano-activated Potential in DLC

Firstly, the modified L-J potential was applied to describe the interaction between two carbon atoms with and without force. When there is no activation, the interaction between two carbon atoms follows the normal L-J potential, as plotted in the Figure 7.4. In the calculation, a cutoff distance was selected to be 3 Å, which is larger than the second nearest-neighbor distance. Other higher order contribution would be neglected. For diamond structure, the nearest-neighbor distance is 1.54 Å and the second nearest-

neighbor distance is 2.52 Å. For graphite, the nearest-neighbor distance is 1.42 Å and the second nearest-neighbor distance is 2.46 Å.[169,170] The values of U_{c0} and r_0 were acquired from the Molecular Dynamics Simulation.[169] Here we choose 711 kJ/mol (7.37 eV) for U_{c0} and 1.54 Å for r_{c0}. The corresponding energy barrier is 7.10 eV up to the cut off distance.
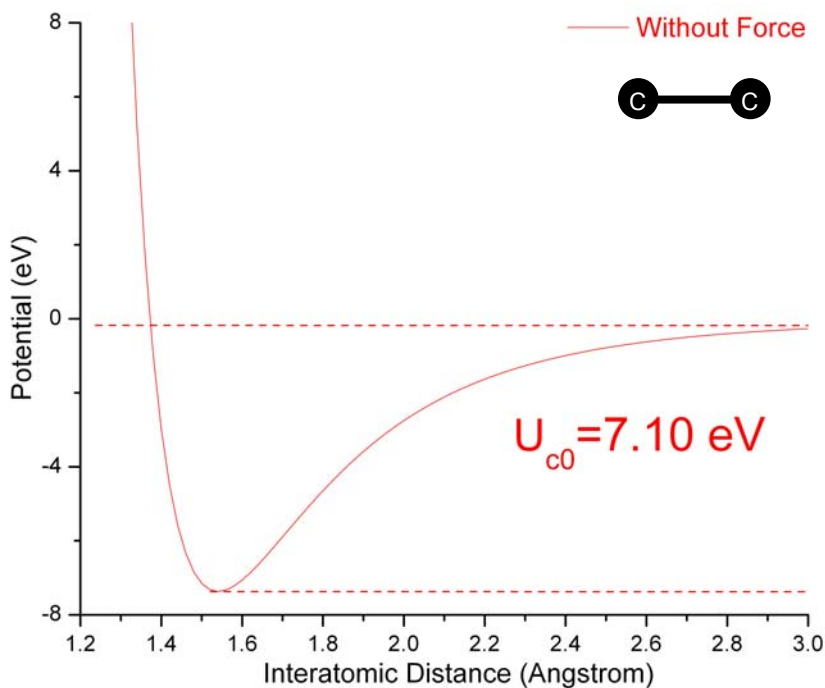
Figure 7.4. The Lennard Jones (L-J) potential between two carbon atoms

Under a tensile force, the interaction between two carbon atoms follows the modified L-J potential (Eq. (7.10)), as plotted in the Figure 7.5. The same values were used for U_{c0} and r_0. The magnitude of the tensile force is 0.5 nN, which is smaller than the measured C-C bond rupture force (2.6 ~ 13.4 nN).[171] The corresponding energy barrier is 6.37 eV (U'_{c0}), which is smaller than the value of the case without force.
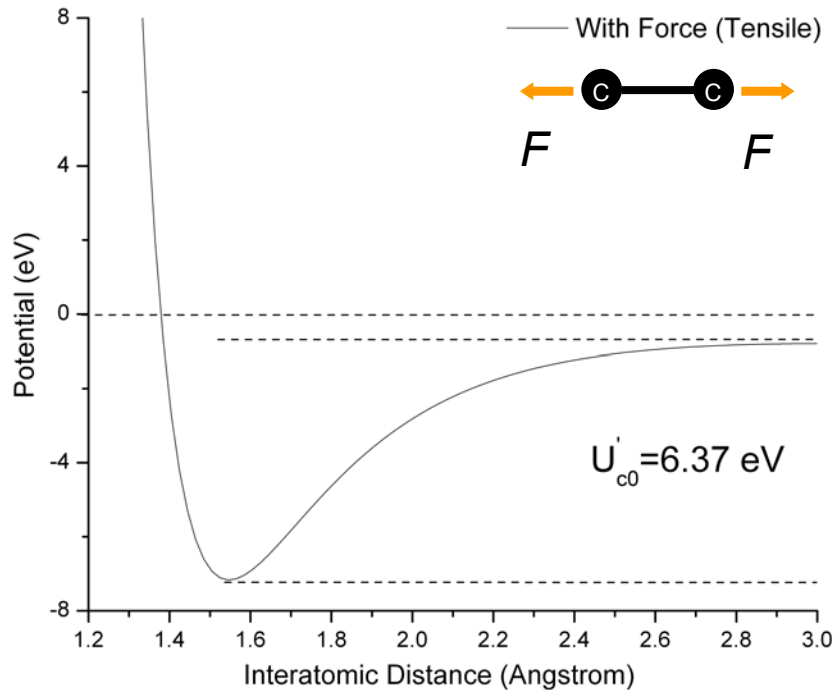
Figure 7.5. The modified L-J potential between two carbon atoms (with tensile force)

Under a compressive force, the interaction between two carbon atoms follows the modified L-J potential (Eq. (7.11)), as plotted in the Figure 7.6. For consistency, the magnitude of compressive force is also chosen as 0.5 nN. The corresponding energy barrier is 7.83 eV (U''_{c0}), which has the largest value among these three cases (without force, with tensile force, and with compressive force).
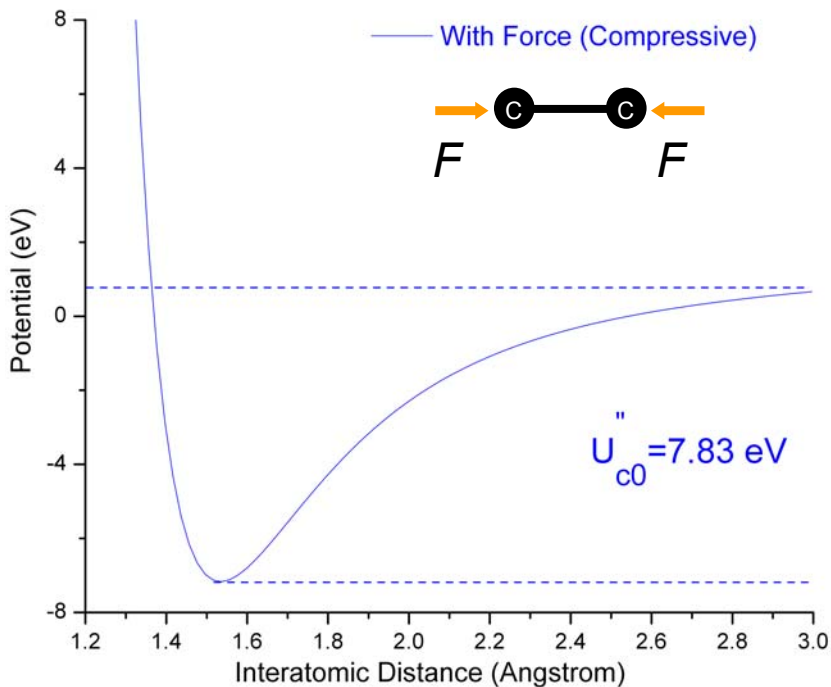
Figure 7.6. The modified L-J potential between two carbon atoms (with compressive force)

In comparison the potential with that with and without activation, under an external force, we are able to confirm that the applied force can deform the potential curve and alter the energy barrier, and consequently initiate a chemical change or physical-chemical exchange. The relationship between theses dissociation energies is:

$$U'_{c0} < U_{c0} < U''_{c0} \tag{7.12}$$

By plotting the potential curves together, we were able to compare them directly, as shown in the Figure 7.7. The applied forces not only deformed the shape of potential curves, but also shifted the equilibrium distance. Under a compressive force, this distance

(r''_{c0}) became shorter. Under a tensile force, this distance (r'_{c0}) became longer. The relationship between r_{c0}, r'_{c0}, and r''_{c0} is:

$$r''_{c0} < r_{c0} < r'_{c0} \tag{7.13}$$
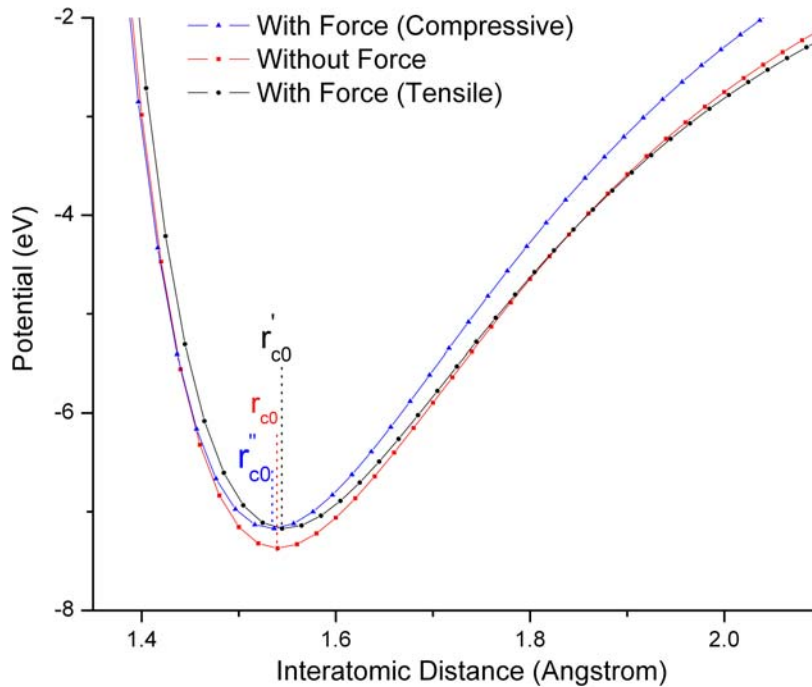
Figure 7.7. Comparison between the potential curve of without force, with force (tensile), and with force (compressive)

For the 3D case, as shown in the Figures 7.8, 7.9, and 7.10, more variables were needed to describe the distance change. For convenience, we choose the polar coordinates and set ρ and Z as variables. The interaction between the carbon atom at the top and the others can be calculated using Eq. (7.14)

$$E = \sum_{i,2}^{5} U(r_{1i}) \tag{7.14}$$

where

$$U(r_{1i}) = U_{c0}[(\frac{r_{c0}}{r_{1i}})^{12} - 2(\frac{r_{c0}}{r_{1i}})^{6}]$$
(7.15)

When there is no activation, the interaction between the carbon atom at the top and others follows the normal L-J potential. The potential contour was then calculated based on the range of ρ (1~3 Å) and Z (0~2 Å), as plotted in the Figure 7.8. For consistency, we choose 711 kJ/mol (7.37 eV) for U_{c0} and 1.54 Å for r_{c0}. The same cut off distance (3 Å) was used for ρ.
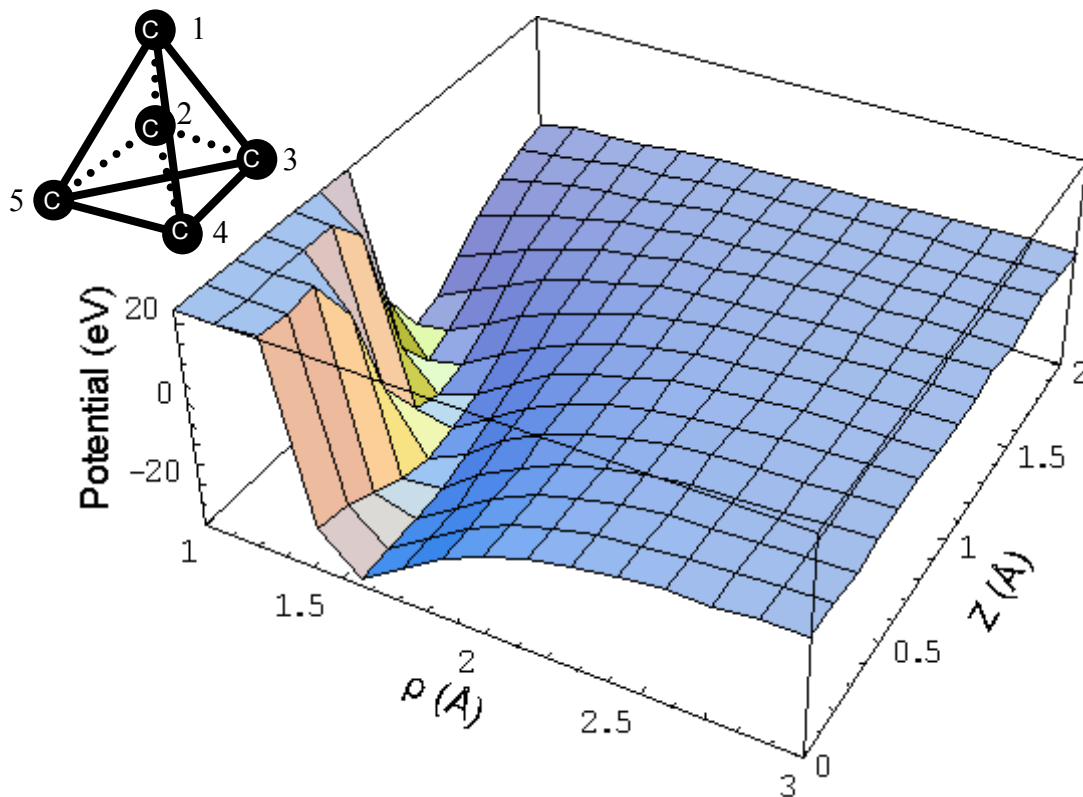
Figure 7.8. The L-J potential contour of a carbon atom in 3D case

With the activation, the interaction between the top carbon atom and its any other pair follows the modified L-J potential. The potential contours were calculated and plotted in the Figures 7.9 and 7.10, where the Figure 7.9 shows the result with a tensile force applied and Figure 7.10 shows that with a compressive force. The magnitude of the tensile or compressive force is 0.5 nN, that is smaller than the measured C-C bond rupture force.[171]
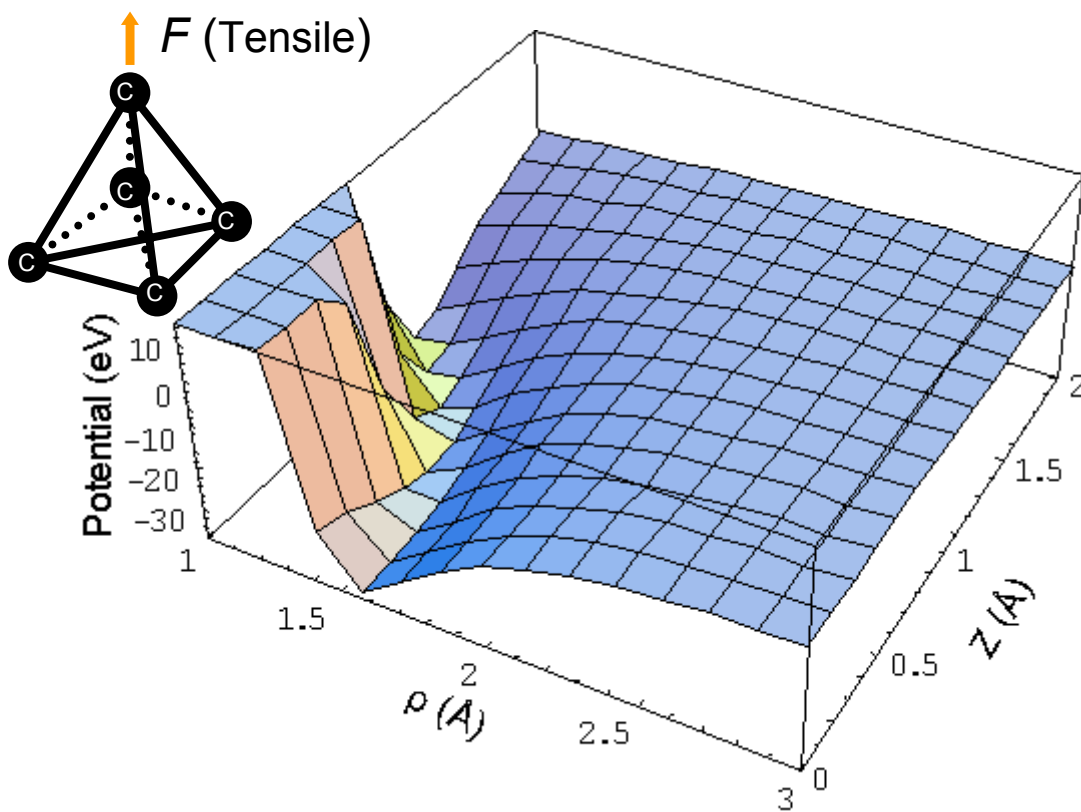
Figure 7.9. The modified L-J potential contour of a carbon atom in 3D case (tensile force)

The calculated potential contours demonstrated the same trend as observed in the 2D case. The tensile force would reduce the energy barrier and the compressive force would raise the same.
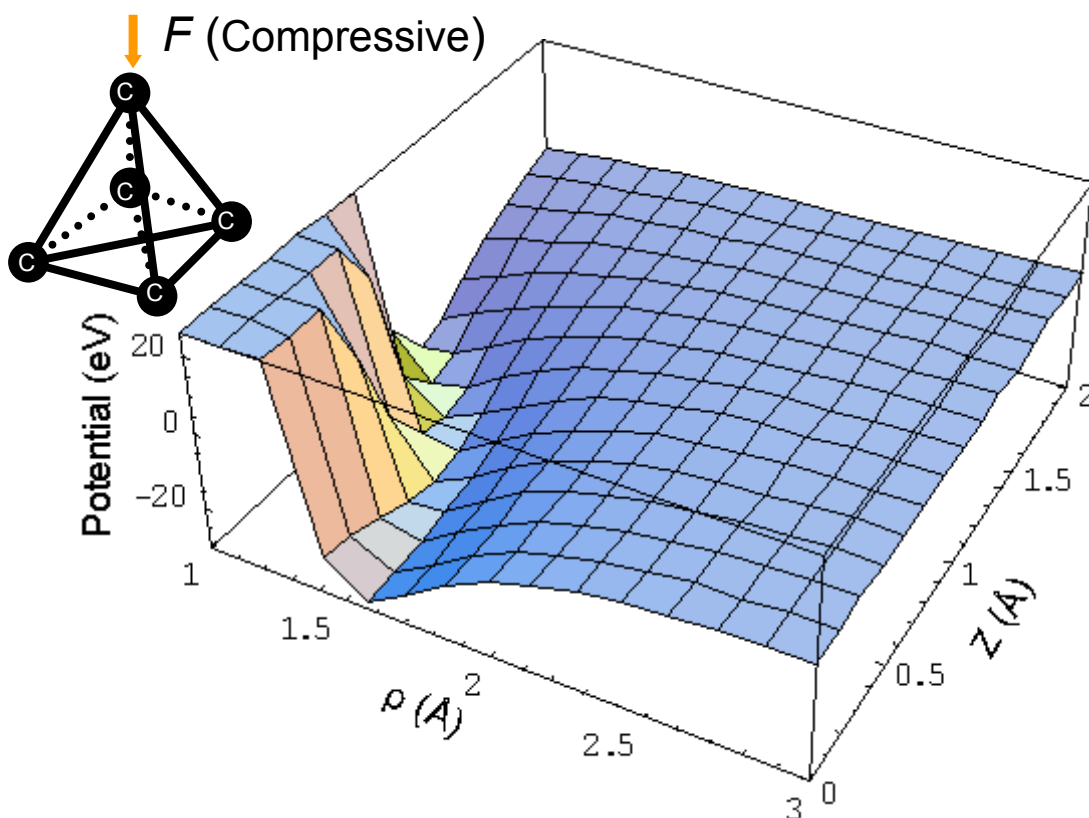
Figure 7.10. The modified L-J potential contour of a carbon atom in 3D case (compressive force)

Considering the contribution of mechano-activation, the modified L-J potential was proposed to describe the effects of activation on the interaction between carbon atoms. The results demonstrated that a tensile force would reduce the energy barrier of the system; while a compressive force would raise the same. Consequently the tensile force would increase the reactivity of the system.

In the experiment, the incident Ar ions have the kinetic energy (5 keV) that is much larger than the bond strength between carbon atoms in diamond (7.37 eV) or graphite (5.43 eV). The carbon atoms on the surface could be directly removed during the collision. It is necessary to point out that we did not consider the collision time during our modeling and experiments. We assumed that the mechanical force was induced at the moment when the collision was taking place.

As shown in Figure 7.11, the system energy of the left structure can be displayed in an in-plane triangle structure, as shown in Figure 7.11, was calculated using the multi-body L-J potential:

$$E = \frac{1}{2} \sum_{i \neq j, 1}^{4} U(r_{ij}) \tag{7.16}$$

where

$$U(r_{ij}) = U_{c0}[(\frac{r_{c0}}{r_{ij}})^{12} - 2(\frac{r_{c0}}{r_{ij}})^6] \tag{7.17}$$

The in-plane triangle structure has the system energy of -3.31 U_{c0} that is smaller than that of the left tetrahedral structure, -3.22 U_{c0}. The energy difference is 0.66 eV. With the removal of the carbon atom at top, the left structure would rearrange itself to the in-plane triangle structure. Because the latter geometry has lower system energy than the prior one, we should be able to observe a transformation from the sp^3 hybridization (diamond structure) to sp^2 hybridization (graphite structure) state during experiments.

$E = -3.22\ U_{c0}$ $E = -3.31\ U_{c0}$
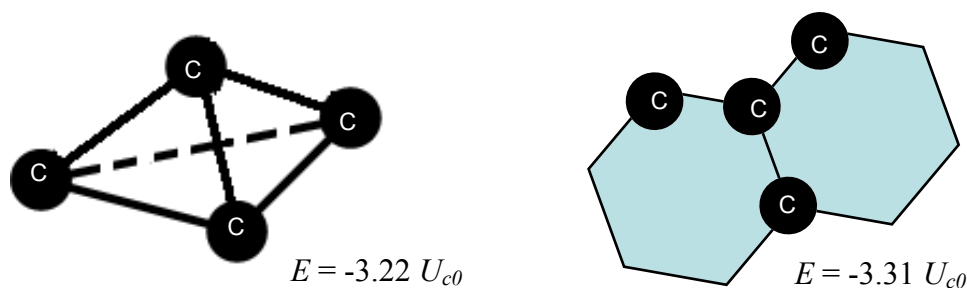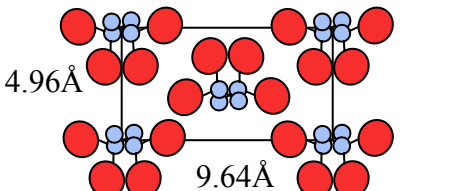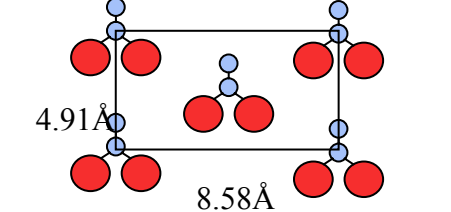
Figure 7.11. System energy of the left tetrahedral structure and the in plane triangle structure

In the experiments, this hybridization state transformation was clearly confirmed by the X-ray photoelectron spectroscopy characterization and analysis (details can be found in Chapter IV). The sample with excessive Ar ion bombardment has less content of sp3 hybridization state and more content of sp2 hybridization state than the other two samples (Table 4.1). These results are the evidence of the transformation from the sp^3 (diamond structure) to sp^2 (graphite structure) state, as predicted by Eq. (7.10), (7.16), and (7.17).

7.2.2. Mechano-activated Potential in PVDF

PVDF has four common crystalline structures or phases, as designated α, β, γ, and δ, as shown in the Figure 3.2. The in-plane unit cell of α and β phase has the similar size, 4.96 Å wide and 9.64 Å long for α phase, 4.91 Å wide and 8.58 Å long for β phase.[172] Based on the calculation by Su et al.,[173] the formation of each phase requires different amount of energy, as shown in the Table 7.1.

Table 7.1. Phases of PVDF and their relative formation energy

Phase	Structure	Relative Energy/Carbon Atom (kcal/mol)
α	4.96Å 9.64Å	0
β	4.91Å 8.58Å	2.38

As shown in the Figure 7.12, the formation of α phase takes less energy than that of β phase. With extra energy, the transformation between α and β phase would be initiated.
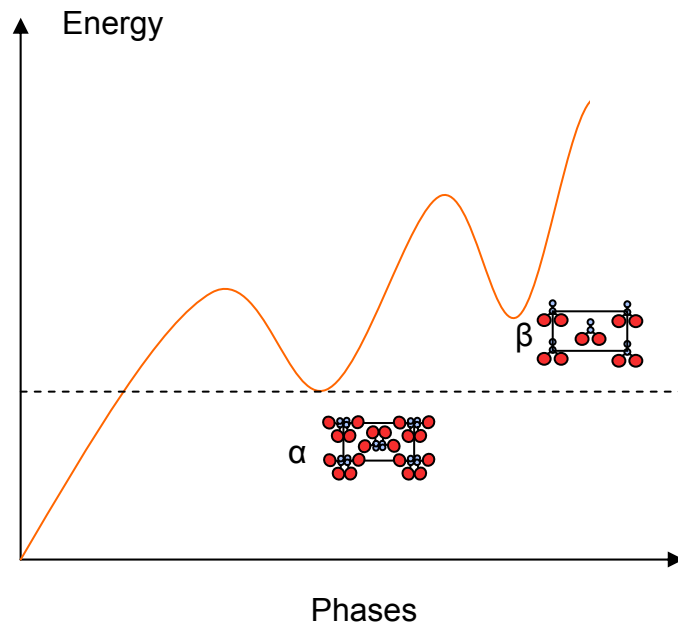
Figure 7.12. Energy-phase diagram of PVDF (α and β phase)

A simple calculation on the work done by an applied tensile force was conducted. Under deformation, the resulting strain was 0.1%. The Young's modulus of a PVDF film (with 9 μm thickness) is 3.2×10^9 Pa based on our measurement.[80] For α phase, the area (A) of a unit cell is about 0.5×10^{-18} m^2. Then for each unit cell, the tensile force can be calculated using Eq. (7.18)

$$F = \sigma \cdot A = E \cdot \varepsilon \cdot A \qquad (7.18)$$

where E is the Young's modulus of PVDF, σ is the tensile stress, A is the area of the unit cell, ε is the tensile strain. The tensile force has the magnitude of 1.6 pN.

The PVDF is a polymer consisting of long chain molecules, which has an averaged length (l_0) of 50 μm.[174] Thus the work done by the tensile force can be calculated using Eq. (7.19)

$$W = F \cdot \Delta l = F \cdot l_0 \cdot \varepsilon \qquad (7.19)$$

where l_0 is the average length of the chain, ε is the tensile strain. The work done by the tensile force is about 1.15 kcal/mol. It is compatible to the energy required to cause transformation between different phases in PVDF.

The modified L-J potential can be applied to describe the interaction between the mer units in α and β phase. For α and β phase, the in-plane unit cell has similar size. The equilibrium distances between mer units along the chain are different, i.e., 2.67 Å for α phase and 2.98 Å for β phase. There is a 0.31 Å difference between them. This difference indicates that under tensile force (along the chain direction), α phase would be easier to get extended than β phase. In experiments, researchers already reported the phase transformation in PVDF under electrical poling. But a clear explanation has not been given. Since in the experiment, the applied tensile force is along the chain direction, as shown in the Figure 7.13, we will focus on the effect of the applied tensile force on the potential curve of α phase.
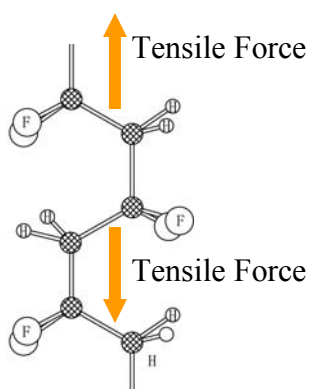
Figure 7.13. The applied tensile force (along the chain direction) in α phase

The results are shown in Figure 7.14, the applied tensile force would reduce the energy barrier and increase the equilibrium distance. For α phase, $U_{\alpha 0}$ (U_0) is the minimum potential, $r_{\alpha 0}$ is the equilibrium distance (2.67 Å).[173]

Figure 7.14. Comparison between the potential curves of α phase. Without force (red), with tensile force (black)

In the experiment, the PVDF film used contained different phases. To simplify the calculation, we choose a system that only contains α and β phase. The energy of the system can be expressed using the potential curve of α and β phase. $U_{\beta 0}$ is the minimum potential for β phase which is larger than $U_{\alpha 0}$ (U_0), and $r_{\beta 0}$ is 2.98 Å.[173]

$$U_{\alpha} = U_{\alpha 0}[(\frac{r_{\alpha 0}}{r})^{12} - 2(\frac{r_{\alpha 0}}{r})^{6}] \tag{7.20}$$

$$U_{\beta} = U_{\beta 0}[(\frac{r_{\beta 0}}{r})^{12} - 2(\frac{r_{\beta 0}}{r})^{6}] \tag{7.21}$$

The L-J potential curves of the system is given in Figure 7.15. There is a crossover at 2.88 Å between these two potential curves. It also clearly shows that when $r_{\alpha0} < r < 2.88$Å, α phase has smaller system energy than β phase; while when 2.88Å $< r < r_{\beta0}$, β phase has smaller system energy than α phase.
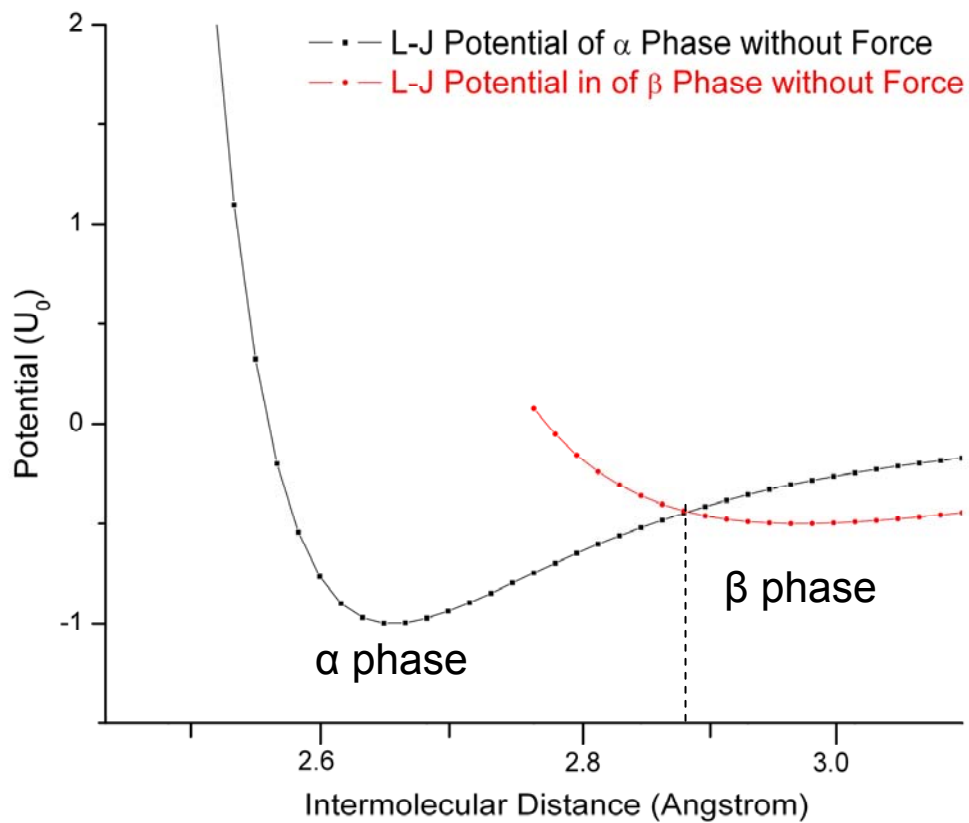
Figure 7.15. L-J potential curves of α and β phase. α phase. α phase (black), β phase (red)

Because the system always prefers to stay at the least energy states, the potential curve of the system would be the combination of α and β phase. When r < 2.88Å, it

follows the potential of α phase; When r > 2.88Å, it follows the potential of β phase, as shown in the Figure 7.16.

As shown in the Figure 7.16, the crossover between the potential curves created the energy barrier between the minimum energy between α and β phase. In this case, a finite activation energy (E_a) is required to surmount the energy barrier leading to the phase transformation between α and β phase.
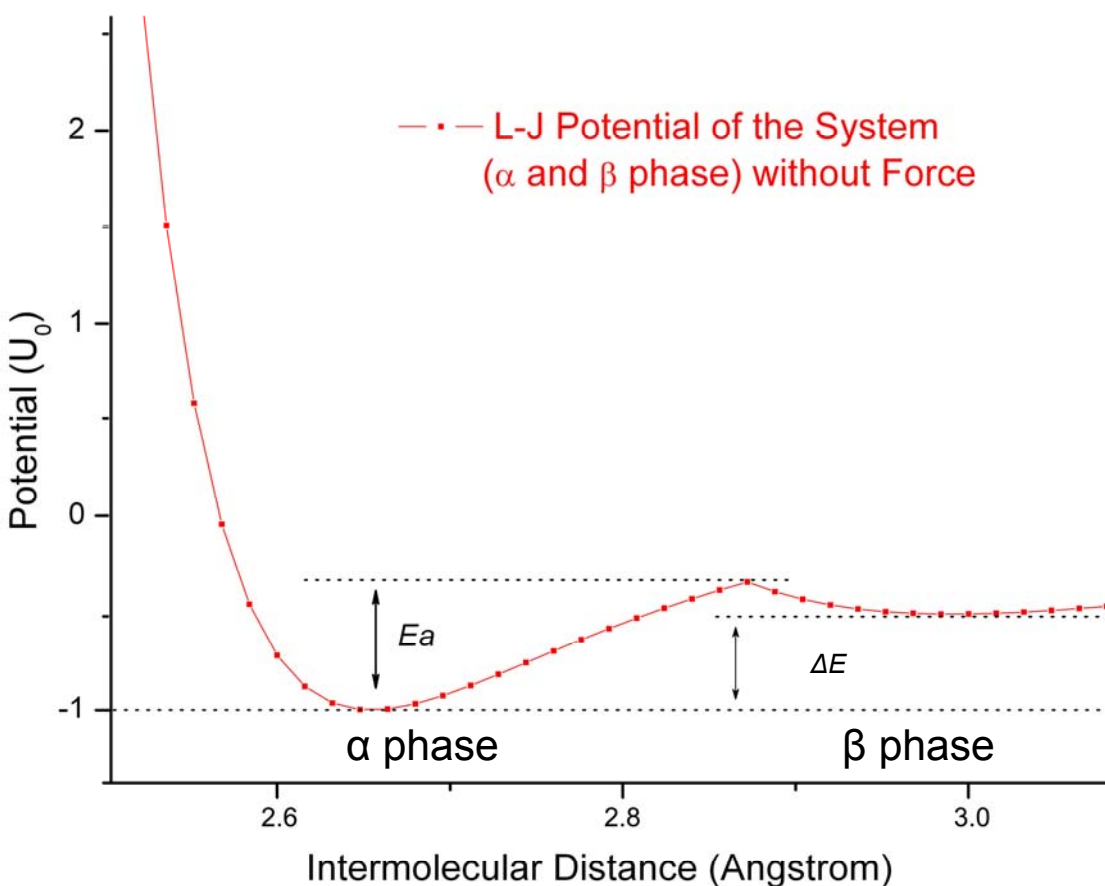
Figure 7.16. L-J potential curves of the system

As shown in the Figure 7.14, the energy barrier in α phase would be reduced under the tensile force. Thus for the system only contains α and β phase, the effect of the applied tensile force on the potential curve can be calculated using Eq. (7.22) and (7.23).

$$U_\alpha = U_{\alpha 0}[(\frac{r_{\alpha 0}}{r})^{12} - 2(\frac{r_{\alpha 0}}{r})^6] - F_0 \cdot \Delta r \tag{7.22}$$

$$U_\beta = U_{\beta 0}[(\frac{r_{\beta 0}}{r})^{12} - 2(\frac{r_{\beta 0}}{r})^6] - F_0 \cdot \Delta r \tag{7.23}$$

A comparison between the potential curve of the system with and without force is given in the Figure 7.17. The results demonstrate that the tensile force is not only able to reduce the activation energy barrier between α and β phase, but also can raise the minimum potential in the potential plotting, as marked by the arrows in the Figure 7.17. The comparison demonstrates that the tensile force is able to excite the system (raising the minimum potential), reduce the activation barrier, and increase the reactivity of the system. Consequently, with the tensile force, it is clear that the possibility for the transformation between α and β phase would increase. Thus in the experiment, we would be able to observe the phase transformation while the tensile force applied on PVDF film.
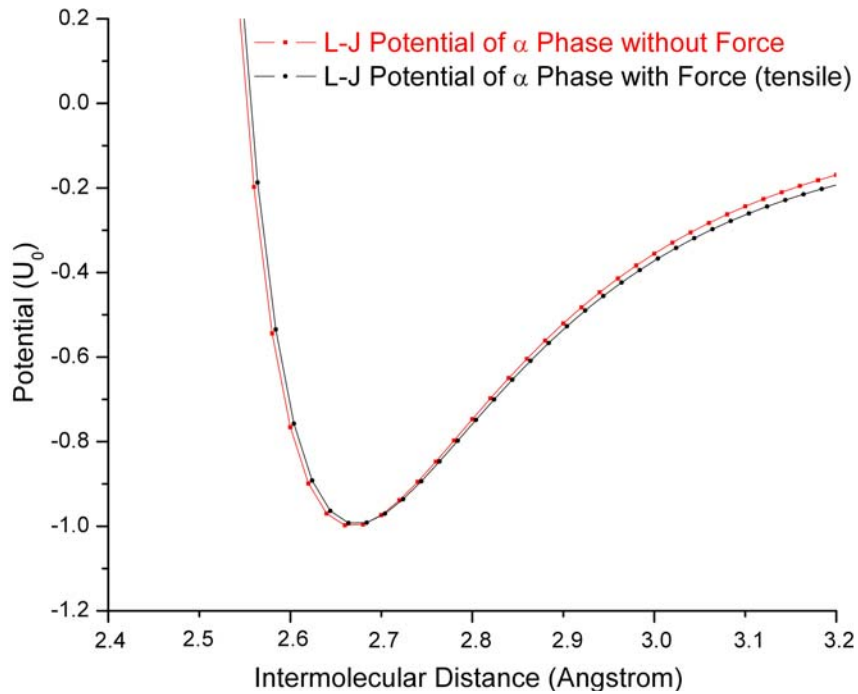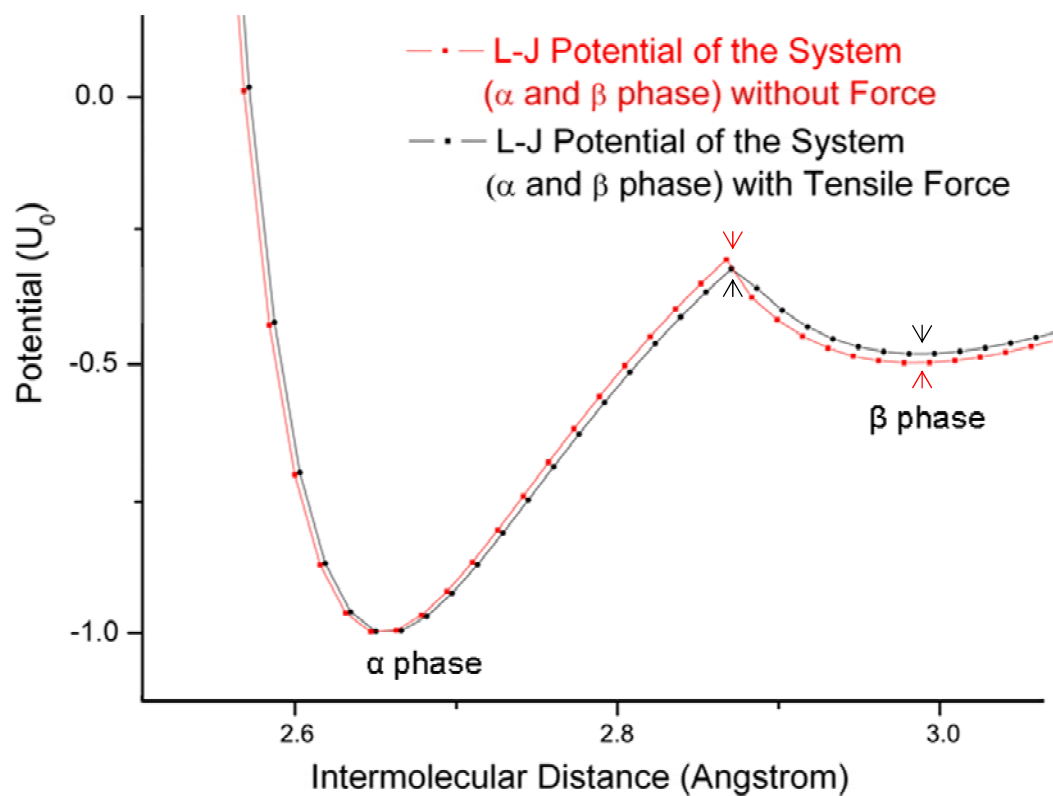
Figure 7.17. Comparison between the potential curves of the system. without force (red), with tensile force (black)

In the experiments, Fourier Transform Infrared Spectroscopy (FTIR) was used to identify the phase transformation while a tensile force was applied. The results clearly verified the transformation between α and β phase took place right after the force was applied. This is correlated well with the prediction from the modified L-J potential (Eq. (7.9), Eq. (7.20), and Eq. (7.23)).

7.3. Summary

An empirical interatomic/intermolecular potential was introduced to describe the effects of mechano-activation in DLC. The potential was tested by comparing the activation energy as a function of the applied mechanical force for carbon atoms. The predicted transformation between sp^3 and sp^2 hybridization state was confirmed by the experiment.

The proposed potential is then applied to study a more complicated system, PVDF (a polymer), which have several molecular arrangements or phases. The effects of the applied tensile force on the energy barrier were examined. Results were further linked to the energy required for the formation of each phase, which predicted the phase transformation in PVDF under the applied tensile force. It was further confirmed by the experimental results.

Using the modified L-J potential, we were able to describe the energy states under the influence of a mechanical force. The effects of mechano-activation in DLC and PVDF were examined by the modified potential that was validated through experimental results.

On the basis of an appropriate potential that contains the contribution from mechano-activation, we were able to describe the energy states under the influence of mechanical force. In light of the modified L-J potential, we examined the effect of the mechanical force from the energy point of view. The experimental results matched well with the proposed theory.

CHAPTER VIII

CONCLUSIONS AND FUTURE RECOMMENDATIONS

8.1. Conclusions

The research presented in this dissertation focused on mechanisms of mechano-activation and its effects on materials properties. Experimental investigation on selected materials, DLC (ceramic), PVDF (polymer, Ag-NCs (metallic nanostructures), were conducted. The effects of mechano-activation were characterized at different length scales. Theoretical analysis was carried out combining experiments which elucidates the mechano-activation process from the energy point of view.

The following lists the major results of research.

1. For DLC, results confirmed that the collision-induced transformation between hybridization states of carbon, and the changing ratio of sp^2 and sp^3 hybridization dominated the friction behavior of the film. With more graphitic carbon (sp^2 hybridization) on the surface, the friction is reduced.

2. For PVDF, results demonstrated that the applied tensile force induced the transformation of α, β, and γ crystalline phase. In addition, the transformation observed was time and direction dependent.

3. For Ag-NCs, a new approach based on the mechanism of mechano-activation was developed for nanochain structure synthesis. Molecular dynamics simulation and experimental results revealed that the formation of Ag-NCs is a synergetic physical-chemical procedure.

The above results proved that mechano-activation is an alternate method to excite electronic and molecular structures. Effects of mechano-activation on materials properties can be observed at different length scales.

4. For the first time, the observed mechano-activation phenomena was elucidate from the energy point of view using the modified Lennard-Jones potential. It was found that the applied mechanical force is able to deform the potential curve which represents the interaction between two atoms and/or molecules altering dissociation energy. The proposed potential was successfully validated by the experimental results of DLC and PVDF. New understanding on mechano-activation was obtained.

This research would not only bring insight into the understanding on the mechano-activation process, but also open new avenues for tailoring materials property and fabricating novel structures with precise control. The understanding obtained here would have significant impacts on materials science and the related industrial applications.

8.2. Future Recommendations

For future research, the following recommendations are suggested:

1. In the proposed theory, the potential was calculated in one unit structure. Further understanding would be able to obtain when more unit structures are included in calculation.

2. The application of mechano-activation in nanoscience would be the next interesting research topic. The combination of them could not only open new avenues for the synthesis of nanomaterials, but also inspire novel approaches in the way to "force" a reaction.

REFERENCES

(1)   *Oxford English Dictionary*, 11 ed.; Oxford University Press: New York, 2008.

(2)   Gilbert, W. *De Magnete, Magneticisque Corporibus, et de Magno Magnete Tellure (One the Magnet and Magnetic Bodies, and on the Great Magnet the Earth)* **1600**.

(3)   Heathcote, N. H. D. V. *Annals of Science* **1967**, *23*, 261.

(4)   Zeeman, P. *Nature* **1897**, *55*, 347.

(5)   Thomson, J. J. *Phil. Mag., Series 6* **1913**, *26*, 1.

(6)   Millikan, R. A. *Physical Review* **1913**, *2*, 109.

(7)   Thomson, G. P. *Wave Mechanics of Free Electrons* McGraw-Hill Book Company: New York, 1930.

(8)   Kusch, P.; Foley, H. M. *Phys. Rev.* **1948**, *74*, 250.

(9)   Siegbahn, K. *Phil. Tans. Roy. Soc. London A* **1970**, 33.

(10)   Klitzing, K. V.; Dorda, G.; Pepper, M. *Phys. Rev. Lett.* **1980**, *45*, 494.

(11)   Binning, G.; Rohrer, H. *US Patent 4,343,993* **1982**.

(12)   Tsui, D. C.; Stormer, H. L.; Gossard, A. C. *Phys. Rev. Lett.* **1982**, *48*, 1559.

(13)   Ohta, T.; Bostwick, A.; Seyller, T.; Horn, K.; Rotenberg, E. *Science* **2006**, *313*, 951.

(14)   Liu, Y.; Flood, A. H.; Bonvallet, P. A.; Vignon, S. A.; Northrop, B. H.; Tseng, H. R.; Jeppesen, J. O.; Huang, T. J.; Brough, B.; Baller, M.; Magonov, S.; Solares, S. D.; Goddard, W. A.; Ho, C. M.; Stoddart, J. F. *J. Am. Chem. Soc.* **2005**, *127*, 9745.

(15)   Kundu, S.; Wang, K.; Huitink, D.; Liang, H. *Langmuir* **2009**, *25*, 10146.

(16)   Wang, K.; Kundu, S.; Lee, H.; Liang, H. *J. Phys. Chem. C* **2009**, *113*, 8112.

(17)   Wang, K.; Liang, H.; Martin, J. M.; Monge, T. L. *Appl. Phys. Lett.* **2007**, *91*, 051918.

(18)   Kauzmann, W.; Eyring, H. *J. Am. Chem. Soc.* **1940**, *62*, 3113.

(19)   Staudinger, H.; Leupold, E. O. *Ber. Deutsch. Chem. Ges.* **1930**, *63*, 730.

(20)   Beyer, M. K.; Clausen-Schaumann, H. *Chem. Rev.* **2005**, *105*, 2921.

(21)   Berkowski, K. L.; Potisek, S. L.; Hickenboth, C. R.; Moores, J. S. *Macromolecules* **2005**, *38*, 8975.

(22)   Charles, R. H.; Jeffrey, S. M.; Scott, R. W.; Nancy, R. S.; Jerome, B.; Scott, R. W. *Nature* **2007**, *446*, 423.

(23)   Smékal, A. *Naturwissenschaften* **1942**, *30*, 224.

(24)   Butyagin, P. Y. *Usperchi Chimiji* **1984**, *53*, 1769.

(25)   Juhász, A. Z.; Kolláth, B. *Acta Chimica Hungarica-Models in Chemistry* **1993**, *130*, 75.

(26)   Juhász, A. Z. *Particulate Science and Technology* **1998**, *16*, 145.

(27)   Boldyrev, V. V.; Tkacova, K. J. *J. Mater. Synth. Proc.* **2000**, *8*, 121.

(28)   Balaz, P. *Int. J. Miner. Process* **2003**, *72*, 341.

(29)   Takacs, L. *Minerals Met. Mater. Soc.* **2000**, *52*, 12.

(30)   Clark, G. L.; Rowan, R. *J. Am. Chem. Soc.* **1941**, *63*, 1302.

(31)   Wanetig, P. *Textilforschung* **1922**, *4*, 154.

(32)   Staudinger, H. *Ber. Deutsch. Chem. Ges.* **1930**, *63*, 921.

(33)   Lantz, M. A.; Hug, H. J.; Hoffmann, R.; Schedel, P. J. A. v.; Kappernderger, P.; Martin, S.; Baratoff, A.; Guntherodt, H. J. *Science* **2001**, *291*, 2580.

(34)   Erlandsson, R.; Yakimov, V. *Phys. Rev. B* **2000**, *62*, 13680.

(35)   Rubio, G.; Agrait, N.; Vieira, S. *Phys. Rev. Lett.* **1996**, *76*, 2302.

(36)   Rubio, G.; Bahn, S. R.; Agrait, N.; Jacobsen, K. W.; Vieira, S. *Phys. Rev. Lett.* **2001**, *87*, 026101.

(37)   Conti, M.; Falini, G.; Samori, B. *Angew. Chem. Int. Ed.* **2000**, *39*, 215.

(38)   Schmitt, L.; Ludwig, M.; Gaub, H. E.; Tampe, R. *Biophys. J.* **2000**, *78*, 3275.

(39)   Bowden, F.; Tabor, D. *The Friction and Lubrication of Solids*; Clarendon Press: Oxford, UK, 1958.

(40)   Bowden, F.; Yoffe, A. *Initiation and Growth of Explosion in Liquid and Solids*; Cambridge University Press: Cambridge, 1952.

(41)   Bowden, F.; Yoffe, A. *Fast Reactions in Solids*; Butterworths: London, 1958.

(42)   Thiessen, P. A.; Meyer, K.; Heinicke, G. *Grundlagen der Tribochemie*; Akademie Verlag: Berlin, 1967.

(43)   Gutman, E. G. *Mechanochemistry of Metals and Protection against Corrosion*; Metallurigija and Protection against Corrosion: Moscow, 1974.

(44)   Bertenev, G. M.; Razumovskaya, I. V. *Fiziko-chimiceskaja Mechanika Materialov* **1969**, *5*, 60.

(45)   Butyagin, P. Y. *Zurnal Vsesojuznogo Chimiceskogo Obscestva D. Mendelejeva* **1973**, *18*, 90.

(46)   Lyakhov, N. Z. *Folia Montana,* **1984**, *Extraoridnary Number*, 40.

(47)   Robertson, J. *Prog. Solid State Chem.* **1991**, *21*, 199.

(48)   Robertson, J. *Surf. Coatings Technol.* **1992**, *50*, 185.

(49)   Lifshitz, Y. *Diamond Rel. Mater.* **1996**, *5*, 388.

(50)   Lifshitz, Y. *Diamond Rel. Mater.* **1999**, *8*, 1659.

(51)   Robertson, J. *Adv. Phys.* **1986**, *35*, 317.

(52)   Pierson, H. O. *Handbook of Carbon, Graphite, Diamonds and Fullerenes: Processing, Properties and Applications*; Noyes Publications: Prak Ridge, NJ, 1993.

(53) Fallon, P. J.; Veersamy, V. S.; Davis, C. A.; Roberston, J.; Amaratunga, G. A. J.; Milne, W. I.; Koshinen, J. *Phys. Rev. B* **1993**, *48*, 4777.

(54) Li, F.; Lannin, J. S. *Phys. Rev. Lett.* **1990**, *65*, 1905.

(55) Ashby, M. F.; Jones, D. R. H. *Engineering Materials*; Pergamon Press: Oxford, UK, 1980.

(56) Jacob, W.; Moller, W. *J. Appl. Phys.* **1971**, *42*, 2953.

(57) McKenzie, D. R. *Rep. Prog. Phys.* **1996**, *59*, 1611.

(58) Field, J. E. *Properties of Diamond*; Academic Press: London, 1993.

(59) Kelly, B. T. *Physics of Graphite*; Applied Science Publishers: London, 1981.

(60) Pharr, G. M.; Callahan, D. L.; McAdams, D. D.; Tsui, T. Y.; Anders, S.; Anders, A.; Ager, J. W.; Brown, I. G.; Bhatia, C. S.; Silva, S. R. P.; Robertson, J. *Appl. Phys. Lett.* **1996**, *68*.

(61) Koidl, P.; Wangner, C.; Dischler, B.; Wagner, J.; Ramsteriner, M. *Mater. Sci. Forum* **1990**, *52*, 41.

(62) Bhushan, B. *Diamond Rel. Mater.* **1999**, *8*, 1985.

(63) Robertson, J. *Thin Solid Films* **2000**, *383*, 81.

(64) Goglia, P.; Berkowitz, J.; Hoehn, J.; Xidis, A.; Stover, L. *Diamond Rel. Mater.* **2001**, *10*, 271.

(65) Lettington, A. H. *Proc. R. Soc. A* **1993**, *342*, 287.

(66) Tiainen, V. M. *Diamond Rel. Mater.* **2001**, *10*, 153.

(67) Allen, M.; Myer, B.; Rushton, N. **2001**, *58*, 319.

(68) Kawai, H. *Jpn. J. Appl. Phys.* **1969**, *8*, 975.

(69) Sessler, G. M. *J. Acoust. Soc. Am.* **1981**, *71*, 1596.

(70) Harrison, J.; Ounaies, Z. "Piezoelectric Polymers, NASA/CR-2001-211422 ICASE Report No. 2001-43, NASA Langley Research Center: Hampton, VA.

(71) Davis, G. T. *Piezoelectric and Piezoelectric Polymers*; Academic Press: Boston, 1993.

(72) Lovinger, A. J. *Science* **1983**, *220*, 1115.

(73) Sobhani, H.; Razavi-Nouri, M.; Yousefi, A. A. *J. Appl. Polym. Sci.* **2007**, *104*, 89.

(74) McGrath, J. C.; Ward, I. M. *Polymer* **1980**, *21*, 855.

(75) Davis, G. T.; McKinney, J. E.; Broadhurst, M. G. *J. Appl. Phys.* **1978**, *49*, 4998.

(76) Naegele, D.; Yoon, D. Y.; Broadhurst, M. G. *Macromolecules* **1978**, *1*, 1297.

(77) Gupta, D. K. D.; Doughty, K. *Appl. Phys. Lett.* **1977**, *31*, 585.

(78) Weinhold, S.; Litt, M. H.; Lando, J. B. *Macromolecules* **1980**, *13*, 1178.

(79) Lovinger, A. J. *Macromolecules* **1981**, *14*, 322.

(80) Wang, K.; Lee, H.; Cooper, R.; Liang, H. *Appl. Phys. A* **2009**, *95*, 435.

(81) Pearman, G. T.; Hokanson, J. L.; Meeker, T. R. *Ferroelectrics* **41980**, *28*, 311.

(82) Pedersen, C. J. *J. Am. Chem. Soc.* **1967**, *89*, 2459.

(83) Pedersen, C. J. *Aldrichimica Acta* **1971**, *4*, 1.

(84) Christensen, J. J. *Science* **1971**, *459*, 174.

(85) Pedersen, C. J. *Fed. Proc.* **1965**, *27*, 1305.

(86) Gokel, G. W.; Leevy, W. M.; Weber, M. E. *Chem. Rev.* **2004**, *104*, 2723.

(87) Liang, H.; Martin, J. M.; Mogne, T. L. *Acta Mater.* **2003**, *51*, 2639.

(88) Grant, J. T.; Briggs, D. *Surface Analysis by Auger and X-ray Photoelectron Spectroscopy*; IM Publications: Chichester, UK 2003.

(89) Wang, K.; Rangel, N. L.; Kundu, S.; Sotelo, J. C.; Tovar, R. M.; Seminario, J. M.; Liang, H. *J. Am. Chem. Soc.* **2009**, *131*, 10447.

(90)   Kundu, S.; Wang, K.; Liang, H. *J. Phys. Chem. C* **2009**, *113*, 5157.

(91)   Kundu, S.; Wang, K.; Liang, H. *J. Phys. Chem. C* **2009**, *113*, 134.

(92)   Kundu, S.; Wang, K.; Liang, H. *J. Phys. Chem. C* **2009 Accepted**.

(93)   Sullivan, J. P.; Friedmann, T. A.; Hjort, K. *MRS Bull.* **2001**, *26*, 309.

(94)   Luo, J. K.; Flewitt, A. J.; Spearing, S. M.; Fleck, N. A.; Milne, W. I. *Appl. Phys. Lett.* **2004**, *85*, 5748.

(95)   Moseler, M.; Gumbsch, P.; Casiraghi, C.; Ferrari, A. C.; Roberston, J. *Science* **2005**, *309*, 1545.

(96)   Roberson, J. *Mater. Sci. Eng.* **2002**, *37*, 129.

(97)   Roberson, J. *Phys. Rev. Lett.* **1992**, *68*, 220.

(98)   Slater, J. C. *J. Appl. Phys.* **1951**, *22*, 237.

(99)   Wilkens, M. *5th Int. Conf. on High Voltage Electron Microscopy*; Imura T.and Hashimoto H. Eds; Japanese Society of Electron Microscopy; Kyoto, 1977, p475.

(100)   Makin, M. J. In *Proceeding of the Ninth Int. Congress on Electron Microscopy* Sturgess J. M. Ed.; Toronto, 1978; Vol. 3, p. 330.

(101)   Urban, K. *Phys. Status Solidi a* **1979**, *56*, 157.

(102)   Jung, P. *Atomic Defects in Metals*; Springer: Berlin, 1991; Vol. 3, Landoldt-Bornstein, New Series, p.1-87.

(103)   Cuomo, J. J.; Doyle, J. P.; Bruley, J.; Liu, J. C. *Appl. Phys. Lett.* **1991**, *58*, 466.

(104)   Briggs, D.; Seah, M. P. *Practical Surface Analysis* 2nd ed.; Wiley: Chichester, UK, 1996.

(105)   Leung, T. Y.; Man, W. F.; Lim, P. K.; Chan, W. C.; Gaspari, F.; Zukotynski, S. *J. Non-Cryst. Solids* **1999**, *254*, 156.

(106)   Diaz, J.; Paolicelli, G.; Ferrer, S.; Comin, F. *Phys. Rev. B* **1996**, *54*, 8064.

(107)   Merel, P.; Tabbal, M.; Chaker, M.; Moisa, S.; Margot, J. *Appl. Surf. Sci.* **1998**, *136*, 105.

(108) Voevodin, A. A.; Phelps, A. W.; Zabinski, J. S.; Donley, M. S. *Diamond Del. Mater.* **1996**, *5*, 1264.

(109) Liu, Y.; Erdemir, A.; Meletis, E. I. *Surf. Coat. Technol.* **1996**, *82*, 48.

(110) Liu, Y.; Erdemir, A.; Meletis, E. I. *Surf. Coat. Technol.* **1996**, *86-87*, 564.

(111) Ong, C. W.; Zhao, X. A.; Cheung, J. T.; Lam, S. K.; Liu, Y.; Choy, C. L.; Chan, P. W. *Thin Solid Films* **1995**, *34*, 258.

(112) Friendmann, T. A.; McCarty, K. F.; Barbour, J. C.; Siegal, M. P.; Dibble, D. C. *Appl. Phys. Lett.* **1996**, *68*, 1694.

(113) Gago, R.; Vinnichenko, M.; Jager, H. U.; Belov, A. Y.; Jimenez, I.; Huang, N.; Sun, H.; Maitz, M. F. *Phys. Rev. B* **2005**, *72*, 14120.

(114) Marks, N. A.; Cover, M. F.; Kocer, C. *Appl. Phys. Lett.* **2006**, *89*, 131924.

(115) Gilman, J. J. *Science* **1996**, *274*, 65.

(116) Kauzmann, W.; Eyring, H. *J. Am. Chem. Soc.* **1940**, *62*, 3113.

(117) Nguyen, T. Q.; Kausch, H. H. *Macromolecules* **1990**, *23*, 5137.

(118) Davis, G. T.; Wang, T. T.; Herbert, J. M.; Glass(eds.), A. M. *The applications of ferroelectric polymers.* ; Blackie: Glasgow, 1988.

(119) Nalwa, H. S. *J. Macromol. Sci.* **1991**, *31*, 341.

(120) Ray, M. C.; Bhattacharya, R.; Samanta, B. *AIAA J.* **1993**, *31*, 1684.

(121) Neugschwangdtner, G. S.; Schwodiauer, R.; Bauer-Gogonea, S.; Bauer, S. *Appl. Phys. A* **2000**, *70*, 1.

(122) Xia, F.; Xu, H.; Fang, F.; Razavi, B.; Cheng, Z. Y.; Lu, Y.; Xu, B.; Zhang, Q. M. *Appl. Phys. Lett.* **2001**, *78*, 1122.

(123) Zhang, Q. M.; Bharti, V.; Zhao, X. *Science* **1998**, *280*, 2101.

(124) Lang, S. B.; Musensit, S. *Appl. Phys. A* **2006**, *85*, 125.

(125) Vinson, J. H.; Jungnickel, B. J. *Ferroelectrics* **1998**, *216*, 63.

(126) Betz, N.; Moel, A. L.; Balanzat, E.; Ramillon, J. M.; Lamotte, J.; Gallas, J. P.; Jaskierowicz, G. *J. Polym. Sci., Part B: Polym. Phys.* **1994**, *32*.

(127) Teyssedre, G.; Bernes, A.; Lacabanne, C. *J. Polym. Sci., Part B: Polym. Phys.* **1993**, *31*, 2027.

(128) Mattsson, B.; Ericson, H.; Torell, L. M.; Sundholm, F. *J. Polym. Sci., Part B: Polym. Phys.* **1999**, *37*, 3317.

(129) Hilczer, B.; Kulek, J. *IEEE Trans. Dielectrics Elec. Insulation* **1998**, *5*, 45.

(130) Marcel, B.; William, B. E.; Otto, J. G. *Macromolecules* **2002**, *35*, 2682.

(131) Chen, G. C.; Su, J.; Fina, L. J. *J. Polym. Sci., Part B: Polym. Phys.* **1994**, *32*, 2065.

(132) Boccaccio, T.; Bottino, A.; Capannelli, G.; Piaggio, P. *J. Memb. Sci.* **2002**, *210*, 315.

(133) Gregorio, R.; Cestari, M. *J. Polym. Sci., Part B: Polym. Phys.* **1994**, *32*, 859.

(134) Salimi, A.; Yousefi, A. A. *J. Polym. Sci., Part B: Polym. Phys.* **2004**, *42*, 3487.

(135) Butyagin, P. Y. *Uspechi Chimiji* **1984**, *53*, 1769.

(136) Bumstead, H. A. *Am. J. Sci.* **1903**, *XVI*.

(137) Faraday, M. *Experimental-unter Elektricitat. I. and II. Reihe.* **1832**, *81*, 96.

(138) Trommsdorff, H. *Ann. Chem. Pharm.* **1834**, *11*, 190.

(139) Kauzmann, W. J.; Eyring, H. *J. Am. Ceram. Soc.* **1940**, *62*, 3113.

(140) Beyer, M. K.; Clausen-Schaumann, H. *Chem. Rev.* **2005**, *105*, 2921.

(141) Charles, R. H.; Jeffrey, S. M.; Scott, R. W.; Nancy, R. S.; Jerome, B.; Scott, R. W. *Nature* **2007**, *446*, 426.

(142) Rabinowicz, E. C. *Sci. Am.* **1968**, *218*, 91.

(143) Fischer, T. E.; Mullins, W. M. *J. Phys. Chem.* **1992**, *96*, 5690.

(144) Pearson, R. G. *Chemical Hardness: Applications from Molecules to Solids.* ; Wiley-VCH, 1997.

(145) Alivisatos, A. P. *Science* **1996**, *271*, 933.

(146) Murray, C. B.; Kagan, C. R.; Bawendi, M. G. *Annu. Rev. Mater. Sci.* **2000**, *30*, 545.

(147) Hong, B. H.; Bae, S. C.; Lee, C.; Jeong, S.; Kim, K. S. *Science* **2000**, *294*, 348.

(148) Caswell, K. K.; Bender, C. M.; Murphy, C. J. *Nano Lett.* **2003**, *3*, 667.

(149) Bhattacharyya, S.; Saha, S. K.; Chakravorty, D. *Appl. Phys. Lett.*, *77*, 3770.

(150) Sun, Y.; Xia, Y. *Adv. Mater.* **2002**, *14*, 833.

(151) Kohno, H. T., S. *Nanotechnology* **2007**, *18*, 395706.

(152) Cao, C., He, Y., Torras, J., Deumens, E., Trickey, S. B. & Cheng, H. P. *J. Chem. Phys.* **2007**, *126*, 211101.

(153) Yang, Y., Nogami, M., Shi, J., Chen, H. R., Ma, G. & Tang, S. *Appl. Phys. Lett.* **2006**, *88*, 081110.

(154) Liu, C. M., Guo, L., Wang, R. M., Deng, Y., Xu, H. B. & Yang, S. *Chem. Comm.* **2004**, *23*, 2726.

(155) Hong, J. W., R. Q. *Phys. Rev. B* **2004**, *70*, 060406.

(156) Bielmann, M.; Schwaler, P.; Ruffieux, P.; Groning, O.; Schlapbach, L.; Groning, P. *Phys. Rev. B* **2002**, *65*, 235431.

(157) Kaushik, V. K. *J. Electron Spectrosc. Relat. Phenom.* **1991**, *56*, 273.

(158) Hoflund, G. B.; Hazos, Z. F.; Salaita, G. N. *Phys. Rev. B* **2000**, *62*, 11126.

(159) Dong, X.; Jahanmir, S.; Hsu, S. *J. Am. Ceram. Soc.* **1991**, *5*, 1036.

(160) Barabanshchikov, Y. G. *Friction and Wear* **2004**, *25*, 481.

(161) Zhurkov, S. N.; Korsukov, V. E. *J. Polym. Sci. B* **1974**, *12*, 385.

(162) Kar, P.; Wang, K.; Liang, H. *Electrochem. & Solid-State Lett.* **2008**, *11*, 13.

(163) Kar, P.; Wang, K.; Liang, H. *Electro. Acta* **2008**, *53*, 5084.

(164) Lennard-Jones, J. E. *Proc. Roy. Soc. Ser. A* **1924**, *106*, 463.

(165)   Lennard-Jones, J. E. *Proc. Roy. Soc. Ser. A* **1926**, *112*, 214.

(166)   Kitaigorodsky, A. I. *Molecualr Crystal and Molecules*; Academic Press: New York, 1973.

(167)   London, F. *Z. Phys.* **1930**, *63*, 245.

(168)   Du, C.; Zhu, B.; Xu, Y. *Macromol. Mater. Eng.* **2005**, *290*, 786.

(169)   Tersoff, J. *Phys. Rev. Lett.* **1988**, *61*, 2879.

(170)   Girifalco, L. A.; Lad, R. A. *J. Chem. Phys* **1956**, *25*, 693.

(171)   Odell, J. A.; Keller, A. *J. Polym. Sci. B* **1986**, *24*, 1889.

(172)   Takahashi, Y.; Tadokoro, H. *Macromolecules* **1980**, *13*, 1318.

(173)   Su, H.; Strachan, A.; Goddard, W. A. *Phys. Rev. B* **2004**, *70*, 64101.

(174)   Sessler, G. M. *J. Acoust. Soc. Am.* **1981**, *70*, 1596.

VITA

Ke Wang was born and raised in Henan, China in 1978. He received the B.S. degree in physics with honors from Lanzhou University, Gansu, China in 2000. He received the M.S. degree in physics with honors from Peking University, Beijing, China, in 2003. With a solid background in physics, he developed a strong interest in materials science and engineering. Since 2007, he has been a research assistant at the Surface Science Laboratory of Texas A&M University, under the supervision of Dr. Hong Liang. His research focuses on nanofabrication, surface and interface science and engineering, especially the study on materials structure-function relationship. He received his Ph.D. in materials science and engineering in December 2009.

He may be reached at MS 3123, Texas A&M University, College Station, TX 77843. His email is ke.phwk@gmail.com.